The Impulsivity of Solar Flares: Concepts and Applications

Wilmar German Fajardo Mendieta

Universidad Nacional de Colombia
Facultad de Ciencias, Observatorio Astronómico Nacional
Bogotá, Colombia
November 2017

The Impulsivity of Solar Flares: Concepts and Applications

Wilmar German Fajardo Mendieta

Thesis presented as a partial requirement to get the title:
Master in Science - Astronomy

Advisor:
Prof. Benjamín Calvo Mozo
Associate Professor
Observatorio Astroómico Nacional
Universidad Nacional de Colombia

Co-advisor:
Dr. Juan Carlos Martínez Oliveros
Assistant Research Physicist
Space Sciences Laboratory
University of California, Berkeley

Research group:
Group of Solar Astrophysics

Universidad Nacional de Colombia
Facultad de Ciencias, Observatorio Astronómico Nacional
Bogotá, Colombia
November 2017

A mi familia,
porque al final del día siempre estarán ahí

Wilmar German Fajardo Mendieta

Agradecimientos

Esta sección va en español porque considero que las emociones se expresan mejor en la lengua materna. Primeo que todo, quiero agradecerle a mi mamá Carlina y a mi papá Germán, no solo por darme la vida, sino por dar día y noche su vida por mí. A mis hermanos y sobrinos, quienes considero mi familia, por su infinita paciencia durante la escritura de este documento, y también en la vida cotidiana, no soy una persona fácil de llevar.

Pasamos ahora al plano profesional. Como no mencionar a mi maestro y mentor, el Profesor Benjamín Calvo Mozo. Profe, ¿qué otra cosa le puedo decir que no haya dicho ya? A usted le debo el ser profesional, el ser físico. Sin importar a lo que me dedique en adelante, siempre voy a llevar su legado conmigo. Juan Carlos, para mí usted un ejemplo a seguir. Todo el GoSA ha caminado por un sendero amplio, el cual usted fue abriendo con sus pasos. Yo quiero hacer lo mismo, pero en otro ámbito. Ustedes dos queridos directores me guiaron para poder llevar a feliz término este trabajo. Gracias, muchísimas gracias, pues solo no lo hubiese podido hacer.

Al GoSA, mi familia en mi alma mater, en la cual ya llevo casi una década de mi vida. Muchachos, ustedes han sido mi motivación siempre. Ha sido un orgullo haberme formado con algunos de ustedes, y también haber contribuido mi granito de arena en la formación de otros. El GoSA y el Observatorio siempre serán mi casa. Algún día nos cruzaremos de nuevo.

Y en esta época de efervescencia y calor, como no mencionar a tres mujeres muy importantes. Saida, tomarte de la mano en estos siete años no tuvo precio. Es un recuerdo que siempre llevaré conmigo. Hasta la Luna, eso no ha cambiado. Valeria, gracias por tanto y por todo. Sobretodo por hacerme creer en mí. Una mano única, color carmesí. Victoria, la única capaz de hacerme parar de la silla cuando escribía este documento. No tienes ni cuatro meses y ya te amo.

A todos, gracias por hacerme sentir vivo.

Abstract

During the impulsive phase of solar flares a distribution of nonthermal electrons propagates from the site of energy release towards the lower layers of the solar atmosphere. Depending on their pitch angles, these electrons can get trapped inside coronal loops or precipitate to the chromosphere or photosphere. The whole picture of this scenario is given by the trapping-plus-precipitation model. The relevance of both processes, precipitation and trapping, was estimated via two dimensionless quantities, namely, the *impulsivity parameter* (IP) and the *trapping indicator* (TI). They were calculated from HXR and microwave emissions, respectively.

The IP and TI were computed in a work sample of 228 flares. HXR and microwaves data were provided by RHESSI and NoRP, respectively. These events were classified according to IP into three impulsivity types: high, medium, and low. This alternative classification of solar flares turned out to be independent of the HXR lightcurve used to measure the IP. On the other hand, the work sample was also classified into three trapping types, according to the values of TI. Such types were: short, average, and prolonged trapping. For events having a single peak in both HXR and microwaves, the trapping types define the regimes where precipitation or trapping dominates. Lastly, it was shown that some active seismically flares can be explained as events where the impulsivity is high (large IP) and magnetic trapping is poorly efficient (small TI). Therefore, this support the hypothesis that sunquakes can be generated by direct impact of energetic electrons.

Keywords: **Sun:activity; Sun:flares; Sun:X-rays; Sun: radio radiation; methods: data analysis** .

Table of Contents

List of Figures

List of Tables

1. Introduction

In this Chapter we will give a brief description of solar flares and the concept of impulsivity, whose approach given here is new for heliophysics. Then, the major goals of the present work are summarized, as well as the structure of the rest of the document. Throughout the text appear many terms and concepts related to solar physics. This terminology and also the generalities about the Sun can be found in Appendix A.1, if any further query is needed.

1.1. Solar Flares

One of the most important phenomena related to solar activity are flares. In one sentence, solar flares are powerful, sudden and localized releases of energy occurring in the solar atmosphere that generate transient disturbances in the surrounding medium. The energy of the flare is believed to be stored in the coronal magnetic field, as it is the only source that has the energy density required to these eruptive events to take place (See Table **1-1**). Such energy is released via magnetic reconnection. The duration of solar flares can range between several minutes and a few hours (Benz, 2016, [12]), which is short in comparison with other timescales related to solar activity, like the lifetime of sunspots. The typical disturbances driven by solar flares are Coronal Mass Ejections (CME), Solar Energetic Particles events (SEP), radio bursts, sunquakes and other different kind of waves (Hudson, 2011, [59]). Apparently, neither flares nor their subsequent related phenomena affect drastically or permanently the properties of the Sun-as-a-star.

Source of energy	Expression	Energy density
Kinetic	$m_p n v^2/2$	10^{-3}
Thermal	$n k_B T$	10^{-1}
Gravitational	$m_p n g h$	4×10^{-1}
Magnetic	$B^2/8\pi$	400

Table 1-1.: A typical flare releases roughly 10^{32} erg within a region whose characteristic length is 100 Mm, which accounts for an energy density of 100 erg cm^{-3}. At the coronal conditions, $n = 10^9$ cm^{-3}, $v = 10$ km/s, $T = 10^6$ K, $h = 10^5$ km and $B = 100$ G, the only source capable to supply this energy is the magnetic field (Mandrini, 2012, [85]; Forbes, Sec. 6.1.3, [44]). The energy density values are in CGS units.

The most accepted model for solar flares is the CSHKP model, named according to the initials of their main developers Carmichael (1964, [20]), Sturrock (1966, [108]), Hirayama (1974, [57]) and Kopp-Pneuman (1976, [70]). According to this model the temporal evolution of solar flares can be taxonomically organized into a set of three phases, namely: preflare, impulsive, and decay (Syrovatskii, 1972, [109]; Benz, 2016, [12]). Each of those phases is characterized by particular signatures across the electromagnetic spectrum, as we shall see below.

In the CSHKP model magnetic reconnection is considered as the physical process responsible for the energy release in a solar flare. Before this occur, the neighborhood of the future reconnection region slightly heats up. This is evidenced as an small enhancement in the Extreme Ultraviolet (EUV), signature that marks the preflare phase (Benz, 2016, [12]). After reconnection, a fraction of the non-potential magnetic energy stored at the coronal loops is transformed into thermal and kinetic energy, which is used to heat the surrounding plasma, and to accelerate particles adjacent to the reconnection region toward the outer and inner layers of the solar atmosphere. The former could be expelled out of the Sun producing SEPs or type III radio bursts, or could populate the ejected magnetic rope associated to a CME, while the latter propagates downwards through the loops, descending along their magnetic field lines and thus emitting microwaves via gyrosynchrotron radiation. These accelerated particles can be trapped inside the magnetic loops or can reach the denser layers of the solar atmosphere, as the chromosphere and upper photosphere. These particles deposit there the majority of their energy via bremsstrahlung generating Hard X-Rays (HXR). This initial evolutionary flare stage is known as impulsive phase (Kane, 1974, [63]).

As the descending accelerated particles are thermalized via Coulomb collisions at the dense layers, the chromospheric plasma receives an energy excess and it is rapidly heated to higher temperatures. Because the plasma cannot dissipate the incoming energy, it rises through the loop populating it with hot material. This causes an increment in the average pressure and density in the loop, but not necessarily in its size. This process is known as *chromospheric evaporation*. It was reported for the first time by Antonucci et al. (1982, [1]), who measured blue-shifted components in the CaXIX and FeXXV lines which correspond to upward line-of-sight motions with velocities ranging between 250 and 450 km s^{-1}. Once the chromospheric material is evaporated into the lower corona, the plasma inside the loop relaxes and its temperature decreases. Such cooling process is evidenced as a slow decay in the SXR and Hα time profiles. This is the main observational feature of the decay phase. Historically, the rise part of the Hα emission have been called *flash phase*. However, here we do not consider it as a proper phase, because it usually overlaps with the impulsive one. Finally, the remaining flare energy is thermally and radiatively dissipated. At this last stage, or decay phase, the whole system becomes quieter than before, except for the upper corona, where shock waves proceed into interplanetary space creating radio bursts and particle flux increments (Benz, 2016, [12]). Figure **1-1** summarizes the main features of the CSHKP model. The three flare phases and their signatures on the electromagnetic spectrum are shown in Figure **1-2** for a particular event.

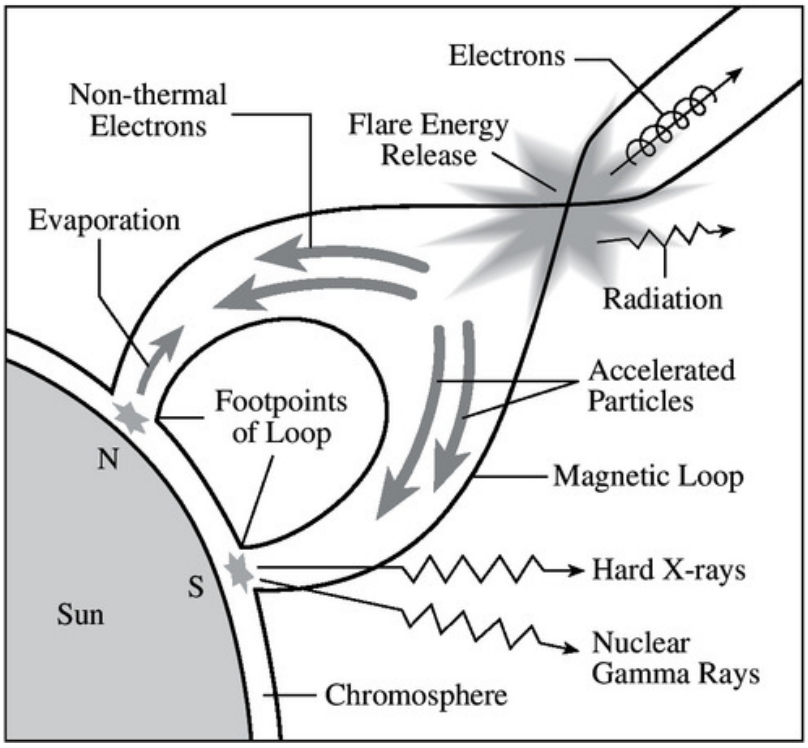

Figure 1-1.: Basic 2D representation of a solar flare. After the energy release, particles are transported through the loop until they collide with the denser part of the solar atmosphere. This causes the chromospheric evaporation, which lead to the loop population and its temperature rise. Finally the plasma inside the loop relaxes. This cartoon was taken from the archive of Professor Kenneth R. Lang, Tufts University [1].

The first detection of a solar flare was made independently by Carrington and Hodgson using a projected white-light continuum image of the Sun (Carrington, 1859, [21]; Hodgson, 1859, [58]). They reported this event, commonly known as *Carrington event*, as very bright patches that last approximately five minutes in an active region. Since then, the number of observations of solar flares increased exponentially, and even these events began to be studied from space. That was how, at the early beginnings of the space age, HXR emissions coming from solar flares were discovered with a balloon-borne mission and afterwards with the ion chambers on board of the *Orbital Geophysical Observatory* (OGO) satellites (Arnoldy et al., 1968, [3]). Nowadays, there are continuous detections of solar flares at almost all the bands of the electromagnetic spectrum, thanks to a wide network of space and ground-based solar observatories. Despite of this achievement, we are still constrained to observe events occurring at the visible side of the Sun from Earth. The only few exceptions by now have been the spacecrafts Helios, Ulysses and STEREO. In the coming years, the new missions like *Parker Solar Probe* and *Solar Orbiter* will be able to study these eruptive events, and in general the solar activity, from a closer perspective again.

[1]Image taken from `http://ase.tufts.edu/cosmos/pictures/stars/Fig6_10Solar_flare_model.jpg`

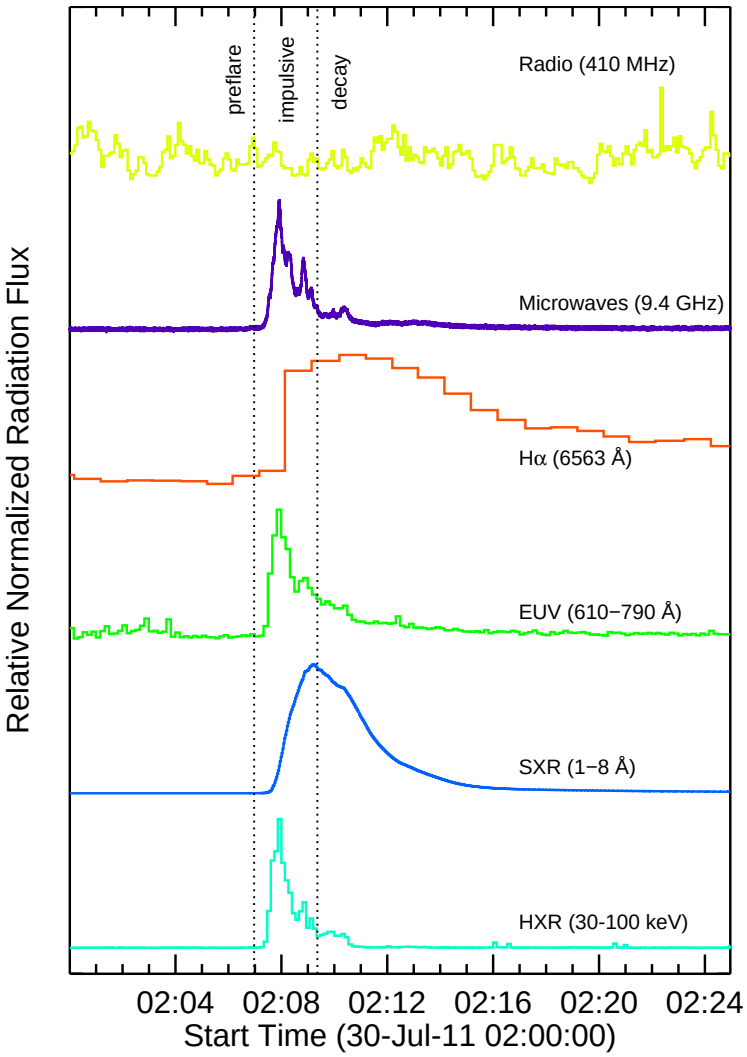

Figure 1-2.: Temporal evolution of the solar flare (SOL2011-07-30T02:09-M9.3). The HXR, SXR, EUV, Hα, microwaves, and radio data comes from RHESSI, GOES, EVE/MEGS-B, the Mauna Loa Observatory, the Nobeyama Radio Polarimeters, and the Learmonth solar radio telescopes, respectively. This particular event has no radio bursts associated, therefore its lightcurve at 410 MHz does not show any characteristic feature.

There is particular space solar observatory which is determining for the study of solar flares, the *Geostationary Operational Environmental Satellite* (GOES). The GOES mission have been operating continuously from 1976. During these four full decades it has counted with 16 satellites, from which four are currently active (GOES 13, 14, 15 and 16). The most recent of all, GOES 16, was launched in November, 2016 [2]. The GOES spacecrafts have always counted with an instrument to measure the SXR flux coming from the Sun. It is called the GOES X-Ray Sensor (XRS) and it operates at two bands, 0.5−4 Å and 1−8 Å, with a cadence of 3 seconds (Ryan et al., 2012, [96]).

[2]Information taken from `http://www.goes-r.gov/`

The SXR flux measurements of the GOES satellite in the band $1-8$ Å are used to classify solar flares. In order to identify a solar flare, GOES defines three typical times according to the data of 1-minute cadence. The flare flag is activated when the SXR signal increases monotonically during four consecutive minutes and the last data is 1.4 times greater than the first one. Then, the beginning time of the flare is the time corresponding to the first of those four consecutive data. The second relevant time is the one at which the SXR signal reaches its maximum. Finally, the end time of the flare is reported when the flux decreases to the half between the maximum and the pre-flare background level (Ryan et al., 2012, [96]).

Although the definition of these three times is important to constraint the temporal range of every single event, the relevant feature for the classification of solar flares is the maximum energy flux measured in the $1-8$ Å band. A flare is cataloged by GOES using a capital letter that represents the order of magnitude of its maximum energy flux value, followed by its respective coefficient. The correspondence between letters, also known as GOES classes, and the order of magnitude of the maximum energy flux is given in Table **1-2**. Thus, for example a solar flare whose maximum energy flux was 7.4×10^{-1} erg cm^{-2} s^{-1} is classified by GOES as a M7.4 event (Feldman et al., 1997, [40]).

Class	**W m^{-2}**	**erg cm^{-2} s^{-1}**
A	$F_{max} < 10^{-7}$	$F_{max} < 10^{-4}$
B	$10^{-7} \leq F_{max} < 10^{-6}$	$10^{-4} \leq F_{max} < 10^{-3}$
C	$10^{-6} \leq F_{max} < 10^{-5}$	$10^{-3} \leq F_{max} < 10^{-2}$
M	$10^{-5} \leq F_{max} < 10^{-4}$	$10^{-2} \leq F_{max} < 10^{-1}$
X	$F_{max} \geq 10^{-4}$	$F_{max} \geq 10^{-1}$

Table 1-2.: Assignment of the GOES classes for solar flares according to their maximum energy flux measured at the $1-8$ Å band. The classification of the event is complemented with the coefficient of the maximum energy flux value.

There are still many open issues about solar flares, from the point of view of the global solar activity and also from the perspective of the well-localized plasma processes occurring only at flaring conditions. Let us start with the global point of view. First, it is not possible to forecast precisely the occurrence of such eruptive events with the current predictive tools. Achieve a better prediction level has become one of the main goals of scientists involved in space weather, as solar flares are one of the trigger mechanisms of the disturbances that propagates on the interplanetary medium. Nowadays, the best prediction level, available for general public, is given by the *Space Weather Prediction Center* (SWPC) which is associated to the *National Oceanic and Atmospheric Administration* (NOAA). This institute counts with a 3-day forecast system, whose probabilities are based on the work of Bloomfield et al. (2012, [15]). Secondly, the coronal heating problem is

possibly explained using solar flares. The hypothesis suggests that several flares of low intensity occur all the time at the Sun. Each of those release a small amount of energy in the corona, of the order of $10^{24} - 10^{27}$ erg, but together accounts for the energy input necessary to rise the plasma temperature up to the millions of Kelvin degrees as is observed (Parker, 1988, [94]). This hypothesis is under discussion as the sensitivity of the available HXR instruments does not allow us to verify the existence of nanoflares (Glesener, Sec. 2.4.2, [49]). Other candidates capable to explain coronal heating are the energy transport along spicules (De Pontieu et al., 2009, [31]) and the damping of magnetohydrodynamic waves via a turbulent cascade (Cranmer et al., 2007, [29]).

On the other hand, some of the processes occurring at the unusual conditions of the magnetized flaring plasma remain without a clear understanding, starting from the reconnection itself. The latter is explained using mostly simplified theoretical 2D models, due to a full analytical solution of the magnetohydrodynamic (MHD) equations cannot be found (Aschwanden, Sec. 10.5.7, [5]). However, these simplified models have allowed the reproduction of many of the observed properties of solar flares, as the morphological evolution of the corresponding active region and the radiation signatures generated (Benz, 2016, [12]). The other main questions are related to the energy transport mechanism and the dynamics of the accelerated particles.

According to the standard model, the bulk energy of the flare is carried by the descending nonthermal electrons, which transfer it to ambient plasma via collisions (Brown, 1971, [16]). An alternative approach propose Alfvén Waves as the dominant transport mechanism, which additionally accelerate the charged particles near loop footpoints instead of at the reconnection region (Fletcher & Hudson, 2008, [42]). This approach represents a possible solution to the *number problem* of solar flares. The latter states that to generate the observed HXR fluxes during solar flares, almost all the available particles present in the corona should precipitate downwards.

Regarding to particle dynamics there are two aspects of interest: the dominant acceleration mechanism and the travel itself along the magnetic structure. The most accepted acceleration mechanism for the beam of descending charged particles is stochastic acceleration, i.e. they enhance their energy by successive resonant wave-particle interactions (Glesener, Sec. 2.3, [49]). Acceleration driven by electric fields or shocks are the other mechanisms to take into account. Shocks are especially relevant for the kinematics of the interplanetary medium (Benz, 2016, [12]). By its part, the travel of the charged particles inside the loop can be described by the *trapping-plus-precipitation* model. Here, the important issue is to evaluate the temporal evolution of the particle distribution using its radiation fingerprints. The aim of this work is focused just on this last idea, providing insights to the aforementioned model by making an statistical observational study.

1.2. The Impulsivity

By definition all solar flares have impulsive phase and during this stage the bulk of the flare energy, which was stored in the coronal magnetic field, is released. The *impulsivity* tell us how fast occurs such release. In this section we will show the evolution of the impulsivity concept, highlighting our new approach to it, and its already explored applications.

The first steps towards the concept of impulsivity were summarized by Dennis & Schwartz (1989, [34]). They mentioned that the emissions associated to solar flares were cataloged as *impulsive* or *gradual* depending on their temporal behavior. The former were intense and take place in short timescales, of the order of seconds or less, e.g. this is the typical case for HXR emissions. By its part, the gradual signatures have a slow evolutionary pattern, lasting some minutes or even more, like occurs with the SXR lightcurves. Then, the flare phases receive their names according to which kind of emission dominates, impulsive or gradual [1].

However, the terms impulsive and gradual were also used to characterize not just a single phase, but the flare as a whole. Solar flares were grouped into three types according to their HXR signatures (Dennis, 1988, [33]). These types are: hot thermal (compact sources with temperatures of the order of 10^7 K), impulsive (events having spike-like fast emissions), and gradual (characterized by prolonged and slow-varying emissions). Usually the hot thermal flares are not very common (Kosugi et al., 1988, [72]), therefore most of the flares are impulsive or gradual.

Some years later, Shibata redefined these two flare types using SXR instead (1996, [100]). He distinguishes a whole flare as impulsive or *Long Duration Event* (LDE) depending on its duration in the band $1 - 8$ Å. In order to compute such duration, he took the beginning and end flare times as the times at which the energy flux has decreased in a factor $1/e$ with respect to the maximum energy flux value of the event F_{max}. If the flare duration is less than one hour then it is said to be impulsive, otherwise it is LDE (K. Shibata, 2016, private communication).

The main difference between impulsive and gradual/LDE events lies on the energy release process. In the first case this release happens in a brief time interval (seconds), while in the other case occurs continuously over a longer temporal scale (several minutes). Therefore, both event types represent a qualitative distinction of solar flares according to the definition of the *impulsivity*. In fact, this apparently naive division is strengthened by two observational correlations: the temporal evolution of the spectral index and the Neupert effect.

The HXR emissions are believed to be a bremsstrahlung continuum generated by electron-ion collisions. The population of electrons follows a power-law distribution for energies greater than 20 keV (Benz, 2016, [12]). The typical temperature at the corona reaches values of millions of

[1] Here gradual refers to the decay phase seen in the previous section

Kelvin degrees, hence the thermal energy of particles ranging between 0.1 and 1 keV. Therefore, the population of electrons is purely nonthermal, as well as the radiation produced from their collisions with the ambient ions. This radiation forms a nonthermal X-ray spectrum that can also be fitted by a power-law distribution. Its associated spectral index varies along time, having two interesting evolutionary patterns: *soft-hard-soft* (SHS) and *soft-hard-harder* (SHH). In the first case the spectral index is high at the beginning of the flare, it became smaller at the maximum, and returns to be high at the end. By its part, in the SHH pattern the spectral index decreases monotonically along time. Grigis & Benz (2004, [51]) showed that impulsive events tend to follow the SHS spectral evolution, while Kiplinger found out that the SHH pattern is consistent with gradual/LDE events, which typically triggers SEPs into the interplanetary medium (1995, [65]).

On the other hand, there is an empirical relation between the X-ray emissions of a solar flare. The cumulative HXR flux is equivalent, or at least proportional, to the SXR flux. This relation is commonly called *Neupert effect* (Neupert, 1968, [91]; Hudson, 1991, [61]). The Neupert effect agrees the standard model of solar flares. The population of accelerated electrons produces HXR when collides against the ambient ions of the lower corona and the high chromosphere. The energy lost by the electrons in such collisions is stored as thermal energy in the surrounding plasma, which emits in SXR. The thermal energy of the plasma builds up until the electron injection ceases (Veronig et al., 2005, [117]). For this reason the SXR are proportional to the cumulative HXR. However, not all the solar flares satisfy the Neupert effect. Dennis & Zarro (1993, [35]) carried out a statistical study to determine in what proportion this correlation holds. They used a sample of 92 events, from which 66 were impulsive and 26 were gradual/LDE. They obtained that impulsive flares fulfilled the Neupert effect in a larger proportion (80 %) in comparison with gradual/LDE events (46 %).

In spite of the support given by the aforementioned correlations, the concept of impulsivity remains, in what has been explained so far, as a qualitative feature of solar flares. Besides it only allows the discrimination of flares in two types, impulsive or gradual/LDE. *What would we do to compare two events of the same type*? This first intuitive concept does not allow us to make such comparison. Nonetheless, the definition of the impulsivity is not just constraint to the qualitative point of view. In fact, the definition states *"how fast the energy release occurs"*, which is an utterly quantitative sentence. The first two words (*how fast*) indicate which observable we need to look for in order to describe the impulsivity. It should be something related with time, specifically some temporal range related to the energy release.

Following this way of thinking, in a previous work (Fajardo et al, 2016, [39]) we devise an observational method to estimate the impulsivity as a quantitative property of the solar flares. The observable chosen was the duration of the nonthermal X-ray emission, which it is directly proportional to the lifetime of the injected electrons, which in turn is related to the temporal scale of the energy release process.

In order to evaluate the impulsivity for a particular flare, is needed to separate the range of energies where the X-ray emission is solely nonthermal. This procedure will be explained in detail in subsection 4.1.1, although a good initial election is the band 30−100 keV. Then, the flare lightcurve over the nonthermal energy range is generated. It is assumed that the duration of the nonthermal X-ray emission corresponds to the raw width of the most prominent peak in such lightcurve (See Figure **1-3**). We also refer to this time interval as the *impulsive phase duration*.

The impulsivity must be inversely proportional to the impulsive phase duration. In other words, the shorter the impulsive phase, the faster occurs the energy release, and the more *impulsive* the flare will be. We estimate the impulsivity by means of *the impulsivity parameter* (IP), which we define as the ratio between an arbitrary normalization factor (NF), and the impulsive phase duration (IPD), i.e. IP=NF/IPD. Thus, the impulsivity parameter is a dimensionless quantity that allow us to know how impulsive a flare is with respect to any other.

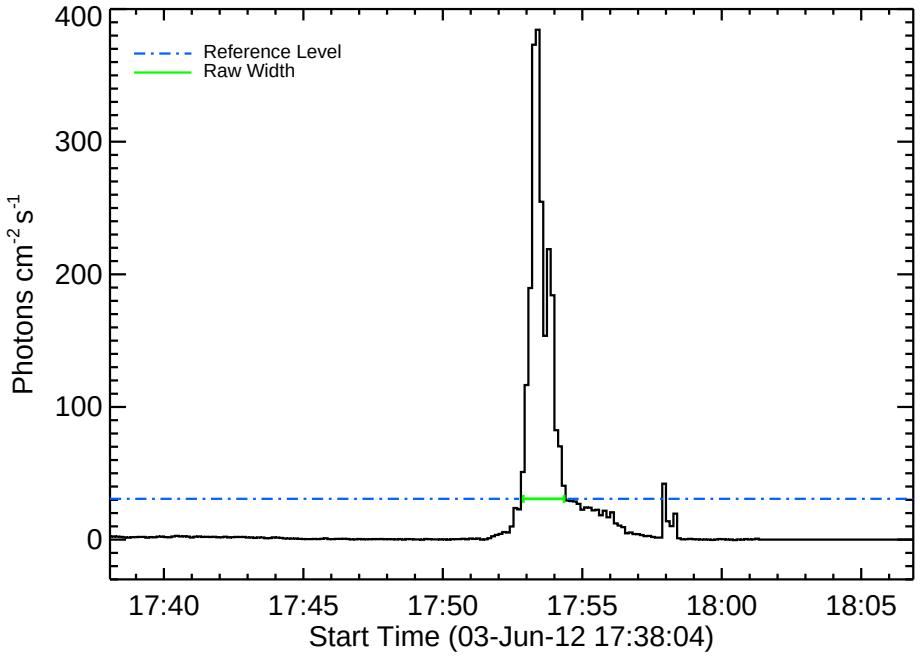

Figure 1-3.: Nonthermal X-ray lightcurve of the flare (SOL2012-06-03T17:55-M3.3). The green segment points out the raw width or duration of the most prominent emission, which is inversely proportional to the impulsivity of this event.

Additionally, we also computed how symmetric the nonthermal X-ray lightcurve looks like. For this, the impulsive phase duration was divided in two parts, the rising and decay times of the emission (RT and DT, respectively), and they were compared via another dimensionless parameter that we named *degree of symmetry* (S), S=(RT−DT)/(RT+DT). Thus, if the decay part of the

most prominent peak lasts longer than its corresponding rising part (S$>$ 0), it means that the relaxation processes take more time to develop than the energy injection processes. The opposite conclusion is inferred for the other case (S$<$ 0).

We applied the previous explained methods to estimate the impulsivity and degree of symmetry for a sample composed by 48 M class events occurred between 2008 and 2013. These events were classified according to their IP values into three types: high (IP$>$2.0), medium ($1.0 \leq$ IP $\leq$ 2.0), and low impulsive events (IP$<$ 1,0). The threshold values were chosen such that the sample was evenly distributed among the impulsivity types. Also, the events were subdivided into three morphological categories according to their S value: dominant injection (S<-0.2, INJ), symmetrical emission ($-0.2 \leq$ S ≤ 0.2, SYM) and dominant decay (S$>$0.2, DEC). Here the choice of the threshold values was made *ad hoc*. The result of applying this alternative system of classification for solar flares over the sample of 48 events is shown in Table **1-3**.

IP/S	**INJ**	**SYM**	**DEC**
HIG	1	9	5
MED	3	6	6
LOW	2	2	12

Table 1-3.: Classification system of solar flares according to the impulsivity parameter (IP) and the degree of symmetry (S). From the 48 events in the sample, 2 could not be cataloged as their nonthermal X-ray lightcurves do not show any prominent emission.

One would tend to think that this way of classifying flares depends strongly on the energy range chosen to create the nonthermal X-ray lightcurves. Nevertheless, it was proved, by using a Fisher's exact test, that such election does not alter significantly the distribution of events over the different impulsivity types. Hence, this new system of classification is statistically robust, at least for the analyzed sample. On the other hand, there is relation between the impulsivity and the degree of symmetry. It was found that the highly impulsive events are mostly symmetrical, while the low impulsive ones have in general a longer decay in comparison with its rising part. Both, the alternative system of classification for solar flares and the impulsivity-symmetry correlation are the main applications of the quantitative approach of the impulsivity concept, and lay the foundations for this thesis.

1.3. Objectives

General objective

The estimation of the impulsivity is based on an observable that is closely related to the timing of the energy release process. By studying the latter feature one could provide insights about the subsequent temporal evolution and activity of the surrounding plasma. Therefore, the impulsivity could be considered as a relevant property of solar flares.

The aim of this work is to deepen the understanding about the impulsivity concept, under the light of the standard model for solar flares and via information derived from characteristic observational signatures of the impulsive phase. Additionally, we will focus to explore the applications of the impulsivity, taking advantage of its quantitative approach which is new in solar physics, in order to get involved the solar community with this powerful observational tool.

Specific objectives

We have considered three focuses for the present study. First of all, we want to verify or deny the aforementioned applications of the impulsivity, i.e. the alternative classification system for solar flares and the impulsivity-symmetry correlation, by making use of a more representative work sample that covers a whole Solar Cycle. Secondly, the magnetic trapping inside coronal loops will be studied via its corresponding microwave emissions, in order to find the role it plays on the different types of impulsive events. Here, the description will be based on the trapping-plus-precipitation model. Finally, we will address the following scientific question: **can highly impulsive events generate other types of solar activity, particularly *sunquakes*?**. Our hypothesis lies on the fact that fast energetic releases should disturb the solar atmosphere in diverse ways, but mainly producing transient phenomena, such as sunquakes or Coronal Mass Ejections.

1.4. Outline

The rest of the document counts with five other chapters. Chapter 2 sets the theoretical background behind the HXR and microwave emissions occurring in solar flares, and how these appear according to the trapping-plus-precipitation model. In Chapter 3 the instruments, data, and the work sample used in the present study are described. The next two chapters constitute the core of this work. They are dedicated exclusively to the three focuses mentioned at the specific objectives. Chapter 4 explains the data analysis process in detail, while Chapter 5 shows the significant patterns and trends found. Lastly, Chapter 6 collect all the most relevant information of the whole work, showing its main results and its future perspectives.

2. Theoretical Background

The quantitative definition of the impulsivity seen in section 1.2 is based on the impulsive phase duration, which is estimated from the nonthermal X-ray observations of solar flares, or what is the same, from their HXR emissions. The duration of the HXR emissions depends on the acceleration mechanism involved, but also on the evolution of the nonthermal distribution of particles inside coronal loops. There is a model that describes such evolution, the so called *trapping-plus-precipitation* model of solar flares. We will start by studying each of its components separately, taking as reference the descriptions of bremsstrahlung and gyrosynchrotron radiation, which can be found in Appendix A.2. Then, the model will be exposed in order to understand when particles precipitate towards the inner layers of the solar atmosphere generating HXR, and when they are trapped inside coronal loops producing microwaves. Both emissions are typical during the impulsive phase of solar flares.

2.1. Direct Precipitation

From the standard model of solar flares seen in section 1.1, it is clear that there are highly energetic particles moving away from the reconnection site, carrying with them the bulk of the energy released by the eruptive event. As a first approximation, let us consider just electrons moving downwards, due to they achieve higher energies than the other charged particles during the same time interval, and suppose that there is not magnetic field. This descending stream of electrons dissipates its energy via Coulomb collisions with the plasma of the solar atmosphere, generating nonthermal bremsstrahlung emissions. The main hypotheses about the location of the HXR source are given by the *thin-target* and *thick-target* models, which were proposed back in the seventies (Brown, 1971, [16]).

In the thin-target model the emission takes place in the corona where the number density of the ambient plasma is low, of the order of 10^9 cm^{-3} (Forbes, Sec. 6.1.3, [44]), and hence the collision rate is small. In order to compensate this, the X-ray emitting region covers several kilometers on height. Such kind of extended HXR emissions can be seen in the corona during behind-the-limb flares (Roy & Datlowe, 1975, [95]). Another remarkable consequence of the small collision rate is that electrons are allowed to escape (Datlowe & Lin, 1973, [30]). In fact, the time structure of the HXR emissions is related to the time required by the electrons to transit or escape the thin-target (Brown, 1975, [17]).

On the other hand, in the thick-target model the nonthermal electrons get scattered continuously until reaching a layer dense enough to stop them, which is the emitting region (Hudson, 1972, [60]). This stopping layer is narrower in height than the thin-target, and is considered to be located at the upper chromosphere, where the number density is roughly 10^{14} cm^{-3} (Kontar et al., 2008, [69]). Additionally, as the breaking process happens on very short timescales, the temporal behavior of the HXR signatures reflects the evolution of the injection rate inherent to the acceleration mechanism (Brown, 1975, [17]). Figure **2-1** shows examples of thin-target and thick-target HXR emissions.

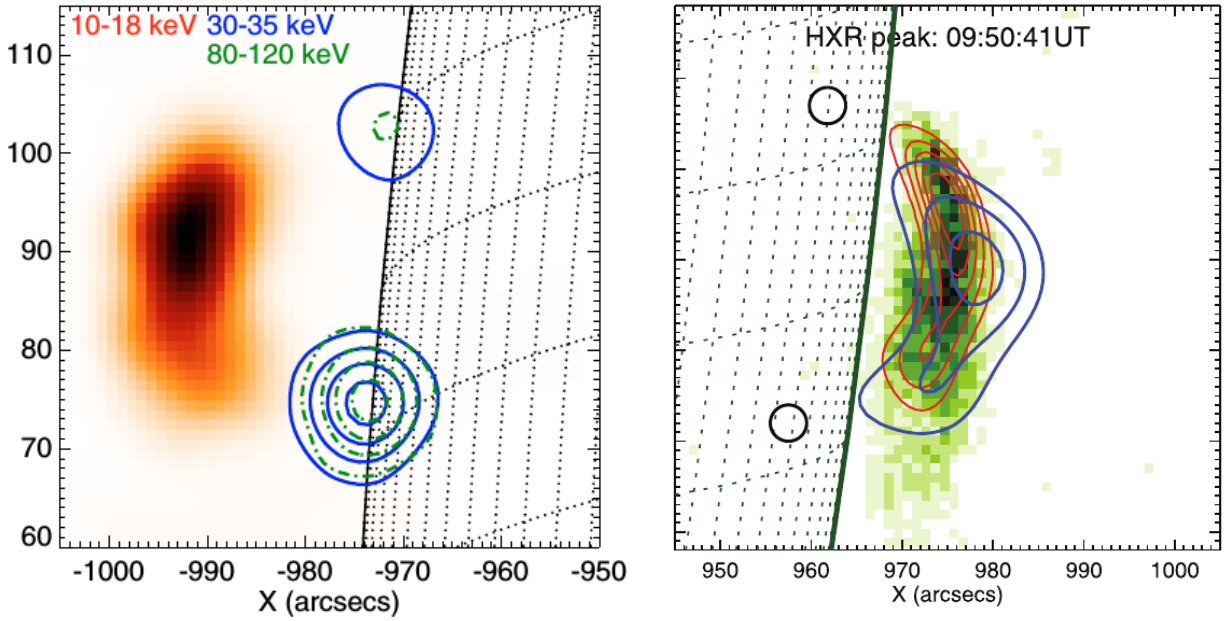

Figure 2-1.: *Left panel:* thick-target emission coming from the footpoints of the active region AR 10537 during the event (SOL2004-01-06T06:29-M5.8). The blue and green contours corresponds to HXR at 30—35 keV and 80—120 keV, respectively (Kontar et al., 2008, [69]). *Right panel:* thin-target emission associated to the event (SOL2006-11-21T09:54-B4.3). The red contours points out the thermal emission seen in the band 5—8 keV, while the blue contours show the nonthermal HXR emission at the band 18—30 keV (Krucker et al., 2007, [74]).

Regardless of the model chosen, the bremsstrahlung continuum up to a few hundreds of keV is produced predominantly by electron-ion collisions (Kontar et al., 2011, [68]). Hereafter, the discussion will be focused on this particular kind of collision, as we will work with X-ray data within this energy range (See subsection 4.1.1). Additionally, it will be supposed that the observed HXR come directly from the emitting region and it is not attributed to photospheric scattering (Kontar et al., 2011, [68]). The energy emitted per unit frequency by a single electron-ion collision is

$$\frac{dW}{d\omega} = \frac{8Z^2e^6}{3\pi c^3 m_e^2 v^2 b^2} \tag{2-1}$$

Here, Z is the atomic number of the ion, and v is the velocity of the electron. The derivation of equation 2-1 is shown in appendix A.2.2. In fact, this is the low-frequency limit of the full expression (See equation A-7). Then, this result can be expanded taking into account all the possible collisions between a single electron and a concentration of ambient ions N_i. To do this, all the contributions over the impact parameters are added up, and the energy radiated per unit frequency per unit time is found

$$\frac{dW}{d\omega dt} = \int 2\pi b N_i v \left(\frac{dW}{d\omega}\right) db \tag{2-2}$$

However, there is another approach to compute the previous quantity by using the differential cross section of the collision ($d\sigma/d\Omega$), instead of the impact parameter, according to the next relation (Aschwanden, Sec 2.3, [5])

$$2\pi b db = \left(\frac{d\sigma}{d\Omega}\right) d\Omega \tag{2-3}$$

Then, the integral of equation 2-2 is done over all the possible directions, $d\Omega$. Thus, the energy emitted per unit frequency per unit time turns out to be

$$\frac{dW}{d\omega dt} = N_i v Q(v,\omega) \qquad Q(v,\omega) = \int \frac{d\sigma}{d\Omega}\frac{dW}{d\omega} d\Omega \tag{2-4}$$

Where $Q(v,\omega)$ is the *radiation cross section*, which is function of the velocity of the electron and the angular frequency of the emitted photon. In the classical case the differential cross section corresponds to the Rutherford scattering formula, and the radiation cross section is derived from it. In fact, all the results for thermal bremsstrahlung, calculated in appendix A.2.2, can be reproduced by using the Rutherford's expression.

For nonthermal bremsstrahlung the differential cross section must be found from quantum mechanics. There, the projectiles are considered as wave packages that interact with the potential generated by the targets. The differential cross section is inferred from the asymptotic stationary states of the projectiles, before and after the collision occurs (Cohen et al., Sec. VIII-A, [27]). A comprehensive review of such calculations under different conditions and approximations was made by Koch & Motz (1959, [67]). At the nonrelativistic limit, for photon energies within the range 20−100 keV, and assuming only electron-proton collisions, due to the plasma in the solar atmosphere is mainly composed by fully ionized hydrogen (Vernazza et al., 1981, [115]; Hansteen, Sec. 8.1, [55]), the corresponding cross section per unit photon energy is

$$Q(\epsilon_e, \epsilon_p) = \frac{8}{3}\,\alpha r_e^2\,\frac{m_e c^2}{\epsilon_e \epsilon_p} \ln\left(\frac{1+\sqrt{1-\epsilon_p/\epsilon_e}}{1-\sqrt{1-\epsilon_p/\epsilon_e}}\right) \tag{2-5}$$

Here, α is the fine structure constant, r_e is the classical electron radius, ϵ_e is the energy of the electron, and ϵ_p is the energy of the emitted photon. This expression is known as the *Bethe-Heitler cross section* or *photon cross section*, and is often used in analytical descriptions of nonthermal bremsstrahlung (Brown, 1971, [16]; Aschwanden, Sec. 13.2.1, [5]). The photon cross section is related to the radiation cross section via $Q(v, \omega) = \hbar \epsilon_p Q(\epsilon_e, \epsilon_p)$.

Now, we are able to compute the electron-ion bremsstrahlung continuum produced by the flaring plasma in the solar atmosphere, regardless the location of the emitting source, tenuous corona or dense chromosphere, i.e. thin-target or thick-target, respectively. Here, it will not be considered the directivity of the HXR emission, so all the mentioned quantities are averages over all directions (Kontar et al., 2011, [68]). Hence, it is assumed that the source is not spatially resolved. The HXR flux per unit photon energy measured by an observer located at a distance R from the source depends on the photon cross section of the electron-ion collision $Q(\epsilon_e, \epsilon_p)$, the velocity of the electrons $v(\epsilon_e)$, and the total number of collisions, which is the integral over the volume of the emitting source of the product between the ambient proton number density n_p, and the electron number density per unit energy $n(\epsilon_e)$ (Brown, 1971, [16])

$$I(\epsilon_p) = \frac{dN_p}{dA dt d\epsilon_p} = \frac{1}{4\pi R^2} \int_{\epsilon_p}^{\infty} Q(\epsilon_e, \epsilon_p) v(\epsilon_e) \left(\int_V n_p n(\epsilon_e) dV \right) d\epsilon_e \tag{2-6}$$

In general, n_p is not uniform within the emitting volume. Then, the integral over V turns out to be the product of the averaged proton density n_0, and the effective electron spectrum at the emitting source $N(\epsilon_e)$ that produces the observed HXR emission

$$n_0 = \int_V n_p dV \qquad \int_V n_p n(\epsilon_e) dV = n_0 N(\epsilon_e) \tag{2-7}$$

In the thick-target model, the effective electron spectrum at the emitting source $N(\epsilon_e)$ is different from the injected electron spectrum $f(\epsilon_e)$, as the latter is affected by the collisional losses throughout its descending travel from the reconnection site to the emitting region (Aschwanden, Sec. 13.2.2, [5]). By its part, in the thin-target model the injection and emitting regions are the same, then both electron spectra are almost identical (Aschwanden, Sec. 13.2.3, [5]).

Let us write the observed HXR photon flux per unit photon energy $I(\epsilon_p)$ in terms of the injected electron spectrum $f(\epsilon_e)$ according to the thick-target model (Brown, 1971, [16])

$$I(\epsilon_p) = \frac{1}{4\pi R^2} \int_{\epsilon_p}^{\infty} f(\epsilon_{e0}) \nu(\epsilon_p, \epsilon_{e0}) d\epsilon_{e0} \tag{2-8}$$

Here, $\nu(\epsilon_p, \epsilon_{e0})$ is the total number of photons of energy ϵ_p produced by an electron whose initial energy was ϵ_{e0}. Such photons can be emitted as long as the energy of the electron remains greater than ϵ_p. Therefore, $\nu(\epsilon_p, \epsilon_{e0})$ obeys to

$$\nu(\epsilon_p, \epsilon_{e0}) = \int_{\epsilon_e=\epsilon_{e0}}^{\epsilon_e=\epsilon_p} Q(\epsilon_e, \epsilon_p) n_p v(\epsilon_e) \left(\frac{d\epsilon_e}{dt}\right)^{-1} d\epsilon_e \tag{2-9}$$

The term, $d\epsilon_e/dt$, represents the collisional energy loss rate of an injected electron of energy ϵ_e

$$\frac{d\epsilon_e}{dt} = -\frac{K n_p v(\epsilon_e)}{\epsilon_e} \tag{2-10}$$

Where K can be effectively considered as constant within the energy range 20−100 keV (Brown, 1971, [16]). Replacing the collisional energy loss rate in expression 2-9, it is found that $\nu(\epsilon_p, \epsilon_{e0})$ does not depend on the number density of the ambient protons nor on the electron velocity. Additionally, substituting the new form of $\nu(\epsilon_p, \epsilon_{e0})$ in equation 2-8 it is obtained the observed HXR spectrum generated by an injected electron spectrum in the thick-target model.

Brown (1971, [16]) developed an analytical method to find both electron spectra, at the emitting source $N(\epsilon_e)$ and the injected one $f(\epsilon_e)$, from the observed HXR emission $I(\epsilon_p)$. He solved this inversion problem from equations 2-6 and 2-8, respectively. Both cases turn out to be Abel's integral equations for the respective electron spectrum. Taking the observed HXR emission as a power-law of the form $I(\epsilon_p) = I_0 \epsilon_p^{-\varphi}$, then the injected electron spectrum would be also a power-law, $f(\epsilon_e) = f_0 \epsilon_e^{-\delta}$. The relation between both exponents is $\delta = \varphi - 0.5$ in the thin-target model, and $\delta = \varphi + 1$ in the thick-target model (Hudson, 1972, [60]). Therefore, in order to reproduce the observed HXR emission the thick-target model requires an injected electron spectrum 1.5 powers steeper or *softer* than the one predicted by the thin-target model. This relation between the indexes δ and φ is a powerful tool to diagnostic the form of the electron spectrum, taking into account just which model fits better on the observational data.

2.2. Magnetic Trapping

The descending beam of nonthermal charged particles that interact with the ambient plasma and deposit its energy via collisions, as was seen previously, is embedded inside magnetic flux tubes, also called coronal loops. The focus of this subsection will be to study how these dynamical structures of magnetic field affect the evolution of the charged particles, which leads to the phenomenon known as *magnetic trapping*.

The motion of a charged particle in the presence of a constant magnetic field traces out a spiral trajectory that can be decomposed in two parts: a linear motion along the magnetic field direction with velocity $v_{||}$, and a circular motion around the field lines with velocity $v_{\perp}$ (See appendix

A.2.3). Besides, the kinetic energy of the particle is invariant, due to the magnetic field does not exert work on it. Let us now discuss another physical feature of this spiral trajectory. Consider the orbit of the charged particle as a wire at which passes an electric current $I = q/\tau$, where q is the charge of the particle, and τ its period of gyration. In one single orbit, the wire almost enclosed itself generating a surface of area $A = \pi r_g^2$, where r_g is the radius of gyration of the particle (See equation A-13). Then, the magnetic moment of the wire is (Longair, Sec. 7.2.1, [82])

$$\mu = IA = \frac{qv_\perp r_g}{2} = \frac{cmv_\perp^2}{2B} = \frac{cE_\perp^{kin}}{B} \tag{2-11}$$

Thus, the magnetic moment of the charged particle moving in a constant magnetic field depends on the ratio between the perpendicular kinetic energy of the particle and the magnetic field strength. To achieve this previous result, it was used the relation $\tau = 2\pi r_g/v_\perp$, and the definition of the radius of gyration in the non-relativistic limit (See equation A-13).

Now, let us assume a magnetic field configuration that changes slowly with time, or that is non-uniform in space having slight magnetic flux concentrations or gradients. In either case, the charged particle experiences a small change in the magnetic field strength ΔB after one single orbit, i.e. after the gyration period τ. According to the Faraday's law, this small variation of the magnetic field along time produces an electric potential difference affecting the motion of the charged particle. The work done by this small voltage, slightly changes the perpendicular kinetic energy of the particle as follows (Longair, Sec. 7.2.1, [82])

$$\Delta E_\perp^{kin} = q\Delta V = \frac{q}{c}\frac{\Delta B}{\tau}\pi r_g^2 = \frac{\Delta B}{B}E_\perp^{kin} \tag{2-12}$$

In the intermediate steps, the gyroradius and the period of gyration were replaced as before. Now, our interest is to compute the variation of the magnetic moment during a single orbit. To do this, it is necessary to take into account the result of equation 2-12

$$\Delta\mu = c\Delta\left(\frac{E_\perp^{kin}}{B}\right) = c\left(\frac{\Delta E_\perp^{kin}}{B} - \frac{E_\perp^{kin}\Delta B}{B^2}\right) = 0 \tag{2-13}$$

Despite the small variation in the magnetic field strength, the magnetic moment remains constant. This is one of the three adiabatic invariants of the motion of a charged particle embedded in a slowly-varying magnetic field (Öztürk, 2012, [93]). Any kind of variation, increment or decrement, in the magnetic field strength must be compensated with an equivalent change in the perpendicular kinetic energy of the particle, in order to keep the magnetic moment invariant. For example, when a charged particle moves towards a region of positive magnetic field gradient, its perpendicular kinetic energy increases, while its parallel component decreases, as the total kinetic energy must be constant $E^{kin} = E_{||}^{kin} + E_\perp^{kin}$ (See appendix A.2.3). So, the perpendicular kinetic energy of the particle reaches its maximum value when the motion is uniquely perpendicular, $E_{||}^{kin} = 0$. At this point, the charged particle cannot keep moving in the direction of the

positive magnetic field gradient, and it is reflected back along the field line. This phenomenon is known as *magnetic mirroring*, holds even for relativistic particles (Longair, Sec. 7.2.1, [82]), and it is a consequence of the invariance of the magnetic moment.

How is the magnetic mirror effect related to the motion of the plasma in the solar atmosphere? Well, loops in the solar atmosphere present naturally gradients of magnetic field. The coronal part of a typical solar loop has a smaller magnetic field strength than its chromospheric footpoints, as the latter are closely linked to zones of abundant magnetic flux emergence, i.e. to active regions (Dulk, 1985, [36]). In these structures the magnetic mirror effect modifies the dynamics of the descending beam of particles, due to the reflections occurring near footpoints, impeding their escape or, what is the same, their precipitation over the denser layers of the solar atmosphere. This is the reason why we say in heliophysics, that particles can be *trapped* in the coronal magnetic field. Another typical example of magnetic trapping can be found in the Earth's magnetosphere, where charged particles bounce at 2 or 3 Earth's radii between regions close to the Earth's magnetic poles, generating the famous Van Allen radiation belts (Öztürk, 2012, [93]).

So far, our discussion have been focused on explaining the magnetic mirror effect as a consequence of the magnetic moment invariance, and how the latter depends on the variations of the perpendicular kinetic energy of the particle and the magnetic field strength. However, this invariance can also be written in terms of the *pitch angle*, which is defined as the angle between the velocity of the particle and the magnetic field, which lead us to the concept of the *loss cone*. To do this, the next relations for the perpendicular momentum of the particle are required, $E_{\perp}^{kin} = p_{\perp}^2/2m$ and $p_{\perp} = p\sin\alpha$, where α is the pitch angle. Substituting into equation 2-11 and having in mind the invariance of μ, it is obtained

$$\mu = \frac{cp_{\perp}^2}{2mB} = \frac{cp^2\sin^2\alpha}{2mB} = cte \quad \longrightarrow \quad \frac{\sin^2\alpha}{B} = cte \tag{2-14}$$

Let us apply this result to a solar magnetic loop. Choose two points on the magnetic structure, namely, the point of highest altitude or apex (labeled with the subscript *top*) and the mirror point at which the charged particles bounce (labeled with the subscript *bot*). At the mirror point, the motion of the particle is exclusively perpendicular, then $\sin\alpha_{bot} = 1$. Using the equation 2-14, it is possible to infer the pitch angle of the particle at the apex, as function of the ratio between the magnetic field strengths at the aforementioned points in the loop (Somov, Sec. 6.2.2, [106])

$$\frac{1}{B_{bot}} = \frac{\sin^2\alpha_{top}}{B_{top}} \qquad \alpha_{top} = \sin^{-1}\sqrt{B_{top}/B_{bot}} \tag{2-15}$$

In fact, α_{top} is a critical parameter that decides the fate of the charged particles inside the magnetic structure. All the particles having an initial pitch angle less than α_{top} precipitates towards the converging legs of the loop and are not reflected back, then they escape from the magnetic trap. The region covered by such pitch angles, $\alpha < \alpha_{top}$, is the previously mentioned loss cone.

On the other hand, particles having pitch angles within $\alpha > \alpha_{top}$ are trapped, and bounce between the converging legs. Eventually, they lose enough energy via Coulomb collisions or other interactions, reducing their pitch angles until entering to the loss cone. In Figure **2-2** a sketch shows the alternatives for the motion of a charged particle according to its pitch angle.

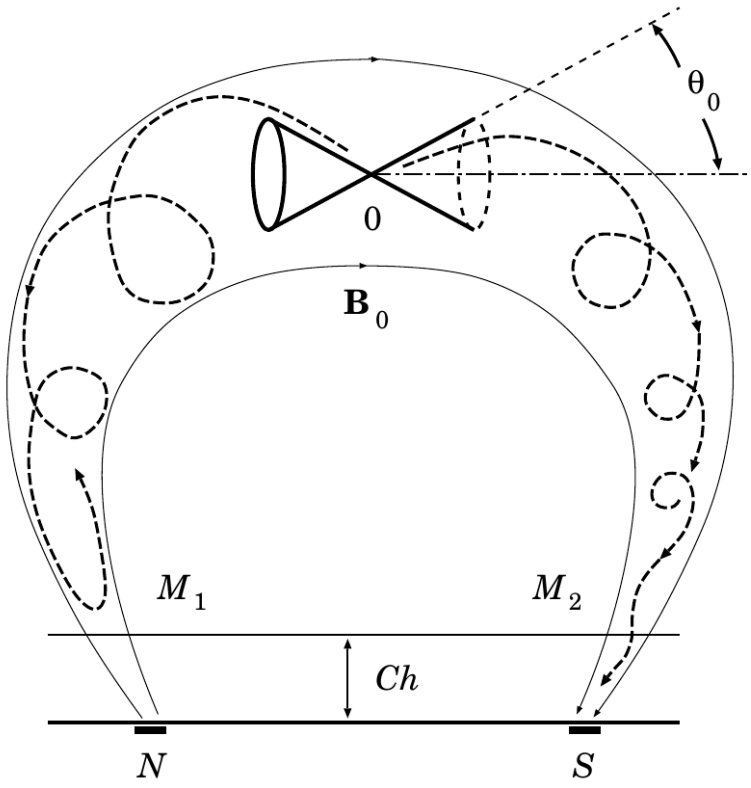

Figure 2-2.: The aperture angle of the loss cone at the apex, here labeled as θ_0, is defined as appears in expression 2-15. If the pitch angle of the particle is within the loss cone, then the particle precipitates (trajectory towards the right leg). Otherwise it bounces back and gets trapped (trajectory towards the left leg). The region labeled with *Ch* denotes the location of the chromosphere. This image was taken from Somov (Sec. 6.2.2, [106]).

The trapped particles in the solar flaring loops are usually midly-relativistic electrons, with energies of 0.1−1.0 MeV, and they are often well described by a power-law distribution over energy (Dulk, 1985, [36]). These electrons produce the microwave emissions observed during the impulsive phase via gyrosynchrotron radiation. Assuming that the distribution of electrons is isotropic over pitch angles, then the energy emitted per unit time per unit frequency per unit volume and per unit solid angle by such distribution is

$$\frac{dW}{dV\,d\nu dt d\Omega} = 3{,}3 \times 10^{-24}(Bn_e)10^{-0{,}52p}(\sin\theta)^{-0{,}43+0{,}65p}\left(\frac{\omega}{\omega_g}\right)^{1{,}22-0{,}90p} \tag{2-16}$$

Here B is the magnetic field strength, n_e is the number density of electrons with energies greater than 10 keV, θ is the direction of propagation of the gyrosynchrotron radiation, and p is the power-index of the distribution of electrons. This empirical expression holds for frequencies $\omega \geq 10\,\omega_g$, and was derived by Dulk & Marsh (1982, [37]). At lower frequencies the absorption process related to gyrosynchrotron radiation becomes important, and the emission becomes optically thick. At this regime the observed spectrum is described by an increasing power-law with a positive power-index between [0,10] (Benz, Sec. 8.1.2, [11]).

2.3. Trapping Plus Precipitation Model

The direct precipitation of electrons in the solar atmosphere and their trapping in coronal loops generate the HXR and microwave emissions of solar flares, respectively. Both kind of emissions can be derived from the trapping-plus-precipitation model. This model explains how the transport of an injected distribution of electrons throughout the evolving magnetic loop modulates the temporal behavior and intensity of the HXR and microwave emissions.

The first steps towards the current trap and precipitation model were made by Takakura & Kai (1966, [110]) and Melrose & Brown (1976, [88]). They made the distinction between the two emitting regions, the trapping and precipitating zones, located at the tenuous corona and at the chromospheric footpoints, respectively. In this context, the bulk of the HXR emission is considered to be thick-target. The dynamics of both regions is related via the parameter ν, which represents the escape rate of the magnetic trap and also the precipitation rate towards the highly collisional thick-target. Thus, under this simple picture the temporal behavior of HXR and microwave emissions will be pretty well correlated as they depends only of ν. However, this is not always the case as is revealed by observations (Lee, Sec. 9.2.1, [77]).

A significant improvement to this classical picture, that allows the temporal independence of HXR and microwave radiation, was made by Aschwanden (1998, [4]). He separates the injected distribution of electrons $Q(E, \alpha, t)$ into two populations according to the critical pitch angle α_{top} defined in expression 2-15. All the injected electrons within the loss cone ($\alpha < \alpha_{top}$) precipitate directly towards the thick-target region. The remaining injected electrons ($\alpha > \alpha_{top}$) are trapped in the magnetic structure and escape from it at a rate ν. Assuming a collisionless trap, i.e. that the transport through the magnetic structure is not affected by interactions such as Coulomb collisions, the evolution of the number density of the trapped particles N and the precipitation rate into the thick-target $\dot{n}$ is

$$N = \int_0^t \exp[-\nu(t-t')]Q(E, \alpha^+, t')dt' \tag{2-17}$$

$$\dot{n} = Q(E, \alpha^-, t) + \nu N$$

This expression is derived from the Fokker-Planck equation that describes the electrons inside the trap (Lee, Sec. 2, [77]). Here, ν is the escape rate, Q is the injection rate, and the symbols α^+ and α^- denotes the trapped and directly precipitating populations of injected electrons, respectively. In this formulation there are two limits of interest. First, when the critical pitch angle is null ($\alpha_{top} = 0$) the loss cone is empty and there is not direct precipitation. Therefore, the HXR emission comes solely from the escaping electrons. In the other limit, if the escape rate is extremely large, then the electrons are entirely untrapped and microwave emission should be absent.

The effect of collisions in the model have been neglected hitherto, although this is relevant as forces the electrons to enter into the loss cone. This effect is known as *pitch angle diffusion* and it can occur at different regimes. When the loss cone is empty and only Coulomb collisions are important the regime is called weak diffusion (Lee, Sec. 9.4.1, [77]). Under these conditions the microwave emission traces out the geometry of the emitting region, showing in some cases the asymmetry of the magnetic field strength in a given loop (Lee & Gary, 2000, [78]). Other collision regime is intermediate diffusion, in which the loss cone is filled with scattered particles, and the precipitation rate ν depends on the square of the electron energy (Lee, Sec. 9.4.2, [77]). Additionally, the entire loop becomes accessible for electrons, thus making the microwave emission to be concentrated in symmetric footpoints (Lee, Sec. 9.4.4, [77]). Lastly, strong diffusion operates when the mean free path is less than the loop length, therefore the electrons cannot even bounce between the mirror points. Consequently, the electron are not being trapped by the magnetic field, but by the collisions within the scattering region (Lee, Sec. 9.4.3, [77]).

So far, it has been shown that the evolution of the electron distribution inside the loop depends on the critical pitch angle α_{top}, and that electrons enter into the loss cone via collisions during its travel inside the loop. However, it has not been considered the temporal evolution of the loop during the flare. Such evolution changes the loop geometry, and consequently the critical pitch angle. Aschwanden (2004, [6]) proposed a theoretical model in order to explain the evolution of a flaring loop under a 2D approach. Before the flare occurs, the solar loop has a highly elongated shape, with an apex located at the reconnection region. After the energy is released via magnetic reconnection, the loop relaxes into a more stable configuration, that is force-free and quasi-circular (Aschwanden, 2004, [6]). Thus, the height of the apex decreases with time as follows

$$h(t) = h_L + (h_x - h_L)\exp(-t/t_R) \tag{2-18}$$

Where, h_x and h_L are the heights of the apex before the flare occurs and after the loop relaxes, respectively. The factor t_R represents the relaxation timescale, which is defined by $(h_x - h_L)/v_A$, where v_A is outflow speed of the reconnection region, i.e. the Alfvén speed. Additionally, as the loop collapses the critical pitch angle at the apex evolves along time. Initially the loss cone is closed ($\alpha_{top} = 0$), and when the loop reaches the quasi-circular shape the loss cone fully opens up ($\alpha_{top} = \pi/2$). Then, the critical pitch angle gradually increases over time as

$$\alpha(t) = \frac{\pi}{2}\left[1 - \exp\left(-\frac{t}{t_I}\right)\right] \tag{2-19}$$

Here, t_I denotes the injection timescale, which is function of t_R, and of the *magnetic length scale* L_B. The latter is the distance from the X-point where the magnetic field strength is the half of the asymptotic value observed outside the reconnection region, assuming the Petschek-type reconnection model (Aschwanden, 2004, [6]). Figure **2-3** shows the temporal evolution of the loop geometry and the loss cone according to this dynamic trap model.

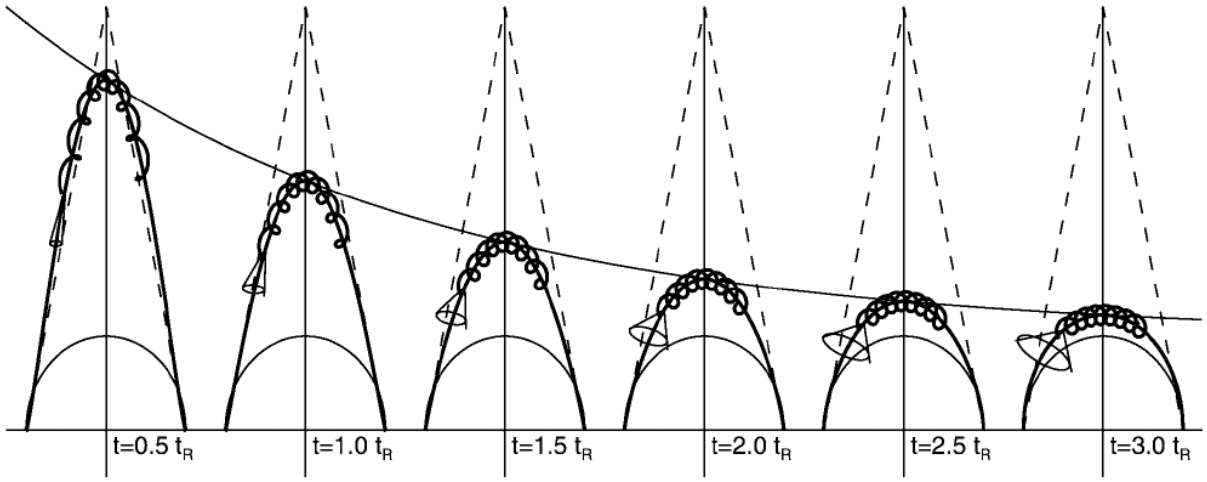

Figure 2-3.: Sketch of the evolution of a dynamic trap. After the reconnection, the loop relaxes to a quasi-circular configuration and the loss cone gradually opens up. Both processes are scaled by the relaxation time t_R. This was taken from Aschwanden (2004, [6]).

Aschwanden (2004, [6]) uses this theoretical model of a dynamic magnetic trap as a tool to reproduce the observed pulsed HXR emissions of solar flares, whose Full Width at Half Maximum (FWHM) are of the order of 0.1−1.0 s. To do this, it has to be assumed that the injected electrons follows an isotropic distribution over pitch angles. The duration of these pulses does not depend on energy, it just corresponds to the transit time of the magnetic length scale L_B at the Alfvén speed. Additionally, these pulsed emissions are in concordance with a bursty reconnection scenario (Kliem et al., 2000, [66]).

Besides the pulsed HXR emissions, the trapping-plus-precipitation model is able to describe a wide range of observed HXR and microwave signatures of solar flares. Depending on the time structure of these signatures it can be inferred whether direct precipitation, precipitation due to escaping from the trap, or magnetic trapping dominates the transport of electrons in a given event. Two of the most common observed signatures, on both spectral windows, are single bursts and multiple bursts. The first case is associated to impulsive flares that present a sharp

peak in HXR, and a corresponding emission well correlated temporarily in microwaves. The main difference between them is the duration of the burst, which is longer in microwaves due to a slow-decaying component. Such delay addresses the effect of magnetic trapping, while the duration of the HXR peak gives a constraint of the direct precipitation, i.e. the one due to $Q(E, \alpha^{-}, t)$ (Lee, Sec. 9.3.1, [77]). In the second case, many peaks protrude over a smooth continuum envelope on both emissions. Each peak represents a single injection, while the entire envelope gives account of the cumulative population of trapped electrons (Lee, Sec. 9.3.2, [77]).

There is another typical scenario where HXR and microwaves are not well correlated in time. This is because either the trapping is extremely efficient or they are decoupled by an external effect as strong diffusion (Lee, Secs. 9.3.3 & 9.3.4, [77]). All the aforementioned examples demonstrate the versatility of the trapping-plus-precipitation model. More insightful conclusions about the transport of electrons inside the loop are achieved when imaging and spectroscopy are integrated into the analysis (Lee, Sec. 9.6, [77]).

Now, let us talk about the population of electrons that propagates inside the evolving magnetic trap. Such nonthermal electrons are supposed to generate the HXR and microwave emissions of solar flares (Bastian et al., 1998, [10]). If so, the spectral indexes of the both observed emissions should be related. Assuming that the distribution of electrons has a power-law form, $N(E) = CE^{-p}$, then the observed HXR emission would be $I(\omega) = I_0\omega^{-\varphi}$, and the optically thin part of the microwave radiation would be $I(\omega) = I_0\omega^{-s}$. There are two options for spectral index of the HXR. The choice depends on whether the thin-target model or the thick-target model is considered (See section 2.2). Likewise, the spectral index for microwaves has two cases, for ultra-relativistic or midly-relativistic electrons, i.e. considering synchrotron or gyrosynchrotron radiation, respectively (See equations A-21 and 2-16). In Table **2-1** all the possible relations between the spectral indexes φ and s are derived (Benz, Sec. 8.1.2., [11]).

	Thick-target	**Thin-target**
Gyrosynchrotron	$\varphi = 1{,}11s + 0{,}36$	$\varphi = 1{,}11s + 1{,}86$
Synchrotron	$\varphi = 2s$	$\varphi = 2s + 1{,}5$

Table 2-1.: Assuming that HXR and microwave radiation of solar flares are emitted by the same population of electrons, the spectral indexes of both kind of emissions, φ for HXR and s for microwaves, are related under different radiative regimes.

In the seventies, it was found observationally that the population of nonthermal electrons producing the microwave emission should be one hundred to one thousand bigger than the respective population from which HXR comes from. This evidence disagrees with the trapping-plus-precipitation model, and in fact, it was one of the biggest issues the model faces. However, this

discrepancy was solved by using the thick-target model for describing the bulk of the HXR emission (Hudson, 1972, [60]). Moreover, improved observations has demonstrated the HXR and microwave emissions are well correlated temporarily, spatially, and may be produced by electrons with similar energies, within the range 10—200 keV (Bastian et al,. 1998, [10]).

In summary, the trapping-plus-precipitation model for solar flares explain that HXR and microwave emissions are produced by the same population of electrons. After leaving the acceleration site, the charged particles enter into an evolving closed magnetic structure from which can escape directly or after some reflections at the mirror points, producing HXR via collisions with the denser layers of the solar atmosphere. Otherwise electrons are trapped in the coronal loop, thus emitting gyrosynchrotron radiation. Therefore, both emissions are complementary and together can give us a comprehensive picture about the transport of the injected distribution of particles inside the magnetic structure.

3. Instruments and Data

In order to study the impulsivity of solar flares we will analyze only the characteristic emissions of the impulsive phase according to the trapping-plus-precipitation model, namely, HXR and microwave radiation. Hence, this Chapter will be devoted to the description of the solar observatories from which we acquire both kind of data. Also, the criteria used to select the work sample are explained in detail, and all the events that fulfilled them are presented in a list.

3.1. Reuven Ramaty High Energy Solar Spectroscopic Imager

The *Reuven Ramaty High Energy Solar Spectroscopic Imager* (RHESSI) is a Small Explorer mission of NASA, belonging to the Explorers program which funds space missions for heliophysics and astrophysics[1]. The main scientific objectives of RHESSI are to understand the behavior of energy and particles during solar flares. This includes processes that take place at the onset of the eruptive phenomena, e.g. the initial energy release and particle acceleration, and also those occurring along its temporal evolution, like the transport of energy and particles in the magnetized solar plasma (Lin et al., 2002, [80]).

The RHESSI spacecraft have a circular geocentric orbit at a constant height of 600 km, and an inclination of 38^o with respect to the Earth's equator (Lin et al., 2002, [80]). The period of its orbit is nearly 45 minutes. For this reason the detection of solar HXR sources is often interrupted by eclipses with Earth and passes through the South Atlantic Anomaly (SAA). The latter is a region where the magnetic field strength of the Earth is pretty low. Then, when the instrument crosses it the detectors stop working for solar signals, in order to protect all the electronic systems, and begins to operate for studying the dynamics of the SAA (Hajdas et al., 2004, [53]).

Additionally, the whole spacecraft is rotating around its main axis at an average frequency of 15 rpm, i.e. its period of rotation is roughly 4 seconds. Despite this nearly constant rotatory motion, RHESSI is pointing at the Sun all the time, thanks to two of their parts: the Solar Aspect System (SAS) and the Roll Aspect System (RAS). They compute the position of the center of the Sun within a precision of $1.5''$ and the angle of rotation of the spacecraft, respectively (Fivian et al., 2002, [41]). Both measurements are made with respect to the position of the background stars.

[1]More information about Explorer Missions in: `https://explorers.gsfc.nasa.gov/missions.html`

The data generated by RHESSI are images and spectra in a wide range of energies, namely, from 3 keV to 17 MeV. Then, it is possible to obtain information of SXR, HXR and gamma-ray solar sources thanks to this instrument. Besides, both RHESSI capabilities can be combined to generate a spectrum at each pixel of an image. This technique is known as *imaging spectroscopy* and it was revolutionary at the time RHESSI begins to operate, because it was the first time that such technique was applied for high energies (Lin et al., 2002, [80]). In what follows it will be explained, without enter in the specific details, how imaging and spectroscopy works by separate.

There are two methods to generate images at high energies, namely, direct focusing and indirect imaging. The former is used by the new generation of HXR instrumentation like NuSTAR and the *Focusing Optics X-ray Solar Imager* (FOXSI) (Wright et al., 2017, [118]; Krucker et al., 2014, [73]), while the latter is the method behind the RHESSI imaging concept (Hurford et al., 2002,[62]).

Specifically, RHESSI uses a modulation technique to generate its X-ray and gamma-ray images. At the front part of each of the nine RHESSI detectors there are a pair of grids, separated between them by about 155 cm. All the pair of grids have different specifications, like spacing and thickness, which gives account to the different spatial resolution of the detectors (Hurford et al., 2002, [62]). The proper name of the system of grids is *Rotating Modulation Collimators* (RMCs), and one of its two identical parts can be seen at the panel (b) in Figure **3-1**. As the spacecraft is rotating the RMCs modulates the X-ray signal coming from the Sun, generating a pattern of light and dark fringes that receive the detectors. The images are reconstructed from this received pattern via a Fourier-transform analysis. There are many reconstruction algorithms, among which are back-projection, clean, pixon, forward-fitting, and some others. For more information about the reconstruction techniques we suggest Hurford et al. (2002, [62]).

In order to generate a good science image just half a rotation is necessary, thus the cadence of the instrument is 2s (Lin et al., 2002, [80]). Nonetheless, this cadence can be higher if the number of photons reaching the instrument is low. This happens for example in GOES C-class events. Then, a longer integration time is required for getting better statistics in the space of frequencies, thus allowing the image reconstruction. By its part, the angular resolution of an image is given by the combinations of the signals from the nine RHESSI detectors. The angular resolution varies depending on the energy range considered; it is 2 arcseconds from 3 keV to 100 keV, 7 arcseconds in the range 100-400 keV, and 36 arcseconds above 400 keV (Hurford et al. 2002, [62]).

Now, let us talk about the spectroscopy technique. As was already mentioned RHESSI has nine detectors, which are located behind the RMCs. These detectors are made of pure germanium, slightly n-type doped, and have dimensions of 7.1 cm in diameter and 8.5 cm of long (Lin et al., 2002, [80]). Each detector is segmented in two parts, namely, front and rear as is shown in panel (c) of Figure **3-1**. The front part is set to receive the low energy photons (up to 100 keV) and has

a thickness of 1.5 cm, while the rear is just sensitive to high energies and its thickness is of 7 cm (Smith et al, 2002, [105]). Any photon reaching the instrument generates an electric current in the corresponding part of the detector, whose intensity is directly proportional to the photon energy (Smith et al, 2002, [105]). When the number of counts is high, the electric currents of two low energy photons can be summed up, and then RHESSI consider them as one single photon. This effect is known as *pile-up* and it is common during the detection of major flares.

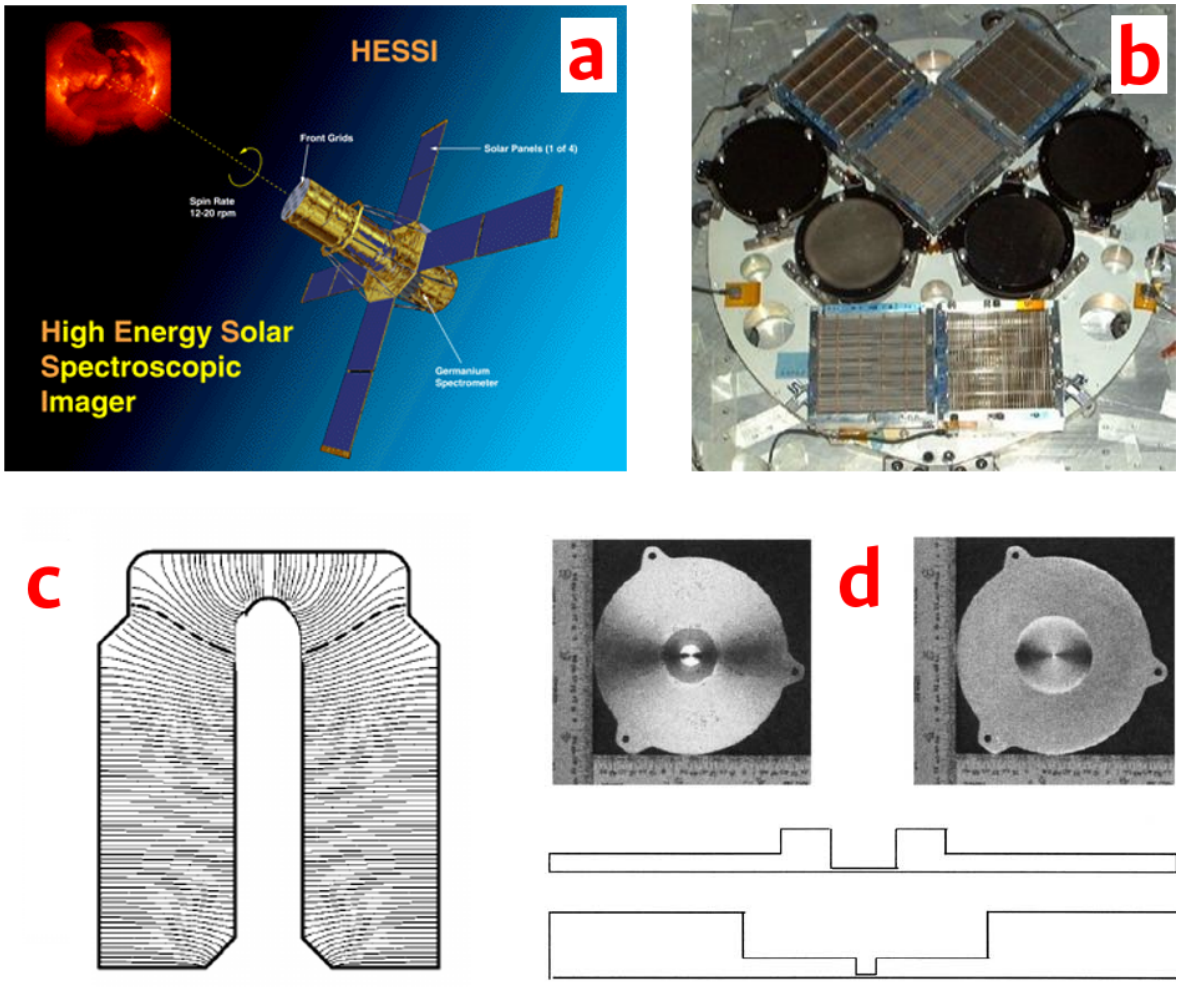

Figure 3-1.: Collage of images about RHESSI. *Panel a*: sketch of the spacecraft. *Panel b*: grid array for the nine detectors. A pair of grids like this composed the RMCs. *Panel c*: segmented detector of Germanium. The dashed line marks the separation between the front (upper region) and rear parts (lower region). *Panel d*: thin (left) and thick (right) attenuators. Here there are shown their top and side views [2].

[2]The images of *Panels a* and *b* were taken from `https://hesperia.gsfc.nasa.gov/hessi/challenge.htm` and `https://hesperia.gsfc.nasa.gov/hessi/frontgridframe.htm`, respectively. The images of the other panels were extracted from Smith (2002, [105]).

The detectors must be at a temperature of 75 K to operate correctly. In consequence, they are mounted on a common coldplate, which is refrigerated by a Stirling cryostat. This system ensures the required low temperature and also the thermal insulation (Smith et al., 2002, [105]). Other part of the spacecraft that take care of the detectors are the attenuators. These are two circular films of aluminum of different thicknesses, thin and thick, and are located above the front part of each detector, but behind the RMCs. They do not have a homogeneous shape as can be seen at the panel (d) of Figure **3-1**. The attenuators are used to cover the spectrometer entrance when the counts number is high enough that saturates the detectors (Smith et al., 2002, [105]). They have four modes to operate, which are also known as attenuation states. These are: (A0) both attenuators are out, (A1) the thin attenuator is in, (A2) the thick attenuator is in, and (A3) both attenuators are in.

The spectral resolution of RHESSI depends on the energy range, being better for small energies. In Table **3-1** can be found the spectral resolution of each detector during flight conditions, separating their front and rear segments. In particular, the average spectral resolution for the front segments is 1 keV in the energy range from 3 to 100 keV. Likewise, for the rear segments it is nearly 3 keV up to 1 MeV (Smith et al., 2002, [105]). The former value is of our interest as we will not work with energies higher than 100 keV (See section 3.3). The only detector that does not work in flight as expected was detector 2. It suffered a breakdown that let it as a monolithic detector of low resolution, and with a reduced dynamical range. Therefore, this detector should not be used for spectroscopy (Smith et al., 2002, [105]). Finally, the attenuation state of the instrument modifies its dynamical range. Without attenuation (A0) the low-energy cutoff is 3 keV. For A1 and A3, it shifts to 6 and 10 keV, respectively. The A2 state is not used in flight.

Detector	Front FWHM	Rear FWHM
1	1.13	2.90
2	7.94	—
3	0.98	2.77
4	0.98	2.82
5	1.47	2.73
6	1.01	3.05
7	3.15	2.98
8	1.26	3.36
9	1.19	2.27

Table 3-1.: Spectral resolution for the nine detectors of RHESSI at 93 keV for the front segments and at 1117 keV for the rear segments. The FWHM of both segments, front and rear, is expressed in keV. In general, the smaller the energy, the better is the spectral resolution. This table was extracted from Smith et al. (2002, [105]).

3.2. Nobeyama Radio Polarimeters

The *Nobeyama Radio Polarimeters* (NoRP) are a set of eight antennas that observe the Sun at seven different frequencies, namely, 1, 2, 3.75, 9.4, 17, 35 and 80 GHz. These instruments are hosted at the Nobeyama Radio Observatory (NRO), which is located at the Nagano Prefecture in Japan. The original antennas of the NRO are the three of the higher frequencies, i.e. 17, 35 and 80 GHz. The other four antennas were first installed at the Toyokawa Observatory in 1979 (Torii et. al, 1979, [112]), and then were moved to the NRO in 1994.

The instrumental array for the highest frequency is the only one that is not composed by a single plate. Instead, it is a two element array made with antennas of 25 cm of diameter, installed on a single equatorial mount (See Figure **3-2**). The separation distance of the array is 330 wavelengths of the observed frequency, or what is the same, 123.75 cm. The election of this particular separation distance ensures that the radio emission of the quiet Sun is canceled, thus allowing the detection of sudden and faint signals that does not belong to the microwave solar continuum (Nakajima et al., 1985, [90]). The minimum flux density detected by this pair of antennas is of the order of 10 sfu [1]. The beam width of each antenna is 65', then they cover the whole Sun as its apparent size is roughly 30'. This instrument have been working since 1984.

At 35 GHz the quiet Sun component is highly influenced by the fluctuations of the Earth's atmosphere. The observed variations in the signals are of the order of 10 %, inhibiting the detection of faint and fast bursts as those characteristics in solar flares at this frequency (Nakajima et al., 1985, [90]). Therefore, the 35 GHz antenna was designed to reduce these atmospheric fluctuations. The method employed makes the antenna temperature of the quiet Sun be equal to the cloud temperature. This condition constrained the diameter of the antenna to 30 cm, and allow it to measure small signals, also of the order of 10 sfu (Nakajima et al., 1985, [90]). The 35 GHz antenna was installed between the two elements of the 80 GHz array, at the same equatorial mount (See Figure **3-2**) and started to operate in 1983. By its part, the 17 GHz antenna has a diameter of 85 cm and was installed on a different equatorial mount in 1978. Its beam width is 100' and its bandwidth is 20 MHz (Nakajima et al., 1985, [90]). Both, the 17 and 35 GHz antennas receive the right and left circularly polarized light (See appendix A.2.5), while the 80 GHz array only measures intensity because it is a radiometer.

The specifications for the low-frequency radio polarimeters, i.e. those at 1, 2, 3.75 and 9.4 GHz, are found in Torii et al., (1979, [112]). There, the authors describe that each antenna was installed on an equatorial mount of 8 meters of height. The antennas have two independent motions, along the declination axis at a discrete rate of 0.05 degrees, and along the polar axis following the daily solar motion. Thus, the tracking of the Sun is made automatically during the whole day, from the sunrise until the sunset. A periodical correction in the antenna pointing is done

[1] Solar flux units (sfu), 1 sfu $= 10^{-22}$ W m^{-2} Hz^{-1}.

every three hours, ensuring an almost constant gain in all the antennas. The maximum gain error is estimated to be 1.5 %. At night, the position of the antennas is reversed and the cycle is repeated. Another important feature of these instruments is the regulation of the temperature in the receivers. This temperature ranging between 35 and 40 Celsius degrees. In consequence the receiver gain is quite stable, allowing daily variations of only 1 % (Torii et al., 1979, [112]).

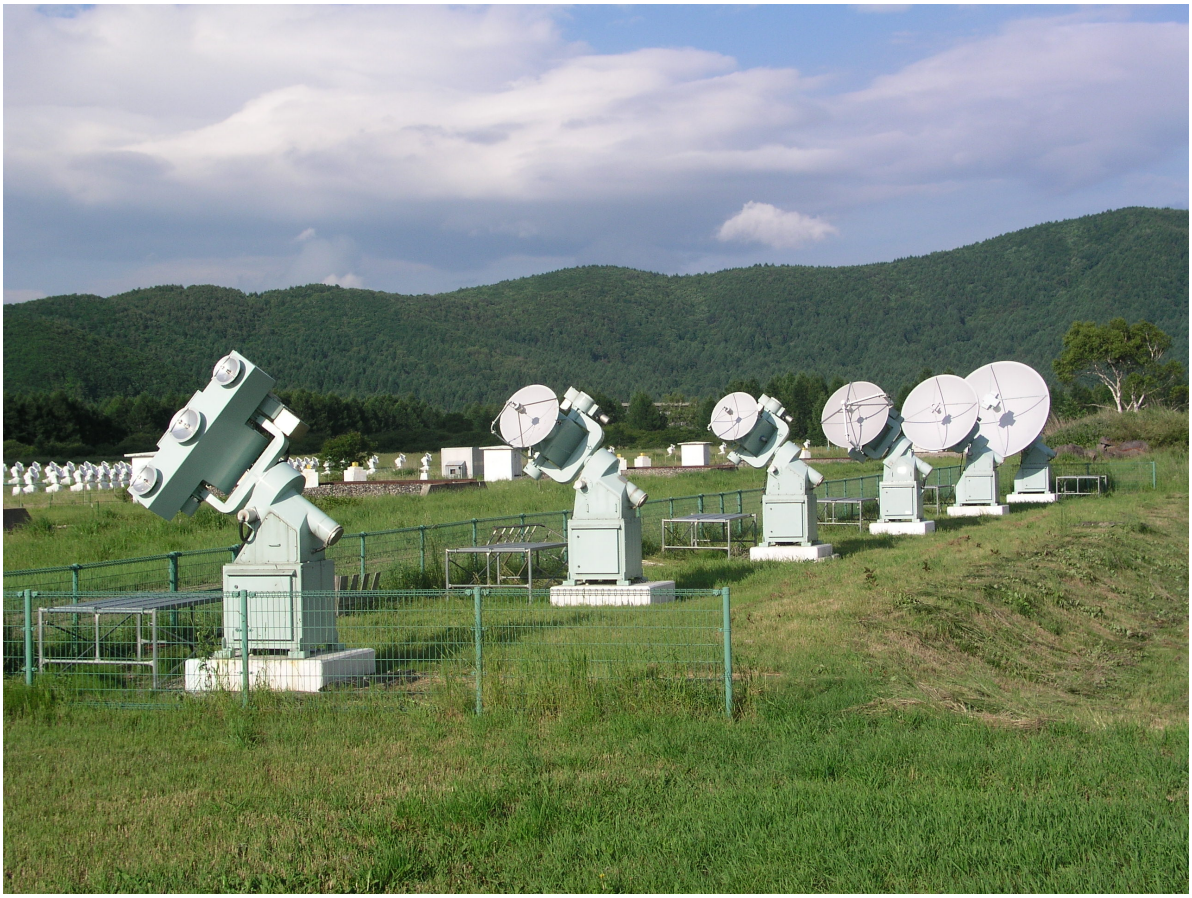

Figure 3-2.: Configuration of the Nobeyama Radio Polarimeters at the NRO [2]. The furthest plate corresponds to the detector at 1GHz. The smallest the plate diameter, the highest is the frequency observed. The nearest mount has three plates. Those of the edges registers solar signals at 80GHz, while the one at the center measures at 35 GHz.

All the antennas at the seven observing frequencies of NoRP have a temporal resolution of a tenth of second, and measure right and left circularly polarized light, except the one at 80 GHz. Therefore, they are capable to obtain the Stokes parameters I and V (See appendix A.2.5). The characteristic properties of all the antennas are shown in Table **3-2**. In general, they have a small bandwidth and present low noise. Also, the antennas observe the Sun as a star because their beam widths are always greater than the apparent size of the Sun.

[2]This image was taken from `http://www.nro.nao.ac.jp/en/gallery/images/rp_002.jpg`.

Feature	1GHz	2GHz	3.75GHz	9.4GHz	17GHz	35GHz	80GHz
Diameter (m)	3.0	2.0	1.5	0.85	0.85	0.30	0.25
Beam width (^{o})	7.4	5.6	3.8	2.6	1.66	–	1.08
Band width (MHz)	10	10	10	10	20	1000	400*
Noise (dB/sfu)	6	7	6.5	5.5	10	10	15

Table 3-2.: The main properties of the NoRP antennas are summarized. The fields of this table are taken from Torii et al. (1979, [112]) and Nakajima et al. (1985, [90]). The beam width is measured in degrees, and this is not found for the 35 GHz antenna in the literature already mentioned. The bandwidth shown for 80 GHz corresponds to the bandwidth of the first intermediate frequency (IF). The last row indicates the noise figure measured in decibels (dB) for the low-frequency antennas (1, 2, 3.75 and 9.4 GHz), while for the high-frequency antennas (17, 35 and 80 GHz) this row represents the receiver noise reported in solar flux units (sfu).

3.3. Work Sample

As was mentioned in section 1.2, we have already made an initial approach to analyze the impulsivity as a quantitative feature of solar flares. To do this, it was used a work sample composed by 48 events. In this previous study (Fajardo et al., 2016, [39]), there were obtained two main results: an alternative classification system for solar flares according to the impulsivity, and a correlation between the impulsivity types and the symmetry of the nonthermal X-ray lightcurves. Therefore, one of the objectives of this thesis is to verify or deny the aforementioned results by using a bigger work sample (See section 1.3). In particular, our interest is to analyze all the possible events that have occurred during a whole cycle of solar activity. However, there are a number of observational constraints and own considerations that limits the size of the sample. Let us explain these criteria in detail.

First of all, we will use RHESSI and NoRP data in order to study the HXR and microwave radiation generated during the impulsive phase of solar flares, according to the trapping-plus-precipitation model (See section 2.3). Then, all the flares composing the work sample must have simultaneous data on both instruments. The search of events was constrained to a specific time interval, whose extremes are given by the date of the first flare detected by RHESSI (February 12, 2002) and the New Year's eve of 2013. This temporal range spans from the maximum of the Solar Cycle 23 to the maximum of the Solar Cycle 24. Thus, a full cycle of solar activity is covered. The number of flares occurred inside this time interval, according to GOES, is 19212.

Only a fraction of all the previous flares were detected by NoRP, because it is a ground-based instrument, and hence it only observes the Sun during the daylight in Japan. Taking into account the variations of the day length due to seasons, the time interval in UTC at which NoRP is always observing the Sun goes from 22:00 to 08:00 UTC. Filtering the initial number of flares by such criterion, the sample reduces to 7689 events.

Besides, the majority of the remaining flares are GOES C-class, as they have a high probability of occurring (Veronig et al., 2002, [116]). These kind of flares usually do not produce enough counts on RHESSI detectors, making their nonthermal HXR lightcurves pretty noisy. In consequence, HXR bursts due to direct precipitation are hardly to detect in such low class events. For this reason, we neglect them. Taking into account this cut-off over GOES classes, the updated size of the sample is 437. This value corresponds to all flares having a GOES class greater or equal than M1.0, and that were observed by NoRP.

In addition, we checked the availability of RHESSI data. Despite being in the space, this instrument have several data gaps due to eclipses with Earth and passes through the SAA (See section 3.1). There is a procedure that check the operational stage of RHESSI for a given time interval, which is called `hsi_nosaan.pro` (L. Glesener, 2014, private communication). As output it gives the fraction of the time interval at which the instrument is acquiring data normally, i.e. the data acquisition does not have activated either the eclipse flag nor the SAA flag.

The `hsi_nosaan` procedure was run for all the 437 events, using as time interval the temporal range spanning from the beginning time to the peak time of each flare according to GOES (See section 1.1). The choice of this particular temporal range is justified by the Neupert effect, according to which it is expected that the HXR to be emitted at the rising part of the SXR lightcurve (See section 1.2). If the output of the procedure is 0.9 or greater, i.e. if the time interval was observed a 90 % or more, the corresponding flare is kept in the sample, otherwise it is rejected. Just 228 flares fulfill this condition.

Lastly, during the X-ray spectral analysis 20 events presented problems. In particular, their spectra were very noisy, having no clear thermal and nonthermal components. This issue makes difficult either to achieve a good spectral fitting nor to compute the transition energy (See subsection 4.1.1). Therefore, these flares were not taken into account.

Thus, putting all the previous criteria together the final work sample was composed by 208 flares. All of them took place from February 12, 2002 to December 31, 2013, and were observed simultaneously by NoRP and RHESSI. Also, they have a GOES class greater or equal to M1.0. All the events of the work sample are listed in Table **3-3**, with their respective ID catalog, peak time in UT according to GOES, and GOES class.

ID	Peak time (UT)	Class	ID	Peak time (UT)	Class	ID	Peak time (UT)	Class
001	2002-02-25 02:57	M1.0	036	2002-10-20 03:39	M1.5	071	2003-10-24 02:54	M7.6
002	2002-03-14 01:50	M5.7	037	2002-10-20 05:14	M1.2	072	2003-10-25 04:46	M1.2
003	2002-03-30 22:26	M1.0	038	2002-11-10 03:21	M2.4	073	2003-10-25 05:53	M1.7
004	2002-04-14 03:51	M1.4	039	2002-11-18 02:08	M7.4	074	2003-11-01 22:38	M3.2
005	2002-04-15 03:55	M1.2	040	2002-12-04 22:49	M2.5	075	2003-11-13 05:01	M1.6
006	2002-05-31 00:16	M2.4	041	2002-12-16 23:36	M1.3	076	2003-11-17 01:34	M1.2
007	2002-06-01 03:57	M1.5	042	2003-01-07 23:33	M4.9	077	2003-11-18 01:39	M1.8
008	2002-06-23 02:55	M1.6	043	2003-01-09 05:37	M1.0	078	2003-11-19 04:01	M1.7
009	2002-07-03 02:13	X1.5	044	2003-01-23 04:48	M1.0	079	2003-11-20 02:12	M1.4
010	2002-07-06 03:42	M1.8	045	2003-01-24 03:27	M1.9	080	2003-11-20 23:53	M5.8
011	2002-07-08 23:20	M2.3	046	2003-02-06 03:49	M1.2	081	2003-12-02 23:00	M1.5
012	2002-07-13 00:08	M1.1	047	2003-03-18 06:00	M2.5	082	2004-01-06 06:29	M5.8
013	2002-07-18 03:37	M2.2	048	2003-03-19 03:07	M1.5	083	2004-01-09 01:22	M1.1
014	2002-07-23 00:35	X4.8	049	2003-04-09 23:29	M2.5	084	2004-01-09 01:44	M3.2
015	2002-07-26 22:17	M5.3	050	2003-04-26 03:06	M2.1	085	2004-01-18 00:17	M1.4
016	2002-07-29 02:38	M4.8	051	2003-04-26 23:40	M2.5	086	2004-01-20 07:43	M6.1
017	2002-07-31 01:53	M1.2	052	2003-04-29 04:59	M1.1	087	2004-02-26 02:03	X1.1
018	2002-08-16 22:12	M1.2	053	2003-05-02 03:08	M1.0	088	2004-03-18 05:17	M1.6
019	2002-08-16 23:33	M1.7	054	2003-05-26 05:50	M1.9	089	2004-03-24 23:29	M1.5
020	2002-08-17 01:08	M1.1	055	2003-05-27 03:06	M1.4	090	2004-04-05 05:55	M1.7
021	2002-08-20 01:40	M5.0	056	2003-05-29 01:05	X1.2	091	2004-05-21 23:52	M2.6
022	2002-08-20 02:57	M1.4	057	2003-06-01 03:06	M1.4	092	2004-07-13 00:17	M6.7
023	2002-08-21 01:41	M1.4	058	2003-06-06 23:38	M1.0	093	2004-07-14 05:23	M6.2
024	2002-08-22 01:57	M5.4	059	2003-06-09 22:31	M1.4	094	2004-07-15 01:41	X1.8
025	2002-08-24 05:48	M1.8	060	2003-06-10 02:54	M2.0	095	2004-07-16 02:06	X1.3
026	2002-08-26 01:03	M1.8	061	2003-06-10 22:13	M1.0	096	2004-07-17 23:08	M1.1
027	2002-08-29 02:53	M1.6	062	2003-06-11 03:06	M1.8	097	2004-07-18 00:35	M2.0
028	2002-09-08 01:43	M1.5	063	2003-06-13 02:04	M3.1	098	2004-07-22 00:32	M9.1
029	2002-09-29 06:39	M2.6	064	2003-06-13 04:37	M1.7	099	2004-07-22 22:58	M1.6
030	2002-09-30 01:50	M2.1	065	2003-06-13 06:45	M1.8	100	2004-07-25 06:39	M1.0
031	2002-10-03 02:21	M2.1	066	2003-06-17 22:55	M6.8	101	2004-08-14 05:44	M7.4
032	2002-10-04 00:43	M1.0	067	2003-07-02 07:28	M3.0	102	2004-08-15 05:06	M1.2
033	2002-10-04 05:38	M4.0	068	2003-07-29 01:39	M1.3	103	2004-08-16 03:47	M1.1
034	2002-10-14 00:10	M2.2	069	2003-10-19 06:26	M1.9	104	2004-08-16 22:44	M1.1
035	2002-10-20 00:45	M1.8	070	2003-10-23 02:41	M2.4	105	2004-08-17 05:06	M1.1

Table 3-3.: List of the events that compose the work sample. Part I.

ID	Peak time (UT)	Class	ID	Peak time (UT)	Class	ID	Peak time (UT)	Class
106	2004-08-19 07:01	M3.0	141	2005-09-13 23:22	X1.7	176	2012-07-02 00:35	M1.1
107	2004-08-31 05:38	M1.4	142	2005-09-17 06:05	M9.8	177	2012-07-04 23:55	M1.2
108	2004-09-12 00:56	M4.8	143	2005-11-18 00:34	M1.2	178	2012-07-05 03:36	M4.7
109	2004-10-30 03:33	M3.3	144	2005-12-02 02:52	M6.5	179	2012-07-05 06:58	M1.1
110	2004-10-31 02:26	M1.1	145	2006-04-06 05:33	M1.4	180	2012-07-06 01:40	M2.9
111	2004-10-31 05:32	M2.3	146	2007-06-02 06:11	M2.5	181	2012-07-07 03:15	M1.2
112	2004-11-03 03:35	M1.6	147	2010-02-08 07:43	M4.0	182	2012-07-10 06:27	M2.1
113	2004-11-04 23:09	M5.4	148	2010-06-12 00:57	M2.0	183	2012-08-06 04:38	M1.6
114	2004-11-06 00:34	M9.3	149	2010-06-13 05:39	M1.0	184	2012-08-18 03:23	M1.9
115	2004-11-06 00:57	M5.9	150	2011-01-28 01:03	M1.3	185	2012-08-18 22:54	M1.0
116	2004-11-06 01:57	M3.6	151	2011-02-15 01:56	X2.2	186	2012-09-06 04:13	M1.6
117	2004-11-10 02:13	X2.5	152	2011-02-16 01:39	M1.0	187	2012-09-30 04:33	M1.3
118	2004-12-01 07:20	M1.1	153	2011-02-24 07:35	M3.5	188	2012-11-21 06:56	M1.4
119	2005-01-15 00:43	X1.2	154	2011-03-08 02:29	M1.3	189	2013-01-13 00:50	M1.0
120	2005-01-15 23:02	X2.6	155	2011-03-08 03:58	M1.5	190	2013-05-02 05:10	M1.1
121	2005-01-17 03:21	M2.6	156	2011-03-09 23:23	X1.5	191	2013-05-12 22:44	M1.2
122	2005-01-19 07:31	M6.7	157	2011-03-10 22:41	M1.1	192	2013-05-13 02:17	X1.7
123	2005-01-20 07:01	X7.1	158	2011-03-15 00:22	M1.0	193	2013-05-15 01:48	X1.2
124	2005-05-12 07:33	M1.6	159	2011-04-22 04:57	M1.8	194	2013-07-03 07:08	M1.5
125	2005-05-16 02:43	M1.4	160	2011-06-07 06:41	M2.5	195	2013-10-15 23:36	M1.3
126	2005-05-17 02:39	M1.8	161	2011-07-30 02:09	M9.3	196	2013-10-22 00:22	M1.0
127	2005-06-01 02:43	M1.7	162	2011-08-03 03:37	M1.1	197	2013-10-23 23:43	M1.4
128	2005-06-03 04:11	M1.3	163	2011-08-03 04:32	M1.7	198	2013-10-24 00:08	M3.1
129	2005-07-12 22:52	M1.3	164	2011-09-05 04:28	M1.6	199	2013-10-25 03:02	M2.9
130	2005-07-14 03:23	M1.0	165	2011-09-06 22:20	X2.1	200	2013-10-26 06:06	M2.3
131	2005-07-14 22:57	M1.1	166	2011-09-09 06:11	M2.7	201	2013-11-02 22:21	M1.6
132	2005-07-16 03:38	M1.0	167	2011-09-10 07:40	M1.1	202	2013-11-07 03:40	M2.3
133	2005-07-28 00:30	M1.0	168	2011-09-23 23:56	M1.9	203	2013-11-10 05:14	X1.1
134	2005-08-03 05:06	M3.4	169	2011-09-25 04:50	M7.4	204	2013-11-15 02:29	M1.0
135	2005-08-25 04:40	M6.4	170	2011-09-26 05:08	M4.0	205	2013-11-17 05:10	M1.0
136	2005-09-09 02:36	M1.1	171	2011-10-20 03:25	M1.6	206	2013-11-23 02:32	M1.1
137	2005-09-09 03:00	X1.1	172	2011-11-05 03:35	M3.7	207	2013-12-19 23:19	M3.5
138	2005-09-09 05:48	M6.2	173	2012-05-05 23:01	M1.3	208	2013-12-23 00:03	M1.3
139	2005-09-10 06:14	M3.7	174	2012-05-06 01:18	M1.1			
140	2005-09-11 02:35	M3.4	175	2012-05-10 04:18	M5.7			

Table 3-3.: List of the events that compose the work sample. Part II.

4. Data Analysis

In this Chapter, analysis methods used to deduce the impulsivity and the relevance of magnetic trapping in all the events of our work sample are described. In order to give a clear and organized description, first the HXR analysis is explained in section 4.1, followed by its microwave radiation counterpart in section 4.2. The event (SOL2002-08-22T01:57-M5.4) will be used to illustrate the analysis procedures. These procedures were applied in the same manner to rest of the sample.

4.1. HXR Analysis

The precipitation of electrons towards the denser layers of the solar atmosphere generates HXR emissions of energies up to hundreds of keV, if only electron-ion collisions are considered (See section 2.1). Such emissions were used to estimate the impulsivity of solar flares (See section 1.2). Therefore, the impulsivity is directly related to the precipitation of electrons, and both can be studied by analyzing the temporal behavior of the HXR lightcurves.

The HXR data used for the present analysis was obtained by RHESSI. This space solar observatory was selected due to three reasons. First, the instrument was active throughout the whole time interval spanned by the work sample (See section 3.3). Second, the HXR coming from the precipitation of electrons can be observed by RHESSI, beacuse its spectral range goes from 3 keV to 17 MeV (See section 3.1). Third, RHESSI posses a high temporal and spectral resolution, the latter being 1 keV within the energy range of interest, i.e. up to 100 keV (See section 3.1).

The HXR analysis described here is divided into various steps. Initially, the X-ray spectra is generated and their thermal and nonthermal components are calculated. Then, the nonthermal emission is used to reconstruct the HXR lightcurve of the flare, from which the impulsivity parameter and the degree of symmetry are estimated. Further characteristics of the flares like the number total number of peaks of the HXR emission or *multiplicity*, the evolution of the spectral index, and the correlation with the Neupert effect, are then evaluated. The last two of these features turned out to be important in the first stages of the impulsivity concept (See section 1.2).

4.1.1. RHESSI Spectra and Nonthermal X-ray Lightcurves

Most of the methods explained in this subsection and the next one are taken from the analysis section of Fajardo et al. (2016, [39]). First of all, the X-ray spectra of the example flare were generated within the *analysis time interval*, which spans from 10 minutes before the beginning of the flare to half an hour after its end. According to GOES the event (SOL2002-08-22T01:57-M5.4) started at 01:37 and ended 02:35 UT. This time interval was divided into regular bins of 8 s. Enough counts can be obtained by using this time bin width, because it represents approximately two full RHESSI rotations, and the appropriate reconstruction of images and spectra for major flares needs just half RHESSI rotation (Lin et al., 2002, [80]; See section 3.1). In each temporal bin of 8 seconds, the X-ray spectrum from 3 to 100 keV was reconstructed in photon flux units. Only the front segment of detector 1 was used for this reconstruction, beacuse this detector has a good spectral resolution and optimal performance during the whole time interval covered by the work sample (L. Glesener, 2014, private communication). In total, 93 energy bins covering the energy interval aforementioned were used. The spectral width of such bins were chosen according to the energy band. The photon flux emitted decreases with increasing energy, then the corresponding energy bins at high energies should be broader than those for low energies. The spectral widths selected were 0.3, 0.5, 1, 2, and 5 keV, for the energy bands 3−15, 15−25, 25−40, 40−60, 60−100 keV, respectively.

The resulting spectra not only contains information of the X-ray emission produced by the flare, but also of the instantaneous solar and instrumental background. Before continuing with the analysis, such background must be found and extracted from the spectra, to preserve only the contribution associated with the flare. This procedure requires the selection of a time interval when we ensure most of the emission is due to this background. The ideal choice for this time interval are the eclipses of the instrument, or its passes through the SAA. This was the case of our example flare. An eclipse, or RHESSI night, took place starting at 02:22:40 UT and lasted until the end of the analysis time interval. The background was computed as the mean photon flux measured during the eclipse, in each one of the 93 energy bins used to reconstruct the spectra. Then, the background over a given energy range is just the average of the individual background flux of the energy bins composing the energy range. Thus, the background can be represented both at the X-ray lightcurve or as a X-ray spectrum as is shown in Figure **4-1**.

However, for some flares in the work sample RHESSI nights or SAA transits do not occur during their analysis time intervals. Hence, in those cases there were chosen five different *background time intervals*, one for each of the following energy ranges: 3−6, 6−12, 12−25, 25−50, and 50−100 keV. These time intervals consist of temporal ranges of one minute centered on the minimum flux of its respective energy band. Again, the background was calculated as the mean photon flux registered at the background time intervals, for all the 93 energy bins. Lastly, the background was substracted to the flux of the raw data to obtain only the contribution related to the flare.

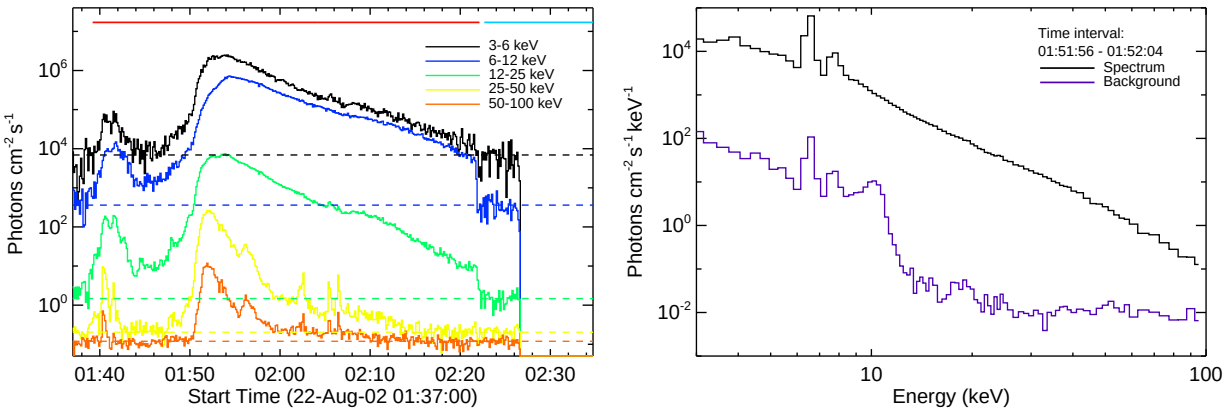

Figure 4-1.: *Left panel:* photon flux of the five minor RHESSI channels and their corresponding background levels represented by the horizontal dashed lines. These background levels correspond to the mean photon flux registered during the RHESSI night, which is labeled by the upper horizontal cyan bar. By its part, the upper horizontal red bar points out the detection of the flare. *Right panel:* the same background presented as a X-ray spectrum for a given time interval. Due to the background levels were taken as constants along time, this background spectrum is the same throughout the analysis time interval.

Then, the thermal and nonthermal X-ray emissions of the example flare were characterized in a similar manner as was done by Grigis & Benz (2004, [51]). In general, the thermal component is present at all flare stages and it is dominant at low energies ($E < 30$ keV), while the nonthermal component has a transient behavior and appears mostly during the impulsive phase. In order to identify these two contributions a spectral fitting process was carried out using the Object SPectral EXecutive Package (`OSPEX`) (Schwartz et al., 2002, [99]). This spectral analysis was not done over all the analysis time interval, due to transient nature of the nonthermal emission. Instead, it was performed within a short time interval where we ensure both contributions were present. This interval, hereafter called *spectral time interval*, lasts three minutes and is centered on the most prominent peak observed at the energy band 25−100 keV. Thus, the spectral time interval was composed by 22 of the initial temporal bins of 8 seconds, and hence it contains the same number of X-ray spectra.

The spectral fitting process was performed over the 22 temporal bins aforementioned. The corresponding X-ray spectra were fitted using two theoretical functions available in `OSPEX`. The first of them, called `vth`, reproduces the thermal continuum due to a single dominant temperature, plus the flux coming from the iron emission line centered at 6.7 keV. The other function, labeled as `bpow`, is a broken power law with two different spectral indices, and it replicates the nonthermal X-ray emission. Explicitly, the parameters to fit in `vth` are: the emission measure,

the plasma temperature, and the relative abundance of iron with respect to other metals. By its part, the parameters associated to `bpow` are: the flux value at the low cut-off energy, the break energy, and the spectral indexes before and after the break energy.

In the fitting process, we always chose the same theoretical functions, `vth` and `bpow`, and also all the parameters were allowed to vary, except by the spectral index before the break energy which was fixed to 1.5, in order to limit the relevance of `bpow` at the low-energy part of the spectra. The energy interval to fit varied in each temporal bin according to the respective attenuation state of RHESSI. The energy intervals used were 3-100 keV, 6-100 keV, and 10-100 keV for the attenuation states A0, A1, and A3, respectively (See section 3.1). The previous considerations were always used regardless the event to study. Figure **4-2** shows the X-ray spectrum and the theoretical functions fitted for one temporal bin of our example flare.

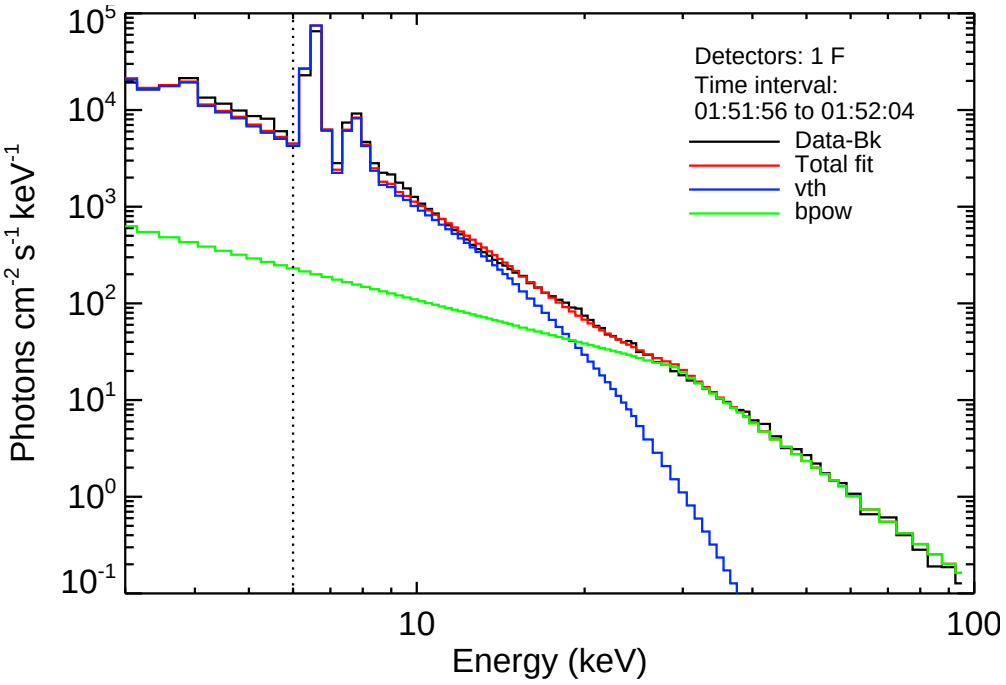

Figure 4-2.: Reconstructed spectrum for a given time interval around the maximum nonthermal emission of the example flare. The theoretical fitting functions `vth` and `bpow`, are shown in blue and green, representing the thermal and nonthermal components of the spectrum, respectively. The spectrum was fitted above 6 keV (vertical dotted black line) since the instrument attenuator state was A1.

Then, our interest was to estimate the energy that separates the thermal and nonthermal parts of the spectrum for each temporal bin. Hereafter, we will denote it as *transition energy*. We defined this quantity as the energy at which the nonthermal component is 10 times higher (in units of photon flux per unit energy) than the thermal one. In other words, it marks the beginning of the nonthermal regime in the spectra. As the X-ray emission from the flare evolves in time,

the transition energy changes from one temporal bin to another. However, these variations are small and are confined in a narrow energy band. Then, we took the transition energy for each flare as the average of the corresponding results for the 22 temporal bins. In our example case (SOL2002-08-22T01:57-M5.4) the transition energy was 18.5 ± 0.2 keV.

The next step was the creation of the nonthermal X-ray lightcurve of the example flare. To do this, the reconstructed X-ray spectra for all of the initial temporal bins of 8 seconds was integrated from the transition energy to 100 keV. The transition energy was selected as the lower integration limit, because emissions coming from energies above this limit are dominated by the nonthermal component. Thus, the thermal contributions are avoided. Furthermore, 100 keV was chosen as the upper integration limit because most of the flares have extremely low photon fluxes at higher energies. The results of the integrations composed the nonthermal X-ray lightcurve in units of photon flux.

The previous description demonstrates one particular approach to produce the nonthermal X-ray lightcurve of a solar flare. However, this is not the only way to do it. One can generate lightcurves by integrating the X-ray spectra in fixed energy intervals, where it is assumed that the emission is exclusively nonthermal (H. Hudson, 2015, private communication). This method is faster than the one explained before, because the spectral fitting process is skipped. Following this idea, four other nonthermal X-ray lightcurves were produced for the example flare, and also for each flare in the sample, using the next energy intervals: 30—40 keV, 25—50 keV, 50—100 keV, and 30—100 keV. Hereafter, such lightcurves will be called LC2, LC3, LC4 and LC5, respectively. Likewise, the lightcurve made by integrating the X-ray spectra from the transition energy to 100 keV will be referenced as LC1. Figure **4-3** shows the five lightcurves generated for our example flare (SOL2002-08-22T01:57-M5.4). The main emission of all these lightcurves are located between the start time and peak time of the flare according to GOES, as is expected from the Neupert effect (See section 1.2 & subsection 4.1.4).

4.1.2. Impulsivity Parameter and Degree of Symmetry

We quantified the impulsivity of a solar flare by estimating the duration of its nonthermal X-ray emission (See Section 1.2). We assume the latter as the duration of the most prominent peak in the nonthermal X-ray lightcurve. Below it is illustrated how such time interval was found in the example flare. The method used is identical for any of its five nonthermal X-ray lightcurves.

First, the most prominent peak in the lightcurve of interest was located. One to be cautious with the selection of this peak, because when the attenuation of RHESSI changes from a high state to a lower one, e.g. from A1 (weak attenuation) to A0 (no attenuation), false peaks are generated. Once the true maximum flux due to the flare was located, then there were found the times at which the flux decays to a *reference flux level*, which was chosen as the 10 % of the maximum flux,

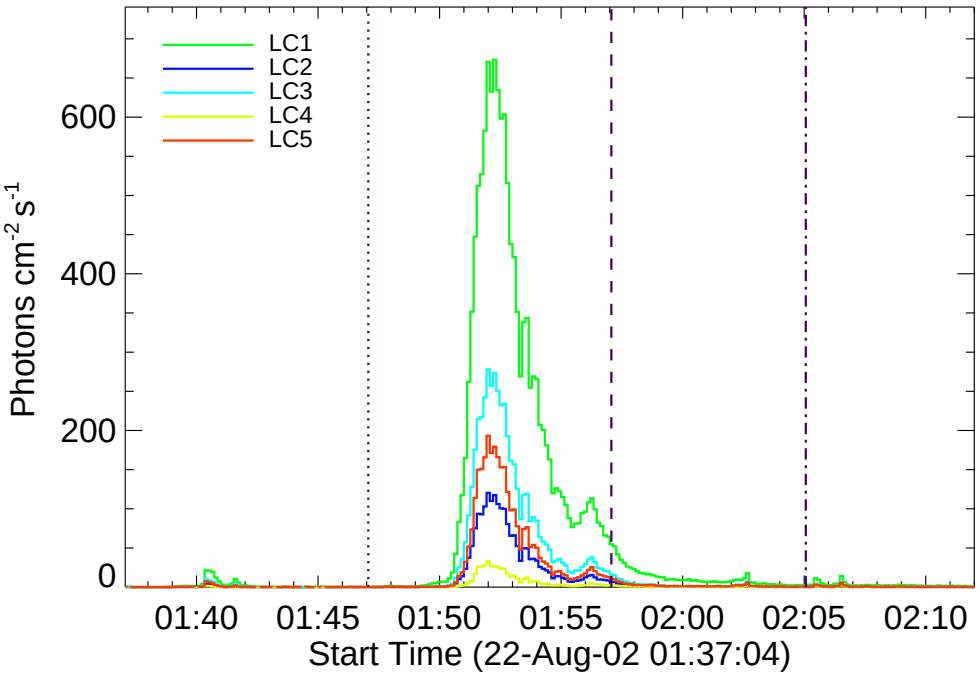

Figure 4-3.: Lightcurves LC1, LC2, LC3, LC4, and LC5 of the example flare (SOL2002-08-22T01:57-M5.4). They were obtained by integrating the X-ray spectra in five different energy intervals. The vertical dashed, dotted, and dashed-dotted lines represent the start, peak, and end times of the example flare according to GOES, respectively.

before and after the most prominent peak occurred. Such times correspond to the beginning and end times of the nonthermal X-ray emission, t_b and t_e, respectively. For some flares the photon flux never reached a value less or equal than 10 % of its maximum within its analysis time interval. In those cases a higher reference flux level was used, up to 25 % of the maximum flux. The time elapsed between t_b and t_e was considered as the duration of the nonthermal X-ray emission of the flare, or what is the same, its *impulsive phase duration* (IPD) (See section 1.2). Additionally, the IPD can be divided into two parts: its rising time (RT) and its decay time (DT). The former time interval goes from t_b to the peak time of the nonthermal emission, while the latter goes from the aforementioned peak time to t_e. Thus, IPD $=$ RT $+$ DT.

The method explained here was applied in the same manner to all the lightcurves belonging to the events of the work sample. In total, the IPD calculation was done 1020 times, because there were five lightcurves for each of the 208 events of the sample. The mean value of the 1020 IPD estimated was named the *normalization factor* (NF), and its value was 292.8 ± 0.1 s. This normalization factor was used to compute the impulsivity parameter (IP), which together with the degree of symmetry follow the next formulas

$$\mathrm{IP} = \frac{\mathrm{NF}}{\mathrm{IPD}} \qquad \mathrm{S} = \frac{\mathrm{RT} - \mathrm{DT}}{\mathrm{RT} + \mathrm{DT}} \tag{4-1}$$

All the involved terms in the previous expressions were already discussed. The values of IPD, RT, DT, IP, and S for the five nonthermal X-ray lightcurves of the example flare are summarized in Table **4-1**. The largest values of IPD, RT, and DT were obtained for LC1. This is due to its associated energy interval, 18.5—100 keV, is the broadest of all the five intervals used, and also because the low energy limit of such interval, i.e. the transition energy, is the smallest of all. Then, LC1 was reconstructed with more photons than the other lightcurves, and therefore it took longer to the flux to reach the reference flux value. Nevertheless, at all cases the values of S are similar, because the proportions between RT and DT remain the same. Also, the values of IP are always around 1.0 at all lightcurves, indicating that the example flare is probably impulsive (See sections 1.2 & 5.1).

Temporal observable	**LC1**	**LC2**	**LC3**	**LC4**	**LC5**
IPD [s]	360	224	256	200	216
RT [s]	88	64	64	48	56
DT [s]	272	160	192	152	160
IP	0.813	1.307	1.144	1.464	1.356
S	0.511	0.429	0.500	0.520	0.481

Table 4-1.: Impulsive phase durations, rise times, decay times, impulsivity parameters, and degrees of symmetry of the example flare (SOL2002-08-22T01:57-M5.4). The results are shown for its five nonthermal X-ray lightcurves (See subsection 4.1.1). The nominal error in the determination of RT, DT and IPD is the half duration of a temporal bin, i.e. 4 s. The uncertainties of IP and S were calculated according to Ardila (2007, [2]). These uncertainties are not shown in this Table, but there are always less than 15 % of their corresponding value.

4.1.3. Multiplicity

It is typical that solar flares have many peaks at HXR (Foullon et al., 2005, [46]; Ofman & Sui, 2006, [92]). This behavior have been found even in a timescale of less than a second (Aschwanden, 2004, [6]). This bursty pattern of the nonthermal X-ray lightcurves is assumed to be generated by unsteady magnetic reconnection, dominated by tearing and coalescence instabilities (Aschwanden, Sec. 10.2, [5]). The temporal resolution chosen for our data, 8 seconds, did not allow us to study these rapid variations in the flares of the work sample. Nevertheless, these fast spikes can join together forming longer envelopes that also present a bursty behavior at larger timescales. Thus, the objective of the present subsection is to check how many of these envelopes appeared in a given flare during its impulsive phase.

The search for peaks was restricted to the time interval elapsed by the impulsive phase duration. The nonthermal X-ray lightcurve within this time interval is smoothed using a window of three elements, all of them having the same weight. Thus, random minor peaks were removed from the lightcurve. Then, all the extrema, mimima and maxima, were detected together with their corresponding times. Again, all the false peaks produced by changes in the attenuation state of RHESSI were not taken into account.

For each true maximum the following criteria were evaluated: **a**) how far were their nearest local minima before and after the local maximum under study, and **b**) how prominent was its peak flux. If any of their local minima were immediately contiguous, then the peak was discarded. Additionally, if its maximum flux value was lower than certain noise level, then the peak was also discarded. Such noise level was computed as the mean flux during the impulsive phase duration. Finally, the number of maxima that satisfied the aforementioned criteria were counted, and this number corresponded to the *multiplicity* of the event under study. This treatment can be developed on any of the five nonthermal X-ray lightcurves of a given event in the work sample. For the example flare the multiplicity is 1 for all its five lightcurves, as is expected from Figure **4-3**. We took another event of the work sample having multiple peaks for showing how this bursty emission looks like, and how it was detected. This example appears in Figure **4-4**.

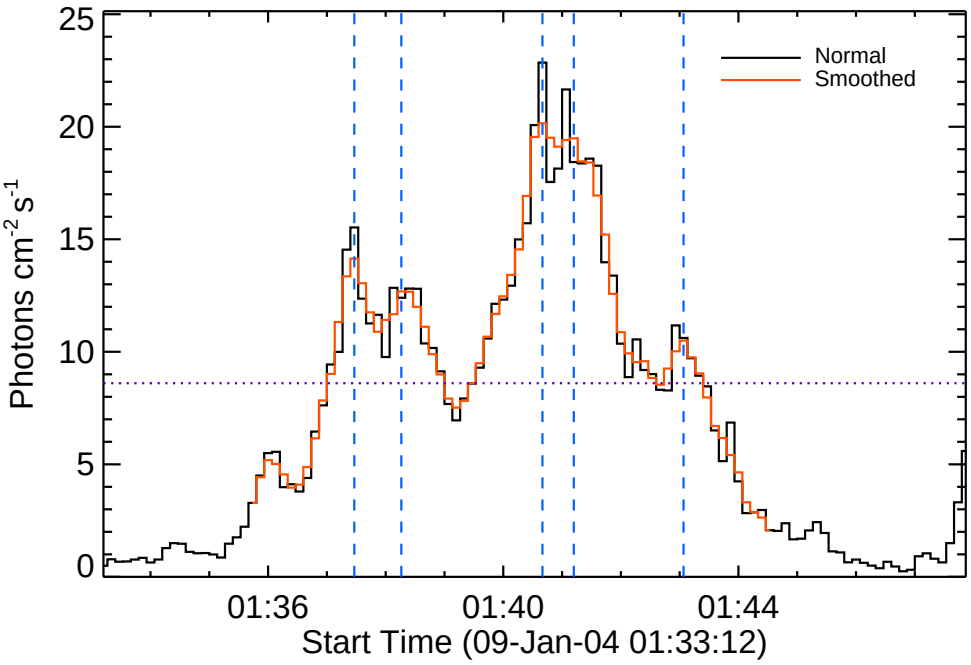

Figure 4-4.: LC1 for the flare (SOL2004-01-09T01:44-M3.2). The red curve corresponds to the smoothed flux throughout the impulsive phase duration. The horizontal dotted line indicates the level of noise. There were detected five maxima above such noise, whose peak times are marked by the blue dashed vertical lines. Thus, the multiplicity of this event at LC1 is 5.

4.1.4. Evolution of the Spectral Index

In subsection 4.1.1 it was seen that the X-ray spectrum of a solar flare has two components, the thermal and the nonthermal. The nonthermal component dominates the spectrum above certain energy, that we defined as the transition energy. In general, the nonthermal component can be modeled as a power-law. Because the nonthermal emission has a transient behavior, appearing solely when the precipitation of electrons occurs, then the spectral index of its corresponding power-law changes throughout the flare. Such changes have been studied previously, identifying typical evolutionary patterns like the *soft-hard-soft* (SHS) (Grigis & Benz, 2004, [51]) and the *soft-hard-harder* (SHH) (Kiplinger, 1995, [65]). These patterns turned out to be relevant for the intuitive concept of impulsivity, with the first of them being related to impulsive flares, and the second to the gradual ones (See section 1.2). Here, we evaluate the temporal evolution of the spectral index in order to recognize all its possible evolutionary patterns, and relate them to the different kinds of impulsivity. The latter will be described in section 5.1.

In the spectral fitting process the theoretical function responsible to reproduce the nonthermal emission is a broken power-law, which is known in `OSPEX` as `bpow` (See subsection 4.1.1). In most of the flares analyzed the break energy of this broken power-law was found around 20—40 keV. From the two spectral indexes of `bpow`, the index of interest is the one after the break energy, hereafter called φ, and it describes the high energy part of the X-ray spectrum. Additionally, the other index was always fixed to a value of 1.5, and then it had not evolution at all.

The study of the temporal evolution of φ was performed uniquely over the spectral time interval, which is the temporal range where the spectral fitting process was carried out, and also when the most prominent nonthermal emission took place (See subsection 4.1.1). The spectral time interval consisted of 22 temporal bins of 8 seconds for any event of the work sample. Thus, a given event like the example flare counted with 22 values of φ. These values were plotted against time as can be seen in Figure **4-5**. In this plot the vertical axis shows the values of φ as negatives. This is done on purpose, because the smaller is φ the harder is its corresponding spectrum. So, hard spectral indexes are located in upper part of the plot, while softer ones appeared in the lower part. Additionally, the evolutionary patterns of φ were not examined in flares that had changes in the attenuation states of RHESSI during the spectral time interval. This criterion was taken into account because the attenuation changes generate abrupt variations in the resulting fitted parameters, including φ, and therefore do not allow an adequate determination of the temporal evolution of φ. In the case of the example flare, RHESSI always had the thin attenuator in (A1 state) during the entire spectral time interval as appears in Figure **4-5**.

The spectral index evolution was evaluated by comparing two fits applied to the function of φ along time. One of them was a linear fit covering all the 22 temporal bins. The other one was a double linear fit, i.e. the composition of a linear fit for the first half of the spectral time interval

(first 11 temporal bins), and another linear fit for the second half of the spectral time interval (last 11 temporal bins). The correlation coefficient (r^2) of both fits, single linear and double linear, were calculated. The fit with the greater correlation coefficient was used to describe the temporal evolution of φ, as long as it was greater than 0.5 in order to ensure that the chosen fit was appropriate for the spectral index data. Of course, other kind of fits e.g polynomials of higher order, can be used. Nevertheless, it is hard to get a physical concept of them.

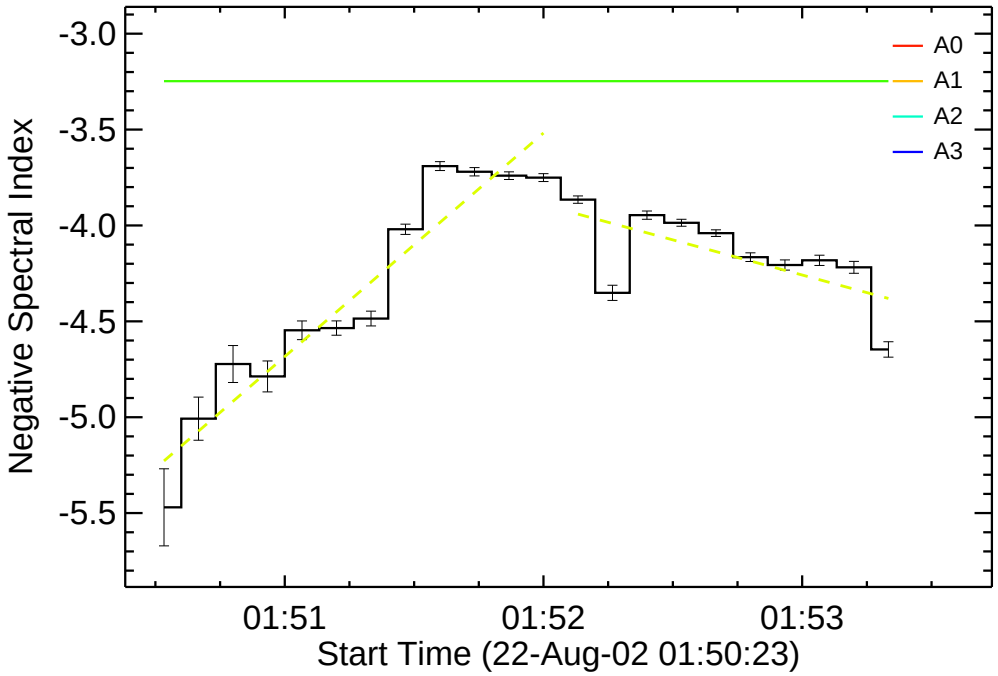

Figure 4-5.: Evolution of the spectral index for the example flare (SOL2002-08-22T01:57-M5.4) throughout its analysis time interval. For this event the best match was achieved with the double linear fit, which is represented by the dashed yellow straight segments. The slopes of the double linear fit varied from positive to negative, therefore the event follows a SHS evolutionary pattern.

If the single linear fit matched better the spectral index data, then there were three possibilities for its temporal evolution: a monotonically decreasing function, a flat function, or a monotonically increasing function. The discriminating factor between these functions was the *critical slope*. If the absolute value of the slope of the linear fit was less than the critical slope, then the evolution is said to be flat. Otherwise, it was a monotonous function, which was increasing or decreasing depending on the sign of the slope. The value of the critical slope was chosen *ad hoc* as 1.5/180s. This means that for a flat pattern the spectral index changed less than 1.5 powers within the spectral time interval (180s). Each of the three evolutionary patterns already exposed were named by us following the notation of the already known patterns, SHS and SHH. Thus, the monotonically decreasing function corresponded to a *harder-hard-soft* pattern (HHS), the flat function to a flat pattern (FLA), and the monotonically increasing function to a SHH pattern.

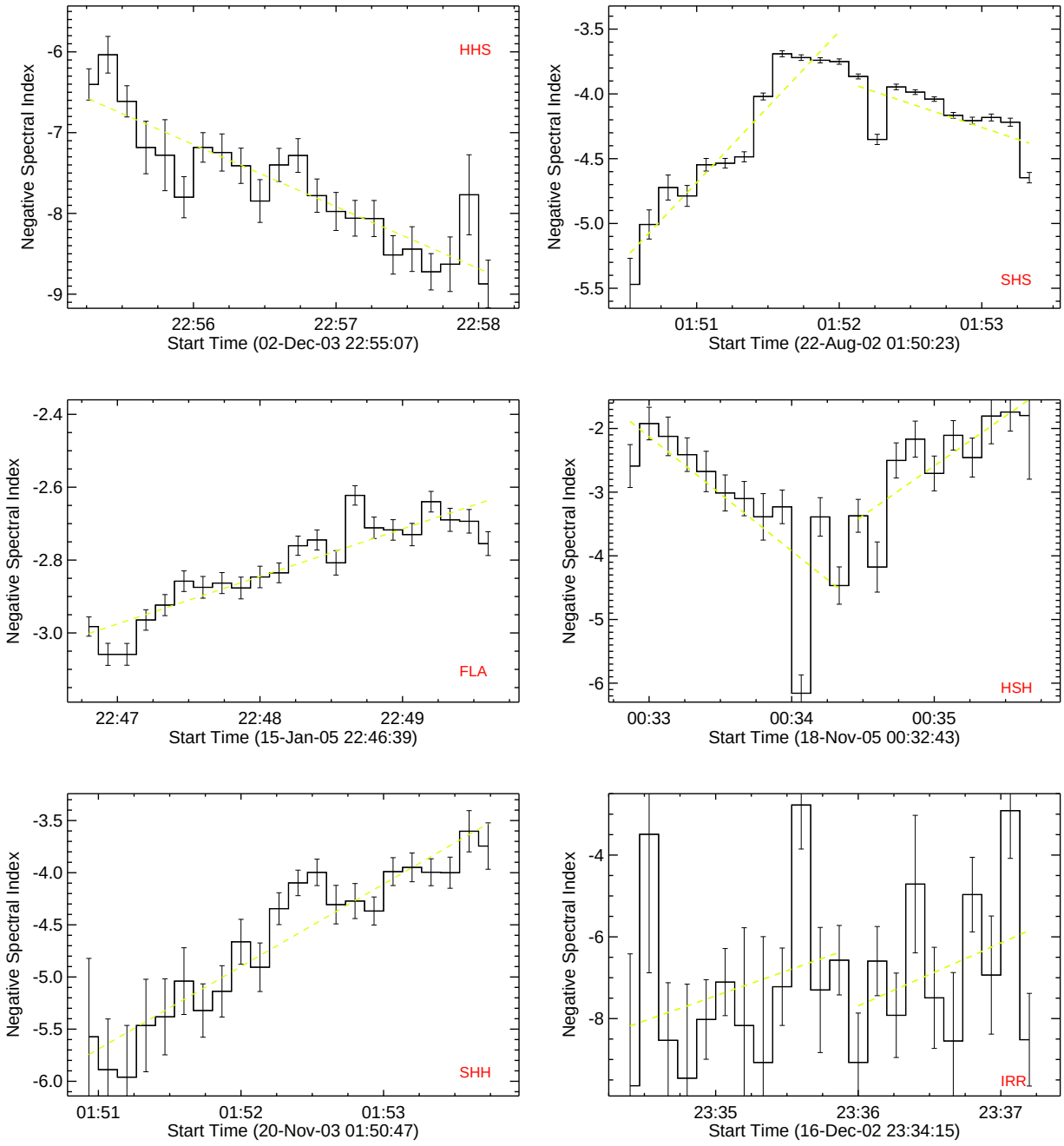

Figure 4-6.: All the temporal evolutions of the spectral index (φ) found in the work sample. In the left column appear the evolutionary patterns found with the single linear fit, while in the right column are the patterns that matched better the double linear fit. The IDs on the work sample of the events plotted (See Table **3-3**) are 81, 120, 79, 24, 143, and 41, for the patterns HHS, FLA, SHH, SHS, HSH, and IRR, respectively. The spectral index describes the behavior of the nonthermal component of the X-ray spectra of solar flares.

When the double linear fit matched better the behavior of φ along time, then there were six options for the evolutionary pattern of the spectral index. Now, the criterion of selection was a comparison between the signs of the slopes of both partial linear fits. If the slope was positive in the first half of spectral time interval and became negative in the second half, then the flare followed a SHS pattern. If the slopes had the opposite behavior, passing from negative to positive, therefore the spectral evolution was considered as *hard-soft-hard* (HSH). Finally, when the slopes had the same sign, it was checked that both were smaller than the critical slope. If so, the analysis for the single linear fit was performed using the average slope, and the spectral evolutions were classified into HHS, FLA, or SHH. Otherwise, the spectral evolution could not be identified and it was labeled as irregular (IRR). Examples of each of the evolutionary patterns mentioned in this subsection are shown in Figure **4-6**. In particular the example flare follows the typical SHS pattern (See Figure **4-5**).

4.1.5. Neupert Effect

One of the observational results that supports the qualitative concept of impulsivity is the Neupert effect (See section 1.2). This effect states that the cumulative HXR flux of a solar flare is proportional to its instantaneous SXR flux (Neupert, 1968, [91]; Hudson, 1991, [61]). In other words, the HXR lightcurve correlates well, both in time and normalized flux, with the time derivative of the SXR lightcurve. The two functional forms of this relation are described in Veronig et al. (2005, [117]) as follows:

$$\int_{t_0}^{t} F_{\text{HXR}}(t')dt' \propto F_{\text{SXR}}(t) \qquad F_{\text{HXR}}(t) \propto \frac{d}{dt}F_{\text{SXR}}(t) \tag{4-2}$$

This correlation between the X-ray emissions represents an energy transfer during a solar flare. The energy deposited by the precipitating electrons during the impulsive phase is accumulated by the ambient plasma as thermal energy (Veronig et al., 2005, [117]). HXR is the manifestation of the electron precipitation, while the plasma heating is exhibited in SXR. In general, the Neupert effect is fulfilled in a bigger proportion in impulsive events, in comparison with gradual ones (Dennis & Zarro, 1993, [35]). Nevertheless, the Neupert effect is not a general rule for all solar flares. In some cases both lightcurves disagrees completely. In the present subsection it is evaluated the degree of correlation between the HXR and the time derivative of the SXR for the example flare. The same procedure explained here was applied to the rest of the sample.

The SXR data for the example flare was provided by the X-Ray Sensor (XRS) on board the GOES-15 spacecraft. The data corresponds to the instantaneous flux in the band $1-8$ Å throughout the analysis time interval of the event, i.e. from 01:37 to 02:35 UT, and had a cadence of 3 seconds. On the other hand, any of the five nonthermal X-ray lightcurves of the example flare could be used as the HXR lightcurve. For the present description LC1 was chosen. Regardless the option selected, the cadence of the HXR lightcurve was of 8 seconds (See subsection 4.1.1). Thus, there

was more data for SXR than for HXR, since the cadence of the SXR was less. Before carrying out the correlation between the X-ray emissions both data arrays must have the same size. Then, the SXR data was resized to the length of the HXR data, and its time derivative was computed. Finally, the HXR lightcurve and the time derivative of the SXR were normalized with respect to their corresponding maximum values, and the resulting arrays were correlated. As result it was obtained the linear Pearson correlation coefficient (r), whose value was among -1 and 1 (Canavos, Sec. 13.8, [19]). The higher the absolute value of r, the better is the correlation. A positive value of r indicated that both lightcurves coincided along time. A negative value of r means that the lightcurves are inversely proportional, i.e. while in one lightcurve the flux increases, in the other one the flux decays, and vice versa. The value of r for the example flare in LC1 was 0.693, which represents a good positive correlation as can be seen in Figure **4-7**.

The value of r allow us to quantify how much the Neupert effect is fulfilled in a given event. Evaluating this correlation coefficient for all the events of the work sample, we noticed it was widely distributed among the interval from -1 to 1. Then, we defined five correlation types with the aim of compare them with the impulsivity types (See sections 1.2 & 5.1). These correlation types are: anti-correlation ($-1 \leq r < -0.15$), null-correlation ($-0.15 \leq r < 0.15$), low-correlation ($0.15 \leq r < 0.35$), medium-correlation ($0.35 \leq r < 0.65$), and high-correlation ($0.65 \leq r \leq 1$). The thresholds between the correlation types were chosen *ad hoc*.

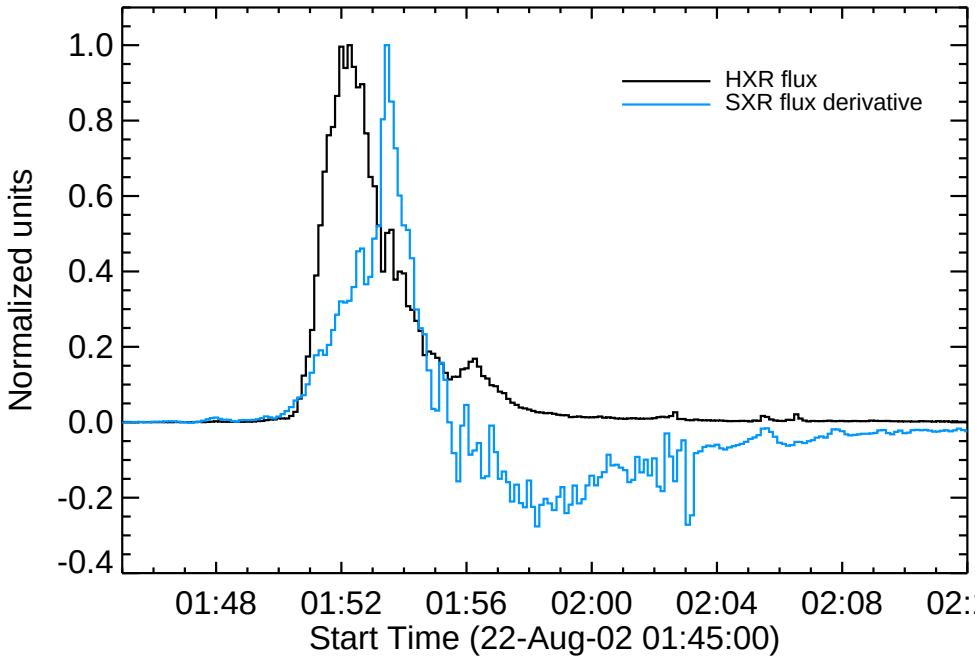

Figure 4-7.: Comparison between the normalized HXR flux (18.5−100 keV) and the normalized SXR time derivative (1−8 Å) for the example flare (SOL2002-08-22T01:57-M5.4). The correlation coefficient between both temporal series is 0.693, which indicates that this event follows the Neupert effect.

4.2. Microwave Radiation Analysis

The midly relativistic electrons that travel inside coronal loops produce the microwave radiation of solar flares. Throughout their descending motion along the loops these electrons spin around the magnetic field lines, emitting light via gyrosynchrotron radiation between the harmonics 10 to 50 of the non-relativistic gyrofrequency (Dulk, 1985, [36]). The latter is $\omega_g = (2.8\ \mathrm{B})$ MHz, with B in Gauss (See equation A-13). For the conditions of the solar corona, B≈100 G, the gyrosynchrotron emissions are expected to be in the range of GHz.

This microwave radiation gives us information about the magnetic trapping of electrons (See section 2.2). The more time the electrons spend inside the magnetic loop because of trapping, the longer will be the corresponding microwave emission. The aim of this section is to evaluate if such trapping exist, and if so estimate how long it takes for each flare of our work sample. In order to achieve this goal the data from NoRP was used, due to it has seven channels around the frequency range of interest (See section 3.2).

The analysis procedure presented here was divided into three parts. Firstly, the lightcurves in microwaves were generated and calibrated from the raw data of NoRP. Secondly, using a spectral analysis there were separated the frequencies at which the emission was purely optically thin. Also at this step, the evolution of the spectral index in microwaves was found in a similar manner as was done for HXR (See subsection 4.1.4). Lastly, the effect of magnetic trapping was quantified via a new observational parameter that we called the *trapping indicator*.

4.2.1. NoRP Lightcurves

As in section 4.1, the descriptions are given for the example flare (SOL2002-08-22T01:57-M5.4). The procedures explained here were applied in the same manner to the rest of the sample. The first step to create the microwave lightcurves was to call the raw data of NoRP. These data were organized in a daily format. For the example flare the restored day was August 22, 2002. The time interval covered by this dataset went from 2002-08-21 22:00 UT to 2002-08-22 08:00 UT, and contained the Stokes parameters I and V for the seven observing frequencies, namely 1, 2, 3.75, 9.4, 17, 35, and 80 GHz in Solar Flux Units (SFU). The temporal cadence of the data was a tenth of second. Besides there was a calibration array called `mvd` that indicated if each value of flux (I or V) was valid or not.

The first modification made to the raw data was to select the timerange corresponding to the analysis time interval used in the HXR analysis, i.e. from 01:37 to 02:35 UT (See subsection 4.1.1). Then, all the non-valid data at any frequency were identified by using the `mvd` array. This is shown in Figure **4-8** for the lightcurve at 9.4 GHz of the example flare. These non-valid data were not taken into account in the subsequent steps of the microwaves analysis.

We worked only with the Stokes parameter I. Hence, hereafter we will refer to it as flux. The background of the flux at a given frequency was found as follows. There were defined two background time intervals. The first of them went from the beginning of the analysis time interval, to the initial time of the flare. The other one started at the end time of the flare, and finished at the end of the analysis time interval. The mean flux at each background time interval was calculated. The background level at the frequency chosen was the minimum between these two mean values. This procedure is illustrated in Figure **4-8** for the lightcurve at 9.4 GHz of the example flare. The same method was applied to all the seven frequencies.

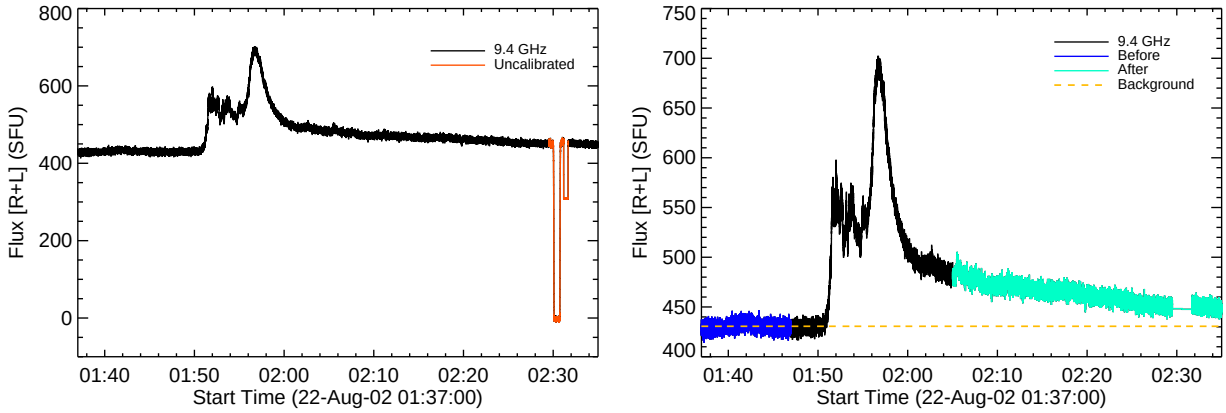

Figure 4-8.: *Left panel:* identification of the uncalibrated data for the 9.4 GHz flux data of the example flare. These data were not considered. *Right panel:* selection of the background time intervals, before the beginning the of the flare (blue data), and after its end (cyan data). The background flux (dashed horizontal line) corresponds to the mean flux value of the background interval before the flare.

The next step was a reduction of the temporal resolution of the data. This was done because we are not interested in the fast varying structures present in solar flares. Instead we wanted to check how all these noisy structures formed a softer lightcurve in a bigger timescale, one order of magnitude greater or so, over which the measurement of trapping is easier to perform (See subsection 4.2.3). Therefore, the flux at all the frequencies were resized to a temporal resolution of 0.5 s, by making sets of five consecutive data and taking the average among them.

Lastly, the background was subtracted to the new data. Thus, the final flux values obtained belong to the microwave radiation exclusively from the flare with a temporal resolution of half a second. The microwave lightcurves of the example flare are shown in Figure **4-9**, except by the lightcurve at 80 GHz. This is because the frequency of 80 GHz was the most noisy of all, and for the most of the flares it was almost flat. Therefore, we decide not to work with this frequency.

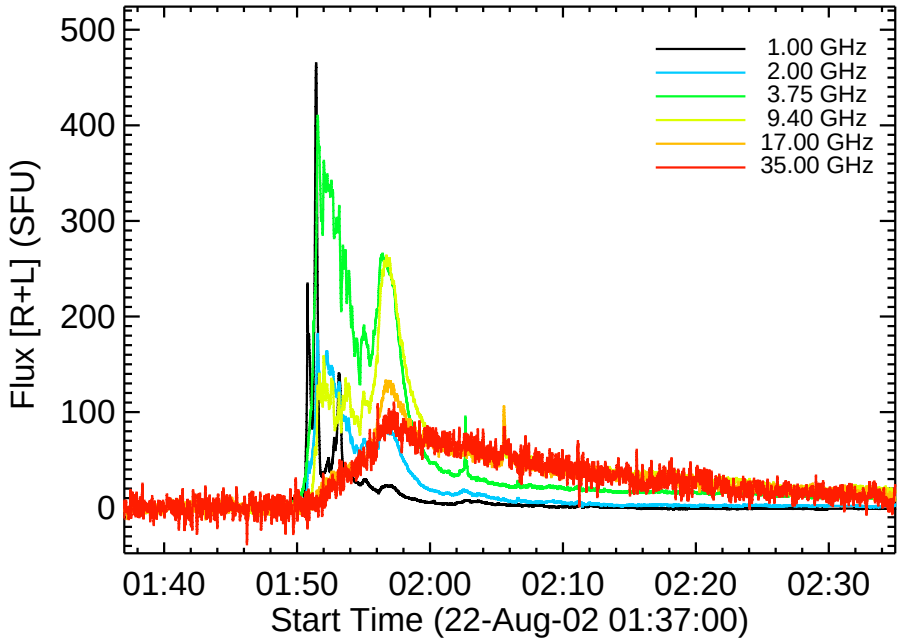

Figure 4-9.: Lightcurves in six of the seven observing frequencies of NoRP, all excepting 80 GHz, for the example flare (SOL2002-08-22T01:57-M5.4). The background of each frequency was subtracted. The temporal resolution was of 0.5 s.

4.2.2. Microwave Spectra

The spectrum of a solar flare in the range of frequencies of NoRP is mainly due to gyrosynchrotron radiation. It has usually two components which are separated by the frequency of maximum energy density ν_p (Dulk, 1985, [36]). In the regime $\nu < \nu_p$ the emission is optically thick and the spectrum has a positive slope in a log-log representation. In the other case, for frequencies greater than ν_p, the emission is optically thin and the spectrum follows a decreasing power-law whose spectral index is expected to be $s = 0.9p - 1.22$, where p is the power-index of the distribution of the midly-relativistic electrons (See section 2.2).

Nevertheless, the observed emission in the optically thick part of the spectrum does not come exclusively from gyrosynchrotron radiation. Other radiative mechanisms like gyroresonance or bremsstrahlung may contribute as their emissivities are important at a few GHz (Gary & Hurdford, Secs. 4.4 & 4.5, [48]). For its part, the optically thin component only accounts for the gyrosynchrotron process. The latter gives us information about the trapping of the electrons, which is what we wanted to study. Therefore, the spectral analysis described here was focused solely on the optically thin part of the microwave spectrum.

We looked for performing a spectral analysis similar to the one developed for HXR, in order to facilitate the comparison between their results. Therefore, the spectral analysis in microwaves was carried out within the spectral time interval used in HXR (See subsection 4.1.1). Additionally, the temporal resolution of the microwave lightcurves was reduced to 8 s, in order to count with the same cadence of the HXR data (See subsection 4.1.1). Due to the choice of the spectral time interval and the reduction of the temporal resolution, each of the six frequencies of NoRP taken into account, all except 80 GHz, had 22 flux data. Therefore, the number of microwave spectra for a given flare of the sample was 22, where the spectrum at the ith time was composed by the six flux values at the ith time.

Now, consider a microwave spectrum at a given time. Its maximum flux and its corresponding frequency were found. The latter was assumed as ν_p. Then, we supposed that all the frequencies larger or equal than ν_p belonged to the optically thin part of the spectrum. Their corresponding flux data were fitted by using a power-law, and its associated spectral index was saved. This power fit could be done if the optically thin part had two or more frequencies with valid flux data, according to the calibration array `mvd` (See subsection 4.2.1). A microwave spectrum of the example flare together with its power fit at the optically thin part is shown in Figure **4-10**. The processes aforementioned were repeated for the 22 spectra.

If a frequency belonged to the optically thin part at least during the 75 % of time spanned by the spectral time interval, i.e. 16 times or more, then we took it as a frequency where the flux was produced solely by gyrosynchrotron radiation. The lightcurves at those frequencies were used to estimate the magnetic trapping (See subsection 4.2.3).

On the other hand, the evolutionary patterns of the spectral index were evaluated in a similar way as was done for HXR in subsection 4.1.4. The main difference was that the linear functions in the double linear fit did not cover the same amount of data. In the HXR case, each linear function fitted half of the spectral time interval, i.e. 11 values of the spectral index, which corresponded to the evolution before and after the peak emission in HXR. Following the same way of thinking, we looked for the peak emission in microwaves within the spectral time interval, adding up the fluxes of the six frequencies. Then, the first linear function fitted all the spectral indexes before the peak emission, while the second linear function fits the remainder data. Additionally, the spectral evolution was evaluated only if there were two or more valid data to fit before and after the microwave peak emission. The validity of the data was checked by using the `mvd` array (See subsection 4.2.1). The estimation of the spectral index and its evolution throughout the flare allowed us to compare the population of electrons inferred from HXR and microwaves emissions as will be seen in section 5.3. The spectral evolution in microwaves for the example flare is illustrated in Figure **4-10**.

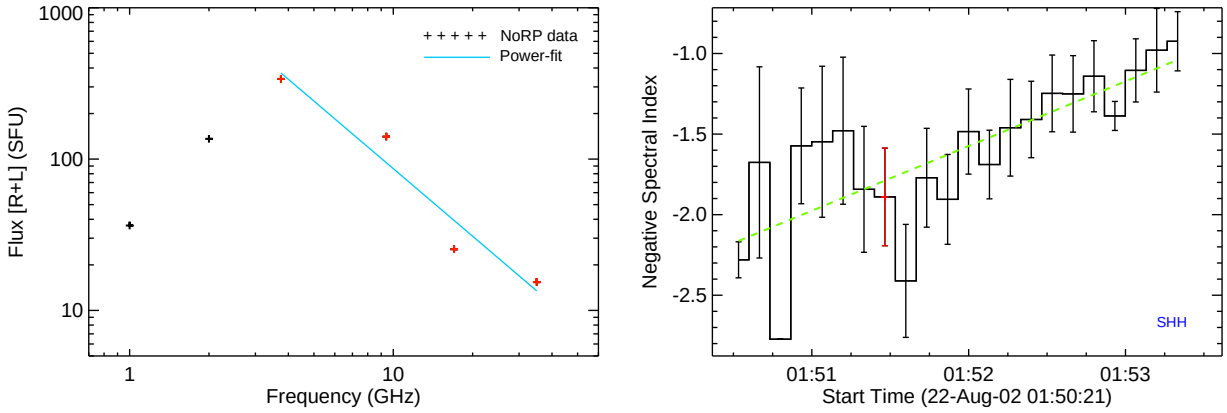

Figure 4-10.: *Left panel*: microwave spectrum of the example flare in the time interval 01:52:00—01:52:08 UT. The plus signs mark the flux data of NoRP. The red ones corresponds to the optically thin part of the spectrum, whose power-law fit is shown in cyan. The spectral index found was s =1.5. *Right panel*: temporal evolution of the spectral index in microwaves for the example flare (SOL2002-08-22T01:57-M5.4). The red point corresponds to the spectral index of the peak emission in microwaves. The evolutionary pattern followed by s was SHH.

4.2.3. Trapping Indicator

The microwave and HXR emissions of solar flares usually present a high correlation. Both lightcurves have almost the same major peaks occurring at very similar times. However, these lightcurves differ mainly in two features. The first difference is the existence of small shifts between their peak times, which makes the HXR to peak earlier. These shifts ranging among 0.1—3.0 s and may be due to larger acceleration timescales, spectral hardening or trapping of the electrons emitting microwaves (Lu & Petrosian, 1990, [84]). The second difference is that the major peaks of the flare decay slower in microwaves than in HXR (Lee, Secs. 9.3.1 & 9.3.2, [77]). Such delays has been successfully explained as an effect of magnetic trapping (Kundu et al., 2001, [75]; Lee et al., 2002, [79]), under the light of the trapping-plus-precipitation model (See section 2.3).

Therefore, the magnetic trapping of electrons in solar flares can be diagnosed by a comparative study between microwaves and HXR, taking advantage of the second difference mentioned above. For this, the duration of the most prominent peaks in both emissions were evaluated. This was already done for HXR, which corresponded to the calculation of the impulsive phase duration (See subsection 4.1.2). Hence, the same method was applied to the microwave lightcurves at the frequencies where the emission comes exclusively from gyrosynchrotron radiation (See subsection 4.2.2), in order to find the impulsive phase duration at each of these frequencies. Finally, the mean of these durations was calculated and it represented the *impulsive phase duration in microwaves* (IPDM). Figure **4-11** shows the estimation of IPDM in the example flare.

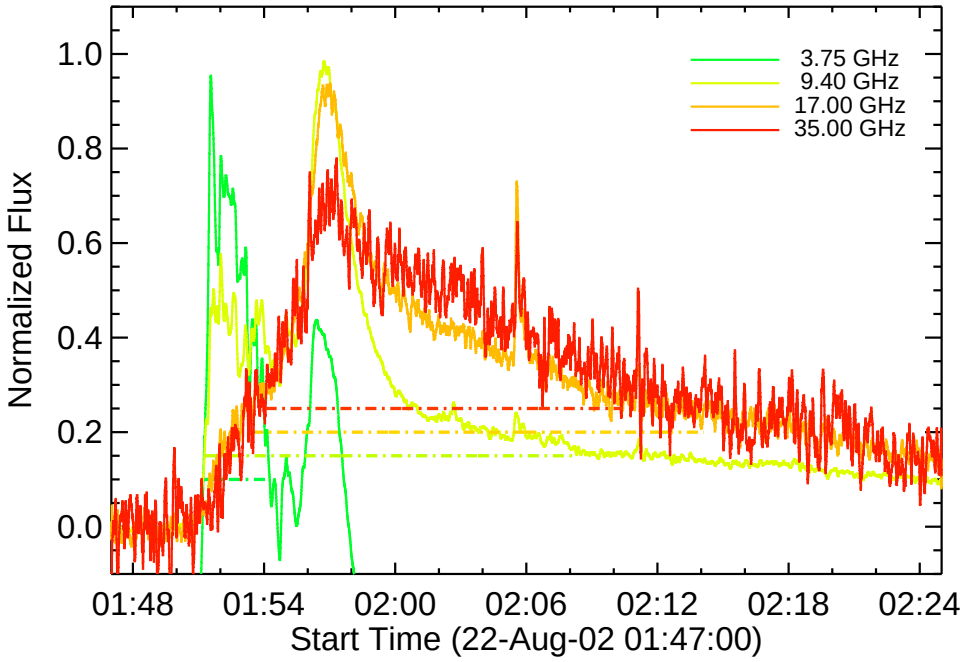

Figure 4-11.: Lightcurves of the example flare coming from gyrosynchrotron radiation. Their impulsive phase durations were 181, 1014, 1240, and 979 s for the frequencies 3.75, 9.4, 17, and 35 GHz, respectively. These results are represented by the horizontal dashed-dotted lines. The IPDM of the example flare was 853 s.

If the magnetic trapping took place, then we expected that IPDM should be greater than IPD. This difference depicted the slower decay observed in microwaves. Then, our interest was to quantify how important was the effect of trapping in solar flares. In order to achieve this purpose, we defined a dimensionless parameter called the *trapping indicator* (TI). The TI corresponded to the percentage difference between both impulsive phase durations, as is shown below

$$\mathrm{TI} = \frac{\mathrm{IPDM} - \mathrm{IPD}}{\mathrm{IPDM}} \tag{4-3}$$

The greater the value of the trapping indicator, the more important is the effect of magnetic trapping. The maximum value has an asymptotic limit which is unity. This limit represents a solar flare where the decay in microwaves is at least one order of magnitude greater than its analogous in HXR. By its part, when the TI is almost null the trapping is negligible and precipitation dominates (See section 2.3). In some strange cases TI can be even negative, which means that the impulsive phase duration in microwaves is less than in HXR. The calculations of TI were done using the IPD measured in LC5, i.e. the nonthermal X-ray lightcurve for the band 30−100 keV. This particular lightcurve was selected because it covered a fixed and broad energy interval. Thus, it collected enough photons to reproduce the major peaks of solar flares at HXR. The TI was computed for all the flares of the work sample. For the example flare it had a value of 0.75.

5. Results

This Chapter is the core of our work, as here we expose how the objectives of this thesis were achieved (See section 1.3). The main insights obtained from the physical properties calculated previously, both in HXR and microwaves, were summarized in four sections. In the first one, the alternative system of classification for solar flares based on the impulsivity parameter (Fajardo et al., 2016, [39]) was tested with the results from the work sample. Besides verifying the correlation between the impulsivity parameter and the degree of symmetry, other relations were studied taking into account the new properties derived from HXR, i.e. the multiplicity, the evolution of the spectral index, and the Neupert effect (See section 4.1). In the second section, the main components of the trapping-plus-precipitation model were compared via their corresponding dimensionless quantities, namely, the impulsivity parameter and the trapping indicator. We examined for which flares precipitation or trapping were dominant, and also the effect of trapping on the different impulsivity types. Then, in the third section, we evaluated if the population of electrons emitting HXR and microwaves was the same. For this, the power index of the distribution of electrons (p) was computed from the spectral indexes in HXR (φ) and microwaves (s), and the results obtained were compared to find similarities. Also, their temporal evolutions were contrasted. Finally, we took a list of reported sunquakes occurred over the timerange spanned by the work sample, and we compared them with our highly impulsive events. This was done to figure out if there was a correlation between these phenomena of solar activity. Thus, we approached to the scientific question proposed in section 1.3. The raw results of the data analysis derived from the whole work sample can be found in Appendix A.3.

5.1. Alternative System of Classification for Solar Flares

The system of classification proposed in Fajardo et al. (2016, [39]) divided solar flares into three types according to their impulsivity parameter values. Such types corresponded to highly impulsive (IP$>$2), medium impulsive (1$\leq$IP$\leq$2), and low impulsive events (IP$<$1). Besides, the IP was computed by using three different nonthermal X-ray lightcurves, the same LC1, LC2, and LC3 used here (See subsection 4.1.1). The results of the system of classification turned out to be independent of the lightcurve chosen to measure the IP. Here, we wanted to check if such independence holds even using the current work sample, which had four times more events than the previous one, and also taking into account two nonthermal X-ray lightcurves that were not considered before, namely, LC4 and LC5.

In order to check such independence, we applied to Table **5-1** a statistical significance test. These kind of tests give as result a probability value or *p-value* between 0 and 1. Our hypothesis was confirmed if the *p-value* was greater than certain significance level. Otherwise it was rejected. The statistical test chosen was chi-square, and we used a significance level of 0.10. The *p-value* found for Table **5-1** was extremely low, $p = 1 \times 10^{-5}$, therefore the alternative system of classification based on the impulsivity depends on the selection of the nonthermal X-ray lightcurve, which is contrary to our initial hypothesis.

IP type	LC1	LC2	LC3	LC4	LC5
High	59	76	65	64	79
Medium	63	65	74	34	53
Low	79	48	63	39	66
NC	7	19	6	71	10

Table 5-1.: Distribution of the work sample into the three impulsivity types. The row labeled as NC shows the number of events that could not be classified, because their lightcurves did not show prominent peaks over the background level. Each column represents the results obtained from a particular nonthermal X-ray lightcurve.

What is the reason behind this unexpected result? To find it out, we must focus on Table **5-1** to look for clues. Immediately, a notorious discrepancy draws our attention. The number of non-classified events (NC) differ appreciably in LC2 and LC4 with respect to the other lightcurves. This could be because for some events LC2 and LC4 did not have enough statistics as their corresponding energy intervals were very narrow (the case of LC2, 30−40 keV) or covered a range of high energies where the emission rate was low (the case of LC4, 50−100 keV). The lack of photons produced noisy lightcurves for such events, where marked emissions were absent. Thus, neither the impulsive phase duration nor the impulsivity parameter could be calculated.

All of these NC events affected the number of flares at each impulsivity type in LC2 and LC4, which generates large differences between the observed and expected values of the contingency table. The overall effect of these differences was reflected by the high value of the statistics (χ^2=171.24), and its respective low *p-value*. Thus, it is plausible to neglect the results from lightcurves LC2 and LC4, and check again our hypothesis. Before doing this, we must bear in mind that the normalization factor changes, and hence the impulsivity parameter values of the work sample. In subsection 4.1.1 we defined the normalization factor as the mean of all the impulsive phase durations measured in the sample. By excluding the IPD results of LC2 and LC4, such mean value is modified to 316.7 s. Therefore, computing the IP with this new normalization factor and neglecting the results of LC2 and LC4, the classification based on impulsivity varies as is shown in Table **5-2**.

IP type	LC1	LC3	LC5
High	62	70	83
Medium	66	71	53
Low	73	61	62
NC	7	6	10

Table 5-2.: Distribution of the work sample into the three impulsivity types. The results of LC2 and LC4 were neglected. The values of the cells changed with respect to Table **5-1** as the normalization factor was recomputed, affecting the IP results and its distribution.

The chi-square test was applied to Table **5-2** and the *p-value* found was 0.214. This value is greater than the significance level, in consequence our hypothesis is confirmed. Thus, the alternative system of classification for solar flares is independent of the lightcurve chosen to measure the impulsivity parameter, provided that such lightcurves belong to broad energy intervals with a low cut-off energy less or equal than 30 keV.

Now, we analyzed the relations between the impulsivity parameter and the other features extracted from the HXR lightcurves and spectra (See section 4.1). Each feature gave a subdivision in the alternative system of classification. The events of the three impulsivity types were distributed into different categories, according to the corresponding feature. This was done for the three lightcurves in which the system of classification was based, namely, LC1, LC3, and LC5.

We started by studying the symmetry of the HXR emission. Here, the degree of symmetry (S) served as the auxiliary feature that subdivide the events of the work sample into three categories of symmetry: dominant injection ($S<-0.2$), symmetrical emission ($-0.2\leq S\leq 0.2$), and dominant decay ($S>0.2$). The classification of the work sample in the three lightcurves of interest using the IP and S together is shown in Table **5-3**. Afterwards, the purpose was to check if the results of the subdivision according to the degree of symmetry varied with the lightcurves. Then, the chi-square test was once again applied to the results of each impulsivity type, i.e. to the 3×3 blocks in Table **5-3**. The *p-values* obtained were 0.947, 0.254, and 0.314, for the impulsivity types high, medium and low, respectively. All of them were greater than the significance level of 0.10. Therefore, the subdivision according to S of the alternative system of classification is independent of the lightcurve chosen to measure the IP and S.

Fajardo et al. (2016, [39]) found that highly impulsive events were specially symmetric, while low impulsive events presented a dominant decay in most of the cases. Additionally, flares with medium impulsivity could have any of both aforementioned HXR morphologies, i.e. symmetrical profiles or long decay profiles. Lastly, the events with dominant injection were rare and they almost did not appear at any impulsivity type. In order to verify these results we selected one of the three lightcurves, and their IP-S classification was studied in detail.

IP Type	LC1	LC3	LC5	S Cat
High	13	12	18	INJ
	20	23	24	SYM
	29	35	41	DEC
Medium	6	5	9	INJ
	27	27	24	SYM
	33	39	20	DEC
Low	10	10	13	INJ
	19	21	23	SYM
	44	30	26	DEC

Table 5-3.: Classification of solar flares according to the impulsivity parameter (IP) and the degree of symmetry (S). The results presented here come from LC1, LC3, and LC5.

The lightcurve chosen was LC5 because it collected the flux of a fixed and broad energy interval. The former characteristic allowed direct comparisons between different events, while the latter ensured enough photon fluxes to reproduce the main emissions of solar flares. Also, this energy range was always nonthermal, except in super-hot flares which are uncommon. In those events, the temperature of their associated coronal loops can reach 30 MK or more, and hence the thermal emission rises up to 50 keV (Tsuneta, 1987, [113]; Caspi et al., 2014, [22]).

In Figure **5-1** can be seen the distribution of the work sample among the different impulsivity types and categories of symmetry for the results obtained from LC5. In contrast with the results of Fajardo et al. (2016, [39]), there was no clear groups in the scatter plot. This makes it difficult to find correlations between both variables. However, these correlations may be hidden as functions of the GOES class. For this reason, the events of the work sample were separated according to their GOES classes in the following subsets: low M class (1.0−2.9), high M class (3.0−9.9), and X class. The IP-S scatter plots were made for each subset (See Figure **5-1**). For the low M class events the points were still broadly spread on the graph. For the higher GOES classes the number of points decreased and an interesting pattern appeared. The impulsivity parameter tends to lower values and the proportion of events with dominant decay increases. This should be due to the duration of the impulsive phase is large in these powerful events, and its most prominent peak appears at the beginning of such phase.

Additionally, some insights about the IP-S relation can be obtained merely by giving a look to Table **5-3**. For example, the events with dominant injection appeared in a less proportion with respect to the other categories of symmetry at all the impulsivity types, as was demonstrated by Fajardo et al. (2016, [39]). The prolonged decay was the most common morphological behavior of the HXR peak emission, even in the high impulsivity type. Thus, symmetrical emissions are no longer distinctive for the highly impulsive events, at least in the current work sample.

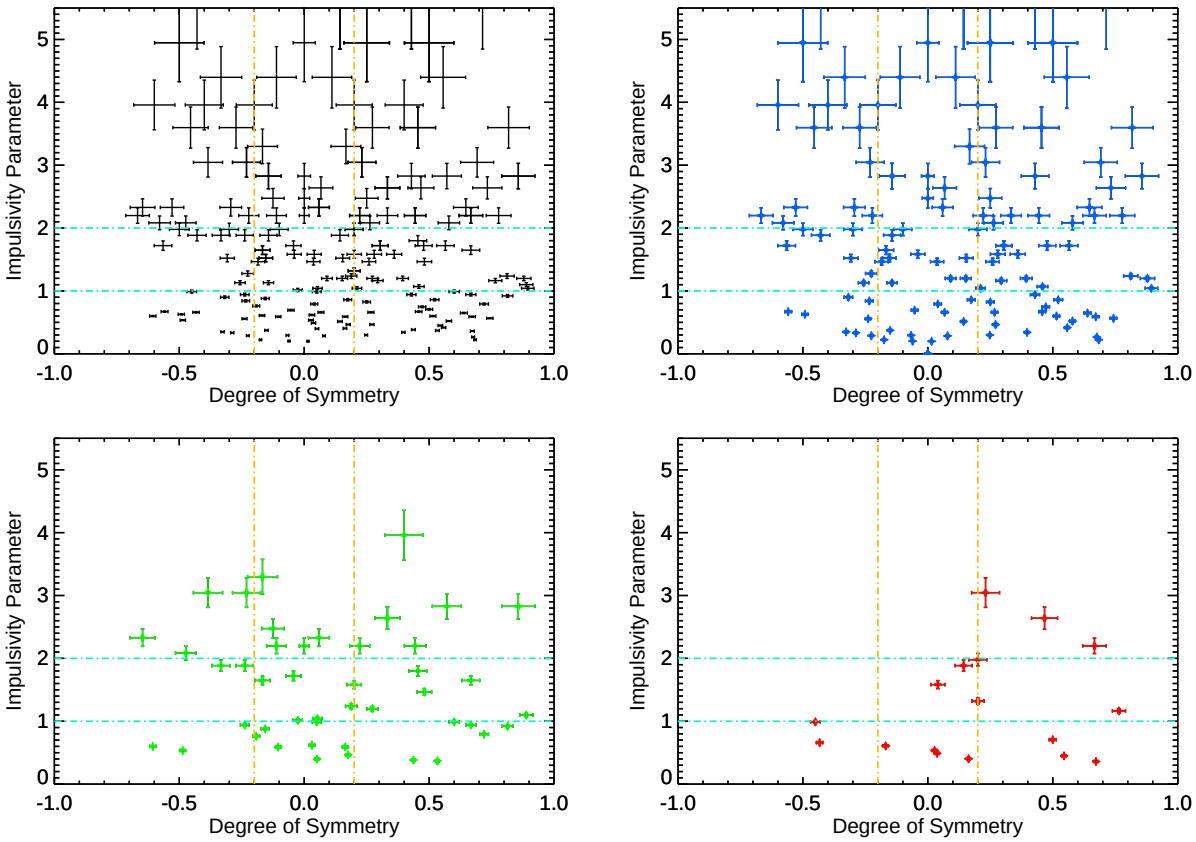

Figure 5-1.: Scatter plots of the impulsivity parameter and the degree of symmetry for the results obtained from LC5. *Upper left panel:* all the events of the work sample classified in LC5 (198). *Upper right panel:* events with GOES classes between M1.0−M2.9 (144). *Lower left panel:* events with GOES classes between M3.0−M9.9 (44). *Lower right panel:* X-GOES class events (18). The low and medium impulsivity types, together with the longer decay profiles are dominant at higher GOES classes.

The next feature to include in the system of classification was the number of peaks occurring during the impulsive phase, or what is the same, the multiplicity. We divided the flares of the work sample into three categories of multiplicity, namely, single peak (SIP), two or three peaks (23P), or multiple peaks (MUP) which were those events having four or more prominent peaks. Table **5-4** shows the subdivision of the impulsivity types into the different categories of multiplicity. As before, the chi-square method was applied giving as result the *p-values* 0.361, 0.843, and 0.891, from high to low impulsivities types. In consequence, the addition of the multiplicity to the system of classification did not affect its independence with respect to the LC1, LC3, and LC5.

Additionally, from Table **5-4** can be inferred that highly impulsive events present predominantly a single peak, while the low impulsive ones have multiple peaks. In the medium type of impul-

sivity the HXR emission may be due to a broad single peak, or two or three consecutive pulses, presumably coming from the same active region. In order to confirm this, an imaging analysis must be performed to locate the nonthermal X-ray sources.

IP Type	LC1	LC3	LC5	MU Cat
High	50	59	74	SIP
	12	11	8	23P
	0	0	1	MUP
Medium	29	29	23	SIP
	32	39	28	23P
	5	3	2	MUP
Low	10	8	8	SIP
	25	26	25	23P
	38	27	29	MUP

Table 5-4.: Classification of solar flares according to the impulsivity parameter (IP) and the multiplicity (MU). The results presented here come from LC1, LC3, and LC5.

Another relevant characteristic for the classification of solar flares was the temporal evolution of the spectral index in HXR. In this case, the subdivisions were not given by ranges of values of certain parameter. Instead, the distinction was made taking into account the evolutionary patterns described in subsection 4.1.4. In summary these patterns were: flat evolution (FLA), monotonically increasing (SHH), monotonically decreasing (HHS), hardening of the spectrum at the peak emission (SHS), and softening of the spectrum at the peak emission (HSH). All the remaining cases which were labeled as irregular (IRR).

The evolutionary pattern was unique for each flare of the sample, because it was calculated from the HXR spectra (See subsection 4.1.1). The diversity of the results for a single flare in the features studied previously comes from their different nonthermal X-ray lightcurves. Hence, this is not the case with the evolution of the spectral index. Table **5-5** shows the distribution of the work sample among the already mentioned evolutionary patterns for the results of LC5. The spectral evolution was estimated solely when the attenuation state of RHESSI was constant throughout the spectral time interval. The events that did not meet this condition appeared in the column denoted as MAS (Multiple Attenuation States) in Table **5-5**. They represented the 44 % of the sample. Another 16.6 % was cataloged as irregular. Therefore, only the 77 remainder flares could be identified among the five evolutionary patterns of interest. The percentages given here were computed taken the total of the sample as the number of classified events according to the impulsivity parameter in LC5, which was 198 (See Table **5-1**).

From the remainder 77 flares the following trends were recognized. The most common evolutionary patterns in the sample were FLA and SHS. In fact, they were particularly relevant for low impulsive events. For the medium type of impulsivity any pattern seems to be more important than the others. This lack of correlation changed for the highly impulsive events due to the preferred pattern were HHS and SHS again. Lastly, the HSH evolution was the weirdest in the sample, appearing only four times. Specifically, this pattern was found in the events 30, 143, 174, and 190, where the numbers represent their IDs in the work sample (See Table **3-3** or Table **A-8**). In fact, we do not know whether it is reported in the literature.

Additionally, our results did not clearly support the work of Grigis & Benz (2004, [51]). Although the SHS evolution was relevant for highly impulsive events, this pattern was not exclusive for such kind of flares. For instance, the SHS evolution was typical in the events with low impulsivity as we mentioned earlier. The work of Kiplinger (1995, [65]) stated that gradual events, the same as low impulsive in this work, follow predominantly the SHH evolutionary pattern. We did not see such preference, but the number of flares following this pattern actually increased at lower impulsivities.

The subdivision of the classification system according to the evolution of the spectral index provided valuable information about solar flares. Nonetheless, we need to be cautious with the trends and conclusions given here, because unfortunately they were derived from less than half of the work sample. Further studies should be implemented to corroborate these conclusions.

IP Type	FLA	SHH	HHS	SHS	HSH	IRR	MAS
High	2	2	8	7	1	10	53
Medium	6	3	5	7	1	6	25
Low	15	5	0	13	2	17	10

Table 5-5.: Classification of solar flares according to the impulsivity parameter (IP) and the evolutionary pattern of the spectral index (SE). These results come from LC5. The last column indicates the amount of flares with multiple attenuator states (MAS). In those cases the evolutionary pattern was not evaluated (See subsection 4.1.4).

The last characteristic involved in the alternative system of classification was the correlation with the Neupert effect. This was evaluated by the linear Pearson correlation coefficient (See subsection 4.1.5), that we denoted in this section as NE. The categories of correlation that subdivide the work sample were: anti-correlation ($-1 \leq \text{NE} \leq -0.15$), null-correlation ($-0.15 \leq \text{NE} < 0.15$), low-correlation ($0.15 \leq \text{NE} < 0.35$), medium-correlation ($0.35 \leq \text{NE} < 0.65$), and high-correlation ($0.65 \leq \text{NE} < 1$). Hereafter, we will refer to them by using the following abbreviations, ANC, NUL, LOC, MEC, and HIC, respectively. The subdivision of the system of classification according to NE appears in Table **5-6**. Unlike previous cases, the Fisher exact test was

implemented in this occasion, because the chi-square method may give incorrect results when a whole row or column of the contingency table to study is null. The *p-values* obtained from the Fisher exact test were 0.241, 0.220, and 0.295 for the impulsivity types high, medium, and low, respectively. Therefore, the independence of the system of classification was once again successfully proven.

We assumed that the Neupert effect is fulfilled if the studied events were within the MEC and HIC categories of correlation. We took the results from LC5 as reference. Then, the fractions of highly, medium and low impulsive events that followed the Neupert effect were 0.76, 0.74, and 0.55, respectively. This is in agreement with the work of Dennis & Zarro (1993, [35]). Therefore, we have confirmed that the impulsivity is directly related to the Neupert effect. On the other hand, the discrepancies at low impulsivities may be due to the NUL category of correlation became important. Perhaps in these events with prolonged HXR emissions the scenario of the energy transfer, from kinetic in the electrons to thermal in the plasma, is no longer true, which leads to the absence of correlation. Another clue in this direction is the existence of anti-correlations between the HXR lightcurve and the time derivative of the SXR lightcurves. Such strange relations only appeared for the low type of impulsivity.

IP Type	LC1	LC3	LC5	NE Cat
High	0	0	0	ANC
	8	8	7	NUL
	7	7	13	LOC
	19	27	33	MEC
	28	28	30	HIC
Medium	0	0	0	ANC
	7	6	3	NUL
	11	8	11	LOC
	28	23	18	MEC
	20	34	21	HIC
Low	3	3	5	ANC
	20	12	15	NUL
	7	3	8	LOC
	24	25	24	MEC
	19	18	10	HIC

Table 5-6.: Classification of solar flares according to the impulsivity parameter (IP) and the correlation with the Neupert effect (NE). The results presented here come from LC1, LC3, and LC5.

The results shown in this section can be modified whether the threshold values that separates the impulsivity types and the different kinds of categories were different. The distribution of the work sample relies on these thresholds which were chosen intuitively. Some improved method of selection must be implemented in the future to avoid the subjectivity in the classification. This will be discussed in Chapter 6.

5.2. Relation Between the Impulsivity and Magnetic Trapping

In Chapter 4 were defined two dimensionless quantities, namely, the impulsivity parameter (IP) and the trapping indicator (TI). The impulsivity parameter tells us how fast occur the precipitation of electrons during solar flares. By its part, the trapping indicator gives account of the magnetic trapping of electrons inside coronal loops. Both processes, precipitation and trapping, take place simultaneously during the impulsive phase, and they determine the kinematics of the nonthermal electrons. We wonder for which kind of flares one process dominates the other. To address this question, we look for a relation between the results of IP and TI in our work sample.

Before describing how we approached to the IP-TI relation, let us explain further details about the calculation of TI. This process was initially exposed in subsection 4.2.3. According to the equation 4-3) the calculation of TI requires the measurement of the impulsive phase duration both in microwaves and HXR, i.e., IPDM and IPD. The accuracy of these measurements could differ a lot, because the corresponding lightcurves had very different cadences, namely, 8 s for HXR and 0.5 s for microwaves (See subsections 4.1.1 & 4.2.1). Such discrepancy in the cadences can affect drastically the value of TI. In order to overcome this difficulty, a new set of nonthermal X-ray lightcurves was generated for the whole work sample. They had a cadence of 2 s and spanned the same energy range than LC5, i.e., 30—100 keV. Thus, the IPD was measured in these new lightcurves. However, the most prominent peak detected in HXR did not always coincide with the most intense microwave emission. Therefore, we reviewed the selection of this peak in HXR in order to ensure its temporal correlation with the peak in microwaves. In this manner, the calculation of TI makes sense.

The use of new HXR lightcurves and the reviewed selection of the peak from which IPD was estimated slightly modifies the distribution of the work sample according to IP. A comparison of the systems of classifications obtained from LC5 with 8 s and 2 s of cadence appears in Table **5-7**. The most significant difference is found in the number of non-classified events. Six additional events could not be classified in the new lightcurves, because the photon flux in the temporal bins of 2 s diminishes enough to eliminate any flare signal above background. This gives a total of 16 events without impulsivity parameter. Besides, from the remainder 192 flares in the sample 15 did not present prominent microwaves emissions, hence the trapping indicator could not be evaluated in those events. So, 177 were the events with successful IP and TI calculations.

Lightcurve	HIG	MED	LOW	NC
LC5 (2s)	77	56	59	16
LC5 (8s)	83	53	62	10

Table 5-7.: Classification of the work sample according to the impulsivity parameter (IP) for LC5 with two different cadences, namely, 2s and 8s. There are six more non-classified events from the new lightcurves.

The results of the impulsivity parameter have already been organized into three different impulsivity types (See sections 1.2 & 5.1). Now, we want to do a similar distinction using the trapping indicator. For this, we made a histogram of the TI results as is shown in Figure **5-2**. The number of bins was given by the square root of the sample size (177 events). The distribution of the trapping indicator has a pronounced peak around TI=0.3, and slowly decaying wings on both sides of the peak. Based on the aforementioned parts of the histogram we define *ad hoc* the following trapping types: short (TI$<$0.216), average (0.216$\leq$TI$\leq$0.383), and prolonged (TI$>$0.383).

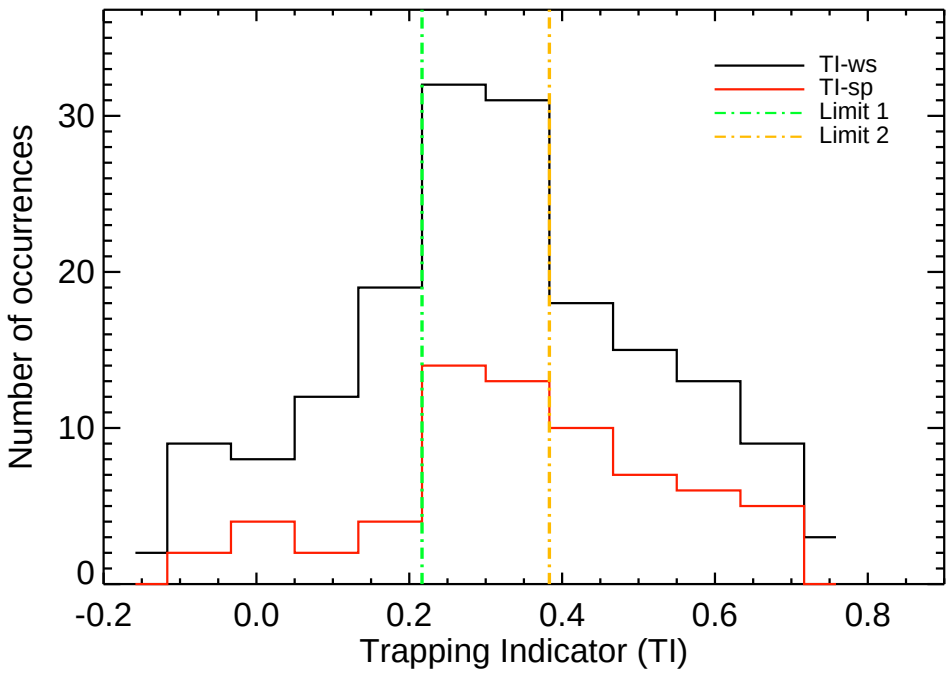

Figure 5-2.: Histogram of the TI results from the whole sample (black distribution), and from a subset having only the single peak events (red distribution). The vertical dashed-dotted lines points out the thresholds between the trapping types.

In order to find some relation between IP and TI, the work sample was classified using the impulsivity and trapping types. This is shown in Table **5-8**. In overall, highly impulsive events show predominantly a prolonged trapping, while for flares with lower impulsivity the effect of

trapping is usually poor. This result was expected, because the definition used for the trapping indicator. Let us suppose two events, one very impulsive having a single peak, and other one of low impulsivity with multiple peaks. In the former, the IPD is short and even a small difference between the impulsive phase duration in microwaves and HXR (IPDM−IPD) generates an appreciable value of TI. In the other case, the IPD is large and may represent the duration of the envelope formed by all multiple peaks. Each of those peaks has its own slow decay in microwaves, but because they occur consecutively only the decay of the lasts peaks are detectable in the measurement of IPDM. The combination of both factors, a large IPD and a small IPDM, makes the TI enters to the short trapping type in these gradual (low impulsive) and bursty (multiple peaks) events.

TI Type	Whole Sample			Single Peak Events		
	HIG	MED	LOW	HIG	MED	LOW
SHO	6	22	28	2	6	6
AVG	29	18	16	17	7	3
PRO	34	13	11	20	5	3
NMR	8	3	4	0	0	0

Table 5-8.: Classification of solar flares according to the impulsivity parameter (IP) and the trapping indicator (TI). The Table presents two set of results, for the whole sample (left) and for the single peak events (right). These results come from LC5 with 2 s cadence.

For all the above, we recognize that events of different nature should not be mixed in this analysis, because the interpretation of their observables do not always coincide. For this reason we focus only in events with a single peak in HXR and microwaves. In total, there are 69 of these flares in the work sample. Their distribution among the trapping types was evaluated as shown in Figure **5-2**. We can conclude that: first, the trapping types are well defined, even for this particular subset of the sample. Second, the precipitation and trapping can be studied in these single peak events like different behaviors of an *Universal Lightcurve*, making the analogy with the *Universal Spectra* defined by Gary & Hurford (Sec. 4.4, [48]).

The Universal Lightcurve has two components, one due to precipitation which is observed in HXR, and a second due to magnetic trapping from microwaves. If their tails are close enough (TI$<$0.216), then precipitation dominates. Otherwise, trapping dominates whether their tails are widely separated (TI$>$0.383). In the range between both regimes, we cannot say which process is the most relevant. Thus, the trapping types discriminate when precipitation or trapping are dominant. Examples of each trapping type, together with the shape of the Universal Lightcurve are shown in Figure **5-3**.

The single peak events were classified according to IP and TI as was done for the whole work sample. The results appear in Table **5-8**. Again, the IP-TI relations of the subset resembles to that of the whole sample. Prolonged and short trapping types are typical for events with high and low impulsivities, respectively. This result may indicate that a long IPD in HXR could be generated by many short pulses, even if it is observed as a single peak in HXR. Because of this, the evidence of trapping is elusive for low impulsive events.

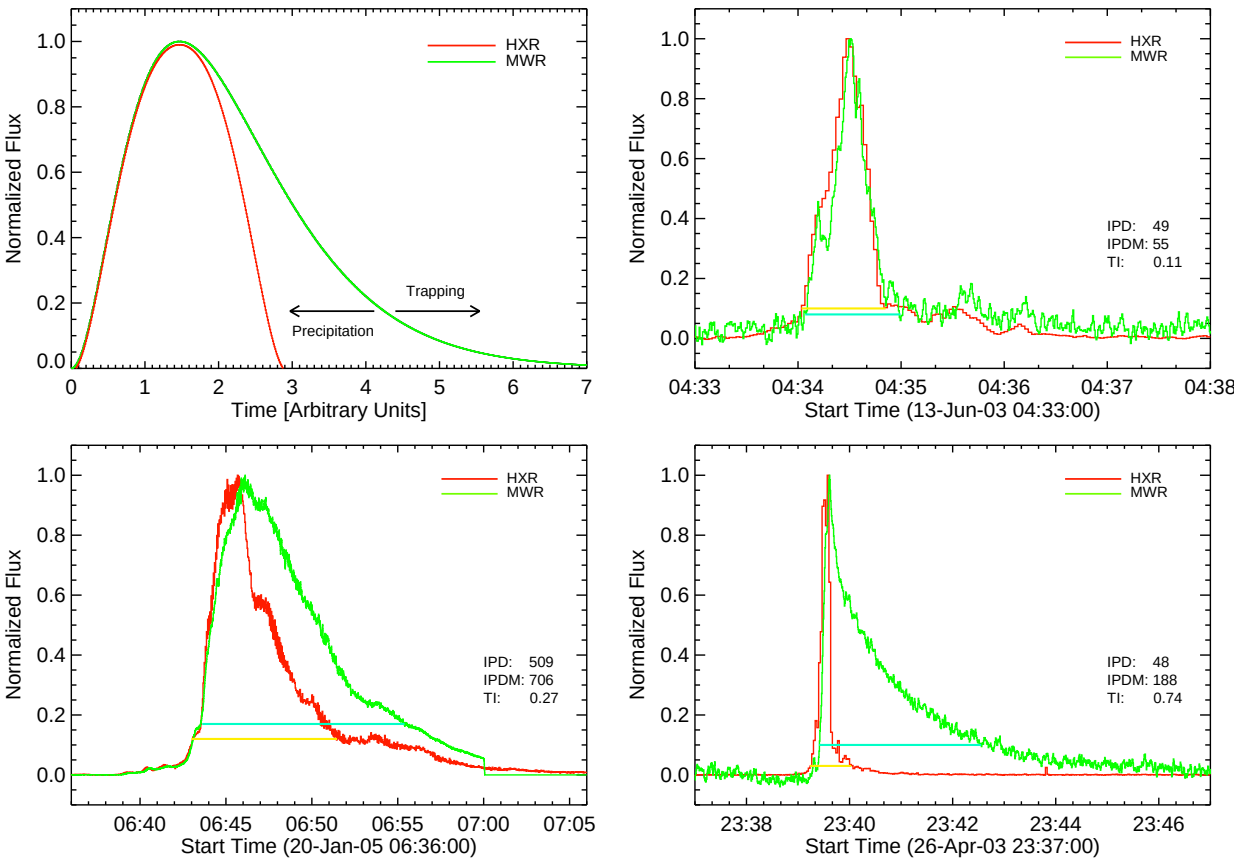

Figure 5-3.: *Upper left panel:* Universal Lightcurve of a single peak in HXR and microwave radiation (MWR). The arrows point out when precipitation or trapping dominates. *Upper right panel:* event where precipitation is relevant. Corresponds to the ID 64 of the work sample. *Lower left panel:* flare belonging to the average trapping type (ID 123). *Lower right panel:* event with an evident domination of magnetic trapping (ID 51). In the three examples with observational data, the yellow and cyan horizontal lines mark the impulsive phase durations in HXR and MWR, i.e. IPD and IPDM, respectively.

5.3. Population of Electrons in HXR and Microwaves

The nonthermal X-ray emission of solar flares is typically described by a power-law, whose spectral index we denoted throughout the text as φ. This spectral index was estimated in the spectral fitting process via the broken power-law function (`bpow`) available in `OSPEX` (See subsection 4.1.1). Because φ varies with time, its temporal evolution was found and classified into different evolutionary patterns (See subsection 4.1.4). The optically thin part of the microwave spectra of solar flares also follows a power-law. Its spectral index was denoted by s, and it was computed by implementing a power-law fit to the optically thin frequencies observed by NoRP instrument (See subsection 4.2.2). Also, its evolutionary pattern was evaluated.

From φ it is possible to infer the power-index p of the distribution of electrons emitting in HXRs. The only condition needed is to assume a model of HXR emission, i.e. thin-target or thick-target model (See section 2.1). In the thin-target model the relation between both indexes is $p = \varphi - 0.5$, while for the thick target model is $p = \varphi + 1$ (Hudson, 1972, [60]). Likewise, there is a couple of expressions that relate s with the power-index of the electrons emitting microwaves. The two cases come from considering gyrosynchrotron or synchrotron radiation as the dominant mechanism producing the microwave emission. These expressions are $p = (s + 1.22)/0.9$ and $p = 1 - 2s$, for gyrosynchrotron and synchrotron, respectively.

According to the trapping-plus-precipitation model, the distribution of electrons producing both types of emissions, HXRs and microwave radiation, should be the same (See section 2.3). In this section, we want to corroborate this statement. For this, the average value of φ and s were computed for each event in the sample, and from these averages, the possible values of p were estimated by applying the expressions mentioned above. The population of electrons is the same if the difference between a given pair of power indexes p, one derived from HXR and the other from microwaves, is small. Then, we computed the differences of all the possible combinations of power indexes, namely, thin-target with gyrosynchrotron, thick-target with gyrosynchrotron, thin-target with synchrotron, and thick-target with synchrotron. The minimum of all those differences was identified, and if it was less than 1.0, then we assumed that the event was generated by the same population of electrons via the radiation mechanisms that produce such small difference in p. The values of the power index p and their corresponding differences can be inferred from the averages of φ and s, which are presented in Tables **A-7** and **A-10**. Additionally, the events having the same population of electrons are listed in Table **5-9**.

The number of events having the same population of electrons in HXR and microwaves are 58. The most typical combination of emission models found was thin-target together with synchrotron radiation. It appeared in a proportion of 62 %. The other important combination involved again the thin-target model, this time together with gyrosynchrotron radiation. This combination takes place 14 times in the events listed in Table **5-9**. The remainder combinations were

ID	Combination	ID	Combination	ID	Combination	ID	Combination
2	Thin-Sync	61	Thick-Gyro	107	Thick-Sync	148	Thick-Sync
6	Thin-Sync	64	Thin-Sync	108	Thin-Sync	149	Thick-Gyro
7	Thin-Sync	66	Thin-Gyro	109	Thin-Gyro	155	Thin-Sync
11	Thin-Sync	67	Thin-Sync	111	Thin-Sync	160	Thin-Sync
12	Thin-Sync	70	Thin-Sync	112	Thin-Gyro	162	Thin-Sync
14	Thin-Gyro	73	Thin-Sync	113	Thin-Gyro	165	Thin-Sync
16	Thin-Sync	74	Thin-Sync	116	Thin-Sync	175	Thin-Sync
19	Thin-Sync	79	Thin-Sync	117	Thin-Gyro	190	Thin-Gyro
22	Thin-Sync	80	Thin-Sync	119	Thin-Sync	193	Thin-Gyro
24	Thin-Sync	82	Thin-Sync	120	Thick-Sync	196	Thick-Sync
37	Thick-Sync	83	Thin-Sync	123	Thin-Gyro	199	Thin-Sync
38	Thin-Gyro	91	Thin-Sync	131	Thin-Sync	205	Thin-Sync
40	Thin-Sync	92	Thin-Sync	133	Thick-Gyro	206	Thin-Gyro
49	Thin-Gyro	97	Thin-Sync	134	Thin-Sync		
59	Thin-Gyro	103	Thin-Gyro	143	Thin-Sync		

Table 5-9.: List of events whose power indexes p are very similar according to a given HXR emission model (thin-target or thick-target), and to a regime of radiation driven by the magnetic field (gyrosynchrotron or synchrotron). It is highly probably that both emissions were generated by the same population of electrons in these events.

not very recurrent, and both were associated to the thick-target model. The evident relevance of the thin-target model may be a consequence of not discriminating the location of the HXR sources. Perhaps, the integrated flux of the X-ray spectra has coronal contributions hiding out the chromospheric ones. Thus, the thick-target emission is difficult to see. In order to confirm this hypothesis, the spectral analysis must be implemented in confined regions of coronal loops, e.g. in the footpoints, and the body of the loop or its apex. Previous studies of this type have been carried out before using also RHESSI data (Simões & Kontar, 2013, [104]).

On the other hand, the evolutionary patterns of the spectral indexes in HXR and microwaves were compared. This is shown in Table **5-10**. In most of the cases the temporal evolution of the spectral indexes could not be evaluated, because of multiple attenuator states in RHESSI (for φ) or due to lack of data in the optically thin part of the microwave spectra (for s). Furthermore, the spectral evolution was classified as irregular in a large proportion of the sample. Leaving aside all these non-classified or irregular events, the main trends found in Table **5-10** were the following. First, only 34 events have a valid spectral evolution for both types of emission. Second, the most important evolutionary patterns in microwaves were SHH and HSH. The former was already reported by Silva et al. (2000, [103]), while the latter is much more common than in HXR.

The events that followed the interesting HSH evolutionary pattern can be found in Table **A-11**. Third, the SHS pattern is dominant in HXR as expected. Lastly, 30 out of the 34 events classified correctly are within the dominant evolutionary patterns mentioned previously.

		Evolutionary Patterns in HXR						
		FLA	**SHH**	**HHS**	**SHS**	**HSH**	**IRR**	**MAS**
Patterns in MWR	**FLA**	0	0	0	0	0	2	1
	SHH	3	1	1	7	0	5	12
	HHS	0	0	1	2	0	2	2
	SHS	1	0	1	3	1	0	5
	HSH	3	5	0	5	0	3	14
	IRR	3	1	2	6	2	10	16
	FEW	13	3	8	4	1	19	40

Table 5-10.: Comparison of the temporal evolution of the spectral indexes in HXR and microwaves, i.e. φ and s. The evolutionary patterns correspond to those defined in subsection 4.1.4. The last row, labeled as FEW, represents the events in which the microwave spectra did not have enough data to evaluate the evolution of the spectral index in microwaves (s). The green cells show the 34 events classified correctly both in HXR and MWR.

5.4. Highly Impulsive Events and Sunquakes

Sunquakes are seismic emissions observed over the solar surface produced by flares. They are seen in the line-of-sight velocity maps of the solar disk as wavefronts that propagate away from a point source. They are usually accompanied by kernels of HXR and white-light continuum emissions (Martínez-Oliveros et al., 2008, [87]). The first detection of these events was reported by Kosovichev & Zharkova (1998, [71]). Since then, the methods of detection have evolved and now the main techniques used for this purpose are: time-distance, ring diagrams, and helioseismic holography (Chaplin, Ch. 10, [25]). Additionally, they have been proposed several hypotheses that explain the generation of these acoustic signals. Such hypotheses are summarized in Buitrago-Casas et al. (2015, [18]). In particular, here we want to check if sunquakes are correlated with the direct impact of high energetic electrons on the lower layers of the solar atmosphere.

We believe that only certain kind of flares are capable of generating sunquakes via the aforementioned mechanism. We suppose that these flares should be very impulsive and must be not

dominated by magnetic trapping. The former condition ensures that the duration of the precipitation of electrons is short, while the second one guarantees that the energy carried by the electrons is deposited at the footpoints, i.e. in the chromosphere or photosphere (Martínez-Oliveros, Sec. 5, [86]). Thus, a vast amount of energy is injected suddenly to these lower layers, and as consequence the acoustic disturbances are produced. These disturbances should be localized within or close to the precipitation region. Indeed photospheric observations of Doppler velocities reveal that seismic kernels, both sources and subsequent wavefronts, do not appear nor propagates far way from its associated active region.

In order to validate the previous scenario in at least one event, we match a database of seismically active solar flares. We used the list published by Buitrago-Casas et al. (2015, [18]). Only 7 out of these 18 seismically active events were in our sample. For these events, the impulsivity and trapping types were consulted from our results and, they are shown in Table **5-11**. We found that the medium and high impulsivity types, together with the short and average trapping types are recurrent in these 7 events. In particular, there is one event (ID 60) whose impulsivity is quite large and its magnetic trapping is very poor. All of this observational evidence gives support to our hypothesis that impulsive events having a dominant precipitation can generate sunquakes. Thus, we address our scientific question exposed in the objectives of this thesis (See section 1.3). The remainder 11 seismically active events were absent in the work sample because they do not have available data in RHESSI or NoRP, or its GOES class was less than M1.0, or due to they are out of the timerange of our sample.

ID	Peak Time	Class	IP Type	TI Type
151	2011-02-15 01:55	X2.2	LOW	SHO
161	2011-07-30 02:09	M9.3	HIG	SHO
170	2011-09-26 05:07	M4.0	MED	SHO
175	2012-05-10 04:17	M5.7	MED	AVE
178	2012-07-05 03:35	M4.7	HIG	AVE
180	2012-07-06 01:39	M2.9	HIG	AVE
202	2013-11-07 03:39	M2.3	MED	SHO

Table 5-11.: Comparison of the events having sunquakes reported by Buitrago-Casas et al. (2015, [18]), with the work sample. The impulsivity and trapping types of these events are reported. From them we conclude that low impulsivity and prolonged trapping are poorly associated to the generation of sunquakes.

6. Conclusions

The general objective of this thesis is to deepen the understanding of the impulsivity of solar flares. In order to achieve this goal, a quantitative concept of the impulsivity is postulated, which is supported by the theoretical background of the trapping-plus-precipitation model. Here, the impulsivity was devised as a tracer of the electron precipitation in solar flares. We propose that it can be calculated as the duration of the most prominent HXR peak, because this emission is mainly produced by the precipitating electrons when they collide against the denser layers of the solar atmosphere. This observable is called the *impulsivity parameter*.

The other component of the trapping-plus-precipitation model gives account of the electrons that propagates along coronal loops and are trapped by the strong gradients of magnetic field at the converging legs of the loops or footpoints. These trapped electrons are observed in microwaves because they emit gyrosynchrotron or synchrotron radiation throughout their journey in the magnetized plasma. Taking this into account, an additional tracer is estimated from the microwave emissions giving information on the effectiveness of the magnetic trapping. This one is called the *trapping indicator*. In this manner, precipitation and trapping complement each other and describe the kinematics of the electrons that propagate inside coronal loops. In this picture, the impulsivity represents only one of these processes, namely, precipitation.

A set of applications and tests of this quantitative approach were implemented in a work sample composed by 208 solar flares. These events took place from February 2002 to December 2013, and belonged to GOES classes greater or equal than M1.0. First, the classification criteria described in Fajardo et al. (2016, [39]) were applied to the work sample. The system divided solar flares in three impulsivity types, namely, high, medium, and low. The fact that such classification is independent of the nonthermal X-ray lightcurve chosen to measure the impulsivity parameter is confirmed. However, the energy intervals of the lightcurves under consideration should be broad, spanning 30 keV or more, and its low energy cut-off must be within 20—30 keV. The validation of the classification system of solar flares based on impulsivity was made by applying the chi-square significance test to the classifications obtained from different lightcurves.

This alternative classification was subdivided by using other observables derived from the HXR lightcurves and spectra. These observables were: the degree of symmetry of the most prominent emission, the number of peaks observed during the impulsive phase or *multiplicity*, the evolution of the spectral index, and the correlation with the Neupert effect. Each of these observables sub-

divided the impulsivity types into different categories. Such subdivisions in the classification system also turned out to be independent from the lightcurve used to calculate the respective observables. The main correlations found between the impulsivity types and the different kind of categories are summarized below.

The highly impulsive events have usually a single peak, and in the most of the cases they fulfilled the Neupert effect as was expected from Dennis & Zarro (1993, [35]). On the other hand, flares with low impulsivity present multiple peaks and the typical evolutionary pattern of their spectral indexes were *Soft-Hard-Soft* or flat. A special mention deserve the result found between the impulsivity and the symmetry of the HXR emission. Surprisingly, these did not show a clear relationship as was expected from Fajardo et al. (2016, [39]). However, an association appeared when events were separated by GOES class. The events of higher class had low values of the impulsivity parameter, and the decay time of the HXR peak was longer than its rise time. This may be because these events have multiple peaks and were low impulsive, with the most prominent peak occurring at the early phase of the flare. The aforementioned results of the alternative system of classification allow us to conclude that the first specific objective of this work was achieved.

Second, the trapping indicator was calculated for the whole work sample, and from it three different trapping types were defined, namely, short, average, and prolonged. These types determined regimes of magnetic trapping for events with a single peak. Therefore from these flares one is able to discriminate whether precipitation or trapping dominates. For this, the concept of *Universal Lightcurve* was employed analogously to the *Universal Spectra* defined by Gary & Hurford (Sec. 4.4, [48]). Additionally, the trapping types were contrasted with the impulsivity types. It was found that efficient trapping was common on highly impulsive events, while short trapping appears to be more correlated with low impulsive events. Thus, we investigated magnetic trapping in solar flares, and its effect on the impulsivity as was proposed in our second specific objective.

The last application joined the concepts of impulsivity and trapping, in order to study their role in the generation of sunquakes. We studied the database of seismically active flares of Buitrago-Casas et al. (2015, [18]), and we complemented it by adding their respective impulsivity and trapping types. We find that these events were predominantly medium or highly impulsive, having a non-efficient magnetic trap. This is in agreement with the hypothesis that sunquakes are generated by the direct impact of high energetic electrons on the lower layers of the solar atmosphere. With this, we addressed the scientific question formulated in section 1.3, and therefore all the specific objectives of this thesis were fully met.

In addition, there were other results that deserve a special mention. According to the trapping-plus-precipitation model the population of electrons emitting HXR and microwaves should be the same. We developed a method to prove the previous statement. This method was based on computing the power-index p of the electron distribution from the spectral indexes of the observed HXR and microwave emissions, i.e. φ and s, respectively. Four possibilities for the power-index were obtained by taking into account two HXR emission models, thin-target and thick-target, and two regimes of microwave radiation, gyrosynchrotron and synchrotron. The differences between the possible combinations of p were calculated. If the minimum of such differences was less than 1.0, then the population of electrons producing both emissions was considered the same, and the HXR emission model together with the regime of microwave radiation were plenty identified. This method could give good results whether φ and s were estimated correctly from observations. Unfortunately, we counted with a high uncertainty in the values of s, because they were derived from the microwave spectra that had fewer points than HXR spectra, three or four in the best cases. Despite of this difficulty with the data, the development of the method is valuable.

On the other hand, the spectral analysis in HXR and microwaves gave two important results. First, we found five evolutionary patterns of the spectral indexes. The most interesting pattern was *Hard-Soft-Hard*. It almost did not appear in HXR, but had an important role in the evolution of microwave spectra. We invite the community to confirm the existence of this pattern. The results summarized in Tables **A-8** and **A-11** can be used as a starting point for this search. Additionally, the comparison between the temporal evolution of φ and s indicates that one of the typical evolutionary patterns in HXR is *Soft-Hard-Soft*, while the common pattern in microwaves is *Soft-Hard-Harder*. This agrees with the result obtained by Silva et al. (2000, [103]).

Future development will be concentrated in removing the subjectivity of the alternative system of classification. Now, the impulsivity types depends strongly on the selection of the threshold values between the different types. The same occurs for all the categories that subdivide the classification. These thresholds were chosen *ad hoc*, and therefore they introduced the subjectivity. In order to avoid this, we want to implement a statistical clustering method like *k-means*. This will allow us to confine the events having correlations within well defined ranges of the respective observables. Besides, the correlations can be made with more than two observables. Thus, relations like impulsivity-symmetry-multiplicity can be performed easily. Finally, we will explore further applications of the Universal Lightcurve, by determining what process dominates, precipitation or trapping, in other solar flares having a single peak during the impulsive phase.

A. Appendices

A.1. Brief Introduction to the Sun

The Sun is a main sequence star at the half of its evolutionary stage. Its current age is roughly 5000 million years old, estimated from the decay of radioactive isotopes in meteorites (Stix, Sec. 2.2, [107]). Its composition, derived from spectroscopic measurements of the surface, is 74 % Hydrogen, 24 % Helium and 2 % of heavier elements. The distribution of these abundances changes radially inwards, increasing the amount of Helium up to 64 % and decreasing the fraction of Hydrogen to 34 % at the core (Bahcall et al., 2005, [7]). The effective temperature of the Sun is nearly 5700 K and its luminosity is $3{,}85 \times 10^{26}$ W. According to the spectral Harvard's catalog the Sun is a G2V star (Karttunen et al., Secs. 8.2 & 8.3 and citations within, [64]). A summary of the main global parameters of the Sun are shown in Table **A-1**.

Parameter	R (km)	M (kg)	T_{ef} (K)	L (erg s^{-1})	A (years)	$\langle B \rangle$ (G)	$\langle P \rangle$ (days)
Value	7×10^5	2×10^{30}	5770	$3{,}8 \times 10^{33}$	5×10^{10}	5-10	27.3

Table A-1.: Main parameters of the Sun as a star. The convention for the solar parameters is R, M, T_{ef}, L, A, $\langle B \rangle$ and $\langle P \rangle$, representing radius, mass, effective temperature, luminosity, age, average polar magnetic field strength and average rotation period at the surface, respectively. These values were acquired from Stix (Secs. 1.2, 1.3, 1.4 and 7.1, [107]), excepting $\langle B \rangle$ which was taken from (Cohen, Sec. 4.1.1, [26]).

Structure

Four regions compose the interior of the Sun. The deepest of these regions is the *core*, where the energy is generated via thermonuclear fusion reactions. Most of the energy is produced by the first branch of the proton-proton chain (ppI), which at the core temperature of approximating 1.5×10^7 K is the most efficient mechanism of energy conversion in comparison with other fusion reactions such as the pp-II, the pp-III and the CNO cycle (Bhatnagar & Livingston, Sec. 3.1.2, [14]). All the latter together just contribute the 9 % of the output energy (Karttunen et al., Sec. 10.3, [64]). In terms of size, it is believed that the core extents around 0.25 $R_\odot$ (Bahcall &

Ulrich, 1988, [8]). Beyond this radius no more energy is generated, hence the luminosity saturates at such location and remains almost constant along the rest of the interior at around the value observed at the solar surface (See Table **A-1**) . Therefore, the energy is just transported via different transfer mechanisms from the border of the core the to the outer inner regions.

In the region between 0.25 and 0.70 $R_{\odot}$, the energy is transported by radiation, giving the name to this layer, the *radiative zone*. The plasma inside the radiative zone can be considered as a stratified series of thin shells, whose density, pressure and temperature decreases radially outwards. Each of those shells is in hydrostatic equilibrium and in Local Thermodynamic Equilibrium (Chandrasekhar, Sec. V.3 and V.5, [23]). This region is usually modeled by the equation of state of an ideal gas, to simplify the theoretical analysis of the mechanical and thermodynamic behavior of the plasma.

At around 0.70 $R_{\odot}$ the opacity of the medium increases and the energy cannot be further propagated via radiation (Bhatnagar & Livingston, Sec. 3.1.3, [14]). Additionally, due to small fluctuations in the solar structure, some parcels within a same thin shell can be displaced from its equilibrium position generating stable or unstable motions. Let us suppose such displacements are given radially outwards. If the density difference between the parcels and the new surrounding shell is negative, then the parcels will tend to rise according to the Archimedes' principle, leading to the unstable scenario. Otherwise the perturbation is stable and the parcels will move to their original position. For the unstable case, the hydrostatic equilibrium is broken and these upwards motions become recurrent, carrying with them the energy from the inner layers. This transfer mechanism is known as convection and it is the dominant at the outer envelope of the solar interior called *convective zone*. This stability condition is usually expressed in astrophysics as a comparison between the absolute values of the temperature gradients of the rising parcels (adiabatic gradient) and the medium (radiative gradient), which is known as the *Schwarzschild criterion* (Landau & Lifshitz, Sec. 1.4, [76]; Hansen & Kawaler, Sec. 5.1.1, [54]). The Schwarzschild criterion states that the transfer mechanism with the smaller absolute gradient dominates the energy transport.

There is an interesting thin layer between the radiative zone and convective zone called *tachocline*. Its name comes from the words *"takhos"* and *"cline"* which together means difference in velocity. In effect, this is an interface region where the rotational behavior of the solar interior changes. Inside the radiative zone the plasma rotates as a rigid body, while at the convective zone the angular velocity depends on latitude (Foukal, Sec. 7.1.2, [45]). Thus, the plasma in the tachocline must hold strong shear forces. Additionally, it is believed that the large-scale toroidal magnetic field of the Sun is generated at this layer, which rises by buoyancy through the whole convection zone reaching the surface to form sunspots (Guerrero et al., 2016, [52]). However, other authors affirm that the sunspots formation is a shallower process driven by turbulence in stratified layers near surface (Losada et al., 2017, [83]).

The visible surface of the Sun or *photosphere* is the outer of the inner regions, and also the lowest of the atmospheric ones. It is not as thick as the previous zones, having approximately 400 km of width (Fraknoi et al., Sec. 15.1, [47]). This is the first region we can directly observe, as is it optically thin in the visible range (See appendix A.2.4). The rest of the solar interior is totally opaque to radiation and it can only be studied from indirect methods such as helioseismology and neutrinos detection (Chaplin, Ch. 5 & 8, [25]). The temperature of the photosphere corresponds to the effective temperature of the Sun. The typical photospheric density is of the order of 10^{-9} g/cm^3 (Eddy & Ise, Ch. 2, [38]). Figure **A-1** shows all the inner layers of the Sun.

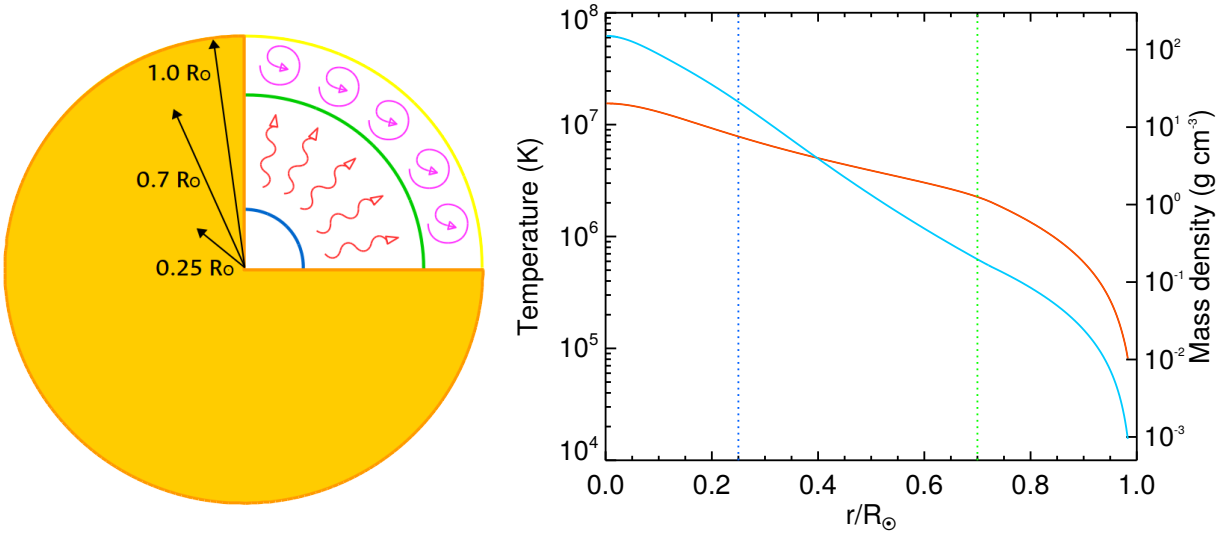

Figure A-1.: *Left panel:* sketch showing all the internal solar layers. The blue and green circle segments point out the border of the core and the tachocline locations, respectively. *Right panel:* temperature and density profiles throughout all the solar interior. These data were taken from the Standard Solar Model (BS2005-AGS,OP). The vertical dotted lines represent again the border of the core and the tachocline locations.

Above the photosphere there are two atmospheric layers, both can be observed from Earth with the naked eye during a total solar eclipse (See Figure **A-2**). Just before the solar disk have been covered by the Moon, a slight pink emission appears surrounding almost the full disk. This comes from the layer which is just above the photosphere, which receives the name of *chromosphere* that means "zone of color". The light observed comes mainly from Hα (6563 Å). Besides this emission line, there are other important lines such as CaII (H and K) and SiI (1520 Å). The latter can only be produced in a non-LTE medium (Vernazza et al., 1973, [114]). Additionally, the temperature in this region exhibits a particular behavior. It decreases radially outwards from the photosphere, reaching a minimum value of about 4170 K at 515 km of height (Vernazza et al, 1981, [115]). Then, above such height the temperature of the plasma rises monotonically up to 10^4 K at 2000 km.

During the totality of the eclipse, a bright irregular white-light emission appears surrounding the full solar disk (See Figure **A-2**). This is an observational evidence of the *corona*, which is the outer part of the solar atmosphere. It extends from a height of approximately 2500 km above the photosphere to a distance of 100 AU (Aschwanden, Sec. 1.6, [5]; Meyer, Sec. 8.1.3, [89]). Therefore, the corona fills the whole solar system, via a continuous flux of matter known as solar wind, protecting all the planetary system from the interstellar medium. Here, we are interested in the part of the corona which is closest to the Sun, i.e. up to a height of 100 Mm, due to this is the spatial domain of solar flares (Liu et al., 2013, [81]). The temperature in this zone ranging between 8×10^5 K and 10^7 K, the latter just at flaring conditions. For its part the density is pretty low in average, of the order of 10^{-16} g/cm^3 (Eddy & Ise, Ch. 2, [38]).

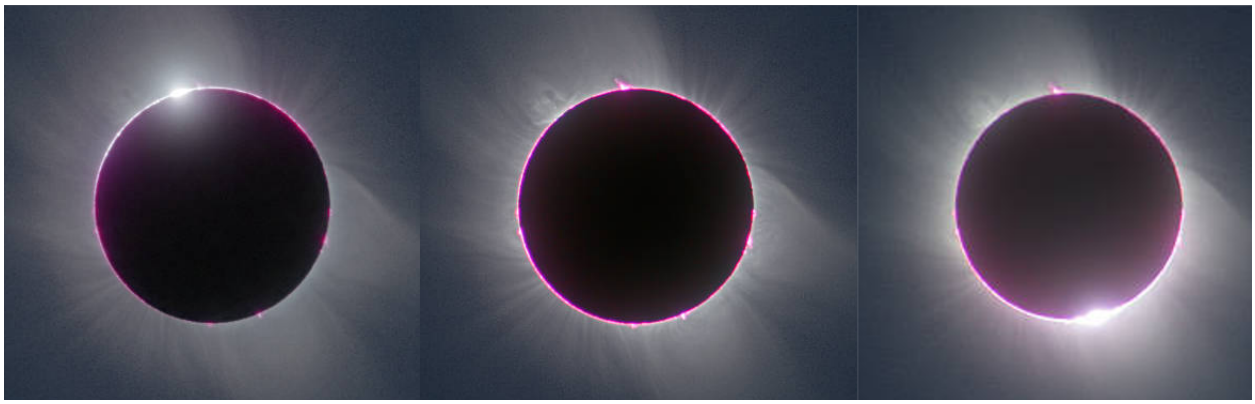

Figure A-2.: Close sequence of the totality during the solar eclipse of April 8, 2005, seen in the middle of the South Pacific Ocean. The surrounding pink emission comes from the chromosphere, while the bright white halo is scattered light produced in the corona. A small portion of the photosphere is also visible as a bright point source in the left and right panels. This effect is known as diamond ring. These pictures were taken by Miloslav Druckmüller [1].

According to the previous descriptions, the temperature increases roughly from 10^4 K at the top of the chromosphere to 10^6 K at the bottom of the corona, i.e. within a narrow spatial region of a few hundred of kilometers. By its part, the density presents also a huge variation within the same region, decreasing six orders of magnitude. The part of the solar atmosphere at which these steeps gradients are located is called *transition zone* (See Figure **A-3**), or *interface region* whether it is considered as one single region together with the chromosphere (De Pontieu et al., 2014, [32]). Through the interface region some physical processes must be building up the energy at the corona, generating the so called *coronal heating*. Also, other mechanisms must supply the outward mass flux that feeds the solar wind (De Pontieu et al., 2014, [32]).

[1]Images downloaded from `http://www.zam.fme.vutbr.cz/~druck/eclipse/Ecl2005d/0-info.htm`

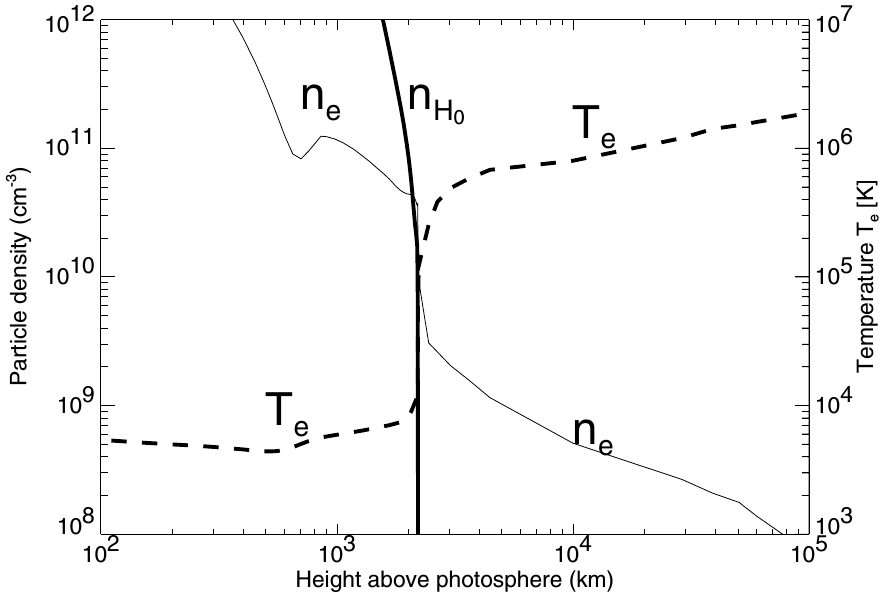

Figure A-3.: Electron temperature and number density above the photosphere according to the model FAL-C (Fontenla et al., 1990, [43]). Around 2000 km the temperature increases while density drops abruptly. Then, scientists assume this height as the location of the transition region. This image was taken from Aschwanden (Sec. 1.6, [5]).

Dynamics

Solar activity manifests itself in a great variety of observational phenomena. The most representative of them are sunspots. These were discovered by Galileo Galilei in 1610 (Golub & Pasachoff, Ch. 2, [50]). A sunspot is a strong concentration of twisted magnetic field that inhibits partially the convection (Cowling, Sec. 4.4, [28]). Hence, the plasma inside a sunspot is colder than the surroundings, which make it looks darker as is seen at Figure **A-4**. Sunspots are the base of closed magnetic structures that extends up to the corona known as *coronal loops* (See Figure **A-4**). The magnetic field strength inside a loop depends on height, it is maximum at the *foopoints* over the photosphere, and minimum at the highest loop point or *apex* (Aschwanden, 2004, [6]).

Sunspots usually emerge in pairs or even in greater groups. Each of such set of sunspots, even those compose by one single spot, is called an *active region*. The lifetime of an active region goes from a few days to a couple of months, depending on its size and morphology. Nonetheless, there are other type of phenomena that happened in shorter timescales. These are eruptive events, like solar flares or Coronal Mass Ejections (CMEs), which are closely related to active regions. When part of the energy stored in a twisted magnetic loop is released, solar flares and/or CMEs can be generated (See section 1.1). The reaction of the medium to these fast and vast energetic releases are usually radio bursts, especially type III, or transient propagating waves such as Moreton waves or *sunquakes* (Hudson, 2011, [59]).

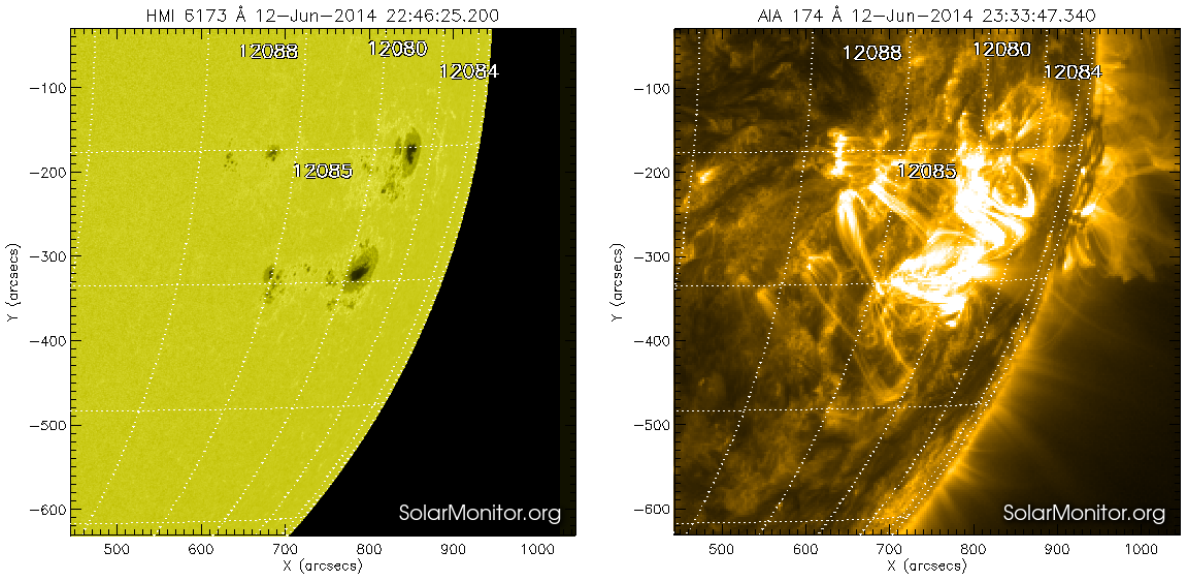

Figure A-4.: Active regions AR 12085 and AR 12080. *Left:* intensity image showing the photosphere. The central spot is AR 12085. *Right*: associated coronal loops to both active regions seen at 171 Å. The images were taken by the instruments HMI and AIA, both on board of the satellite SDO. These were extracted from `solarmonitor.org`.

The Sun presents a periodical cycle of activity of eleven years (See Figure **A-5**). This is evidenced in the appearance and disappearance of sunspots, the occurrence of solar flares and the long-term behavior of the radio flux density at 10.7 cm, among other indicators (Hathaway, 2015, [56]). During the minimum of the cycle the activity is the lowest, there are not sunspots on the solar disk neither eruptive phenomena. At this stage the Sun it is known as *quiet*. On the other hand, when long-live magnetic structures are often seen on the solar surface and the rate of occurrence of eruptive phenomena is high, it is said that the Sun is *active*. Of course, the peak activity of a given cycle occurs at its maximum.

In overall 24 Solar Cycles have been registered to date making use of sunspots counting indicators (See Figure **A-5**). The most famous of them is the Wolf's number, from which other indicators are derived as the International Sunspot Number [2]. The Wolf's number has been computed daily from 1849 to date, while the previous data were extrapolated from the available reports of photospheric observations or geomagnetic activity measurements (Hathaway, 2015, [56]). Currently the 24th Solar Cycle is finishing, whose maximum happened in 2014.

As was mentioned in the previous subsection, the solar interior is opaque to radiation and consequently the information we can acquire from the physical processes involved there is poor. Nonetheless, this situation totally changes for the solar atmosphere. There, the dynamics of

[2]The International Sunspot Number is 0.6 times the Wolf's number `http://www.sidc.be/silso/newdataset`.

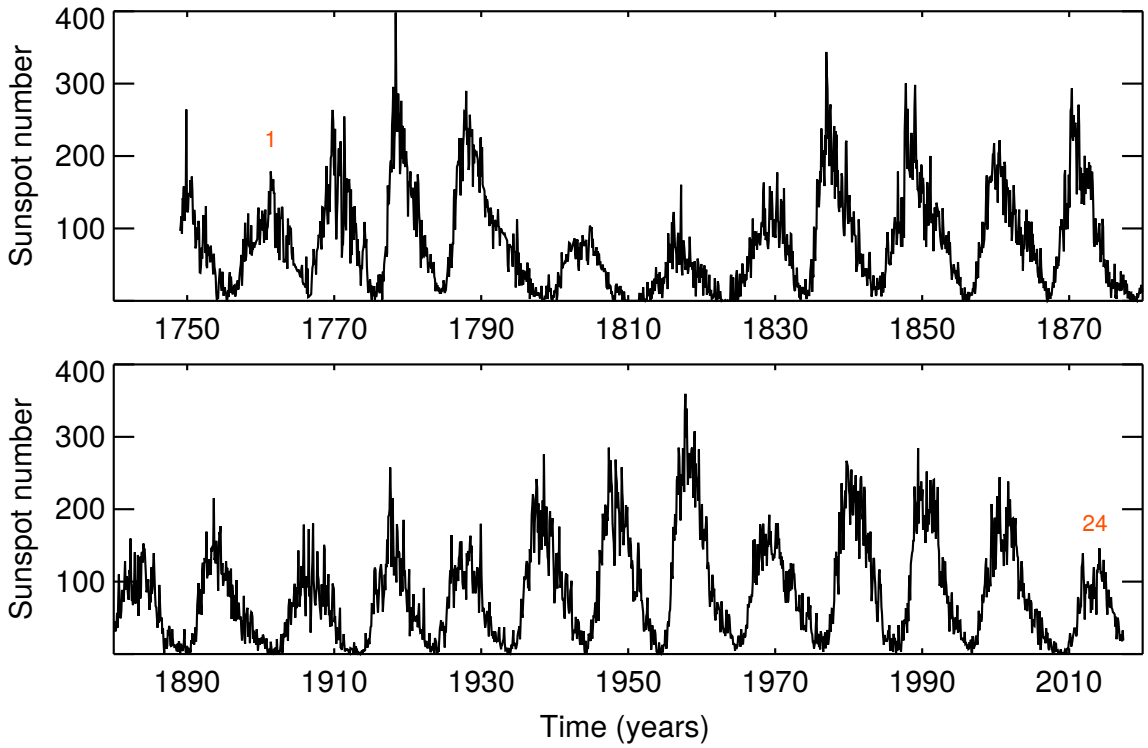

Figure A-5.: Monthly averages of the International Sunspot Number. The dataset spans over all the Solar Cycles. The first and current cycles are labeled with red numbers over their corresponding data. The sunspot data were taken from the World Data Center SILSO, Royal Observatory of Belgium, Brussels [102].

the plasma can be easily observed as this medium is optically thin, i.e. transparent to radiation (See appendix A.2.4). However, its theoretical description is far from being trivial. One common approach used is to treat the plasma as a highly conductive fluid in the presence of an evolving magnetic field. Thus, one suitable theory to describe this system is magnetohydrodynamics (MHD). Here, the behavior of the fluid is derived from equations of mass, momentum and energy conservation, and also from the temporal evolution of the magnetic field (Schnack, Lec. 7, [98]).

One relevant feature to highlight of MHD is the *frozen-flux condition*, which is satisfied only in ideal MHD. The ideal MHD is the most basic description, where all the energy dissipations (viscous, thermal and ohmic) are neglected. The frozen-flux condition states that the magnetic flux through a closed contour co-moving with the fluid is constant (Schnack, Lec. 9, [98]). As consequence, the fluid velocity field and the magnetic field are attached to each other, but only one of them dominates the plasma motion. The β-plasma parameter, $\beta = 8\pi p/B^2$, is commonly used to determine which is the governing field. If $\beta \ll 1$ the fluid is attached to the magnetic field and moves following the field lines. Otherwise, if $\beta \gg 1$, the fluid drags the magnetic field and force it to change according to the fluid flow. The first case occurs in the solar corona, while the second happens in the photosphere (Aschwanden, Sec. 1.8, [5]).

A.2. Physical Processes

One of the foundations of astrophysics are the theories on radiative processes and radiative transfer, which try to figure out how light is created and destroyed, and also how interacts with matter. These processes are so general that can be found at all kind of astrophysical scenarios, including the solar atmosphere at flaring conditions. Here, we will give a brief review about the generation of light via two different mechanisms, namely, bremsstrahlung and gyrosynchrotron. Additionally, the propagation of light through certain medium, and the basics about its states of polarization will be discussed.

A.2.1. Radiation from Accelerated Charged Particles

Consider a charged particle that travels with a constant velocity. We set a reference frame attached to the particle at the initial time of the movement t_0. Suddenly and during a short time interval Δt, the particle is accelerated by a external force towards the same direction of its motion. After that, it keeps moving at the same constant velocity as before.

In such system, the electric field generated by the particle has two different behaviors, seen from the reference frame previously described. During the stages of uniform movement, the electric field is centered on the particle and only has a radial component that follows the well-known Coulomb law. On the other hand, while the particle is accelerated, a tangential component appears in addition to the radial one (Longair, Sec. 6.2.2, [82]). This tangential component is known as the *radiative field* and has two distinctive characteristics. First, its intensity decrease with the inverse of the distance, which make it dominant at the far distances regime over the Coulomb field. Secondly, the radiative field is not conservative, and hence it represents an energy dissipation of the accelerated particle.

These two components of the fields can be found analytically from Maxwell equations. Initially, the equations with sources are written in terms of the scalar ϕ and vector $\vec{A}$ potentials. The resultant differential equations are transformed into wave equations with sources, making use of the Lorenz gauge. The sources are the charge and current densities, but in the case of a single particle they are Dirac deltas of the charge q and the instantaneous particle velocity $\vec{v}$. The solutions of these equations are known as the Liénard-Wiechert potentials, and they represent how ϕ and $\vec{A}$ change in space and evolves with time (Rybicki & Lightman, Sec. 3.1, [97])

$$\phi(\vec{r},t) = \frac{q}{[1-\frac{1}{c}\vec{n}(t_r)\cdot\vec{v}(t_r)]|\vec{r}-\vec{r_0}(t_r)|} \qquad \vec{A}(\vec{r},t) = \frac{q\vec{v}}{c[1-\frac{1}{c}\vec{n}(t_r)\cdot\vec{v}(t_r)]|\vec{r}-\vec{r_0}(t_r)|} \tag{A-1}$$

In these expressions, $R = |\vec{r}-\vec{r_0}(t_r)|$ is the distance between the observer and the particle, and $\vec{n}$ is the unit vector of such distance. Notice that all the quantities on the right-side of equations A-1 are evaluated in a time denoted by t_r, called *retarded time*. The potentials produced by the

charged particle are not detected instantaneously by the observer. This information takes a time R/c to arrive. Hence, at time t the observer sees how were the potentials at a previous time, $t_r = t - R/c$, which is the retarded time. This effect explains how the light we see from our Sun was actually emitted about eight minutes ago, because this is the time required for the light to travel one Astronomical Unit. The corresponding fields derived from the Liénard-Wiechert potentials are (Rybicki & Lightman, Sec. 3.2, [97])

$$\vec{E}(\vec{r},t) = q\left[\frac{(\vec{n}-\vec{\beta})(1-\beta^2)}{\kappa^3 R^2}\right] + \frac{q}{c}\left[\frac{\vec{n}}{\kappa^3 R}\times\left\{(\vec{n}-\vec{\beta})\times\dot{\vec{\beta}}\right\}\right] \qquad \vec{B}(\vec{r},t) = \vec{n}\times\vec{E}(\vec{r},t) \quad \text{(A-2)}$$

Where $\vec{\beta} = \vec{v}/c$ and $\kappa = 1 - \vec{n}(t_r)\cdot\vec{\beta}(t_r)$. In the equation for the electric field, the first term on the right-hand side is the Coulomb or velocity field, while the second one is the radiative field. In the astrophysical context the sources are far away from the observer, so the light we detect is solely produced by the radiative fields, as they decay with a lower power of distance in contrast to the velocity fields. Thus, the total power emitted by a far charged accelerated particle comes from the Poynting flux of its radiative fields and obeys to (Rybicki & Lightman, Sec. 3.3, [97])

$$P = \frac{dW}{dt} = \frac{2q^2\dot{v}^2}{3c^3} \quad \text{(A-3)}$$

This is known as the *Larmor's formula*. This expression holds for a charged particle moving at any speed. In fact, it is a relativistic invariant due to the total power emitted is always the same either measured from the observer frame (Σ) or from the instantaneous frame attached to the particle, usually named proper reference frame (Σ'), i.e. $dW/dt = dW'/dt$. In the case of a relativistic motion, the square of the particle acceleration seen by the observer, according to Lorentz transformations, is $\dot{v}^2 = \gamma^4(\dot{v}_\perp + \gamma^2\dot{v}_{||})$. Moreover, the light emitted by the charged particle has a dipole configuration at its proper reference frame, whose lobes are perpendicular to the instantaneous acceleration of the particle (Rybicki & Lightman, Secs. 3.3 & 4.8, [97]).

A.2.2. Bremsstrahlung

When two different charged particles interact by means of their electric fields, commonly known as Coulomb collisions, they are accelerated and emit light. The radiation generated in this process is known as *bremsstrahlung*. This cannot be produced by a single pair of identical charged particles, as we can always set a reference frame at the center of mass of the system, where the dipole moment, $\Sigma\vec{d_i} = \Sigma q_i\vec{v_i}$, is null and likewise the total power emitted according to the Larmor's formula (see equation A-3).

Consider a collision between a moving electron and a static ion. As the ion is much heavier than the electron, it can be assumed that its state of motion will not be affected by the collision. On the other hand, the electron will suffer a deflection of its trajectory, braking down as it gets close to the ion and emitting light as consequence. In other words, the energy of the electron

decreases via a *free-free* transition. If the electron is highly energetic such deflection will be very small, and after the collision it keeps moving almost in the same direction. This is known as the small-angle scattering regime (Rybicki & Lightman, Sec. 5.1, [97]). Now, we will find the spectrum radiated by a relativistic electron under this regime. The nonrelativistic case can be derived straightforward by neglecting the Lorentz factors.

Let us fix two reference frames to describe the system, the instantaneous proper frame of the electron Σ', and other one centered on the static ion Σ. Both frames have the same axes orientation, with the x-axes being parallel to the direction of motion of the electron. At times $t = t' = 0$, the vertical axes of both frames are aligned, i.e. $x = x' = 0$. However, the frames are separated along z by a distance b, corresponding to the impact parameter of the collision (Longair, Sec. 5.3.1, [82]). The electric field produced by the ion is the responsible of the small deviation in the trajectory of the electron. Seen from Σ it follows the Coulomb law, and at the location of the electron its components are

$$E_x = \frac{Zevt}{[(vt)^2 + b^2]^{3/2}} \qquad E_z = \frac{Zeb}{[(vt)^2 + b^2]^{3/2}} \tag{A-4}$$

Here, Z is the atomic number of the ion and v is the initial speed of the electron. The field seen by the electron in its proper frame is obtained by making the Lorentz transformation of the electromagnetic tensor (Tejeiro, Sec. 8.4, [111]), which yields the following non-null components $E'_x = E_x$, $E'_z = \gamma E_z$, and $B'_y = \gamma\beta E_z$, where $\beta = v/c$. Additionally, the time dilation effect have to be considered, $t = \gamma t'$, for giving all quantities in the frame Σ'.

The electron acceleration has two components, parallel and perpendicular to the direction of motion, $\dot{v}'_{||} = -eE'_x/m_e$ and $\dot{v}'_{\perp} = -eE'_z/m_e$, respectively. Here, we have neglected the acceleration produced by B'_y, as we are only interested in the dynamical effects driven by the electric field. Besides, this contribution becomes irrelevant for nonrelativistic electrons, due to it is scaled by β.

The total energy radiated by the relativistic electron, measured at Σ', can be obtained as the integral of the Larmor's formula (dW'/dt') over time or as the integral of the radiated spectrum ($dW'/d\omega'$) over frequency. Applying the Parseval's theorem (Longair, Sec. 6.2.5, [82]), both integrals relate to each other, and the radiated spectrum can be found straightforward

$$W' = \int_{-\infty}^{\infty} \frac{dW'}{dt'} dt' = \int_{0}^{\infty} \frac{dW'}{d\omega'} d\omega' \qquad \frac{dW'}{d\omega'} = \frac{4e^2}{3c^3} |\dot{v}'(\omega')|^2 \tag{A-5}$$

Here, $\dot{v}'(\omega')$ is the Fourier transform of the electron acceleration, which is defined as

$$\dot{v}'(\omega') = \frac{1}{(2\pi)^{1/2}} \int_{-\infty}^{\infty} \dot{v}'(t') \exp(i\omega' t') dt' \tag{A-6}$$

Computing the Fourier transforms for both components of the electron acceleration, parallel and perpendicular to the direction of motion, and replacing the results in expression A-5 we have

$$\frac{dW'}{d\omega'} = I_0 + I_1 = \frac{8Z^2e^6}{3\pi c^3 m_e^2 v^2}\,\frac{\omega'^2}{\gamma^2 v^2}\left[\frac{1}{\gamma^2}K_0^2\left(\frac{\omega' b}{\gamma v}\right) + K_1^2\left(\frac{\omega' b}{\gamma v}\right)\right] \tag{A-7}$$

Where $dW'/d\omega'$ is the spectrum radiated by the relativistic electron in its proper frame of reference Σ', and K_i is the modified Bessel function of ith order. This spectrum is flat until the cut-off frequency $\omega' = \gamma v/b$, where it falls exponentially as is shown in Figure **A-6**. The main contribution along all frequencies is the radiation derived from the perpendicular component of the acceleration (I_1). By its part, the emission from the parallel component (I_0) has a lower intensity and is located around the cut-off frequency. At higher energies I_1 becomes even more important, due to I_0 decreases γ^{-2} times with respect to I_1 (Longair, Sec. 6.3, [82]).

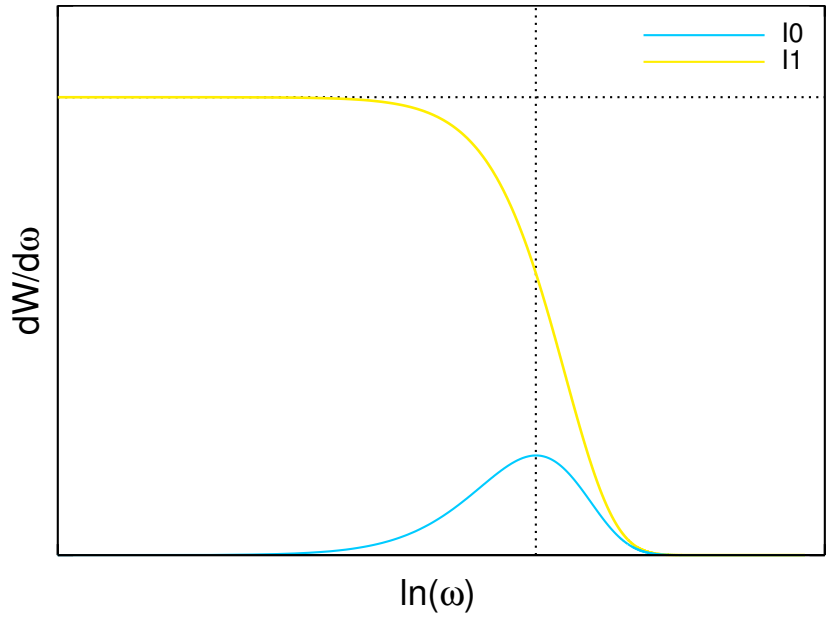

Figure A-6.: Functional form of the spectrum emitted by an electron that collides with an ion. I_0 and I_1 are the radiation coming from the parallel and perpendicular components of the electron acceleration. The horizontal dotted-line marks the flat part of the spectrum at low frequencies, while the vertical dotted-line points out the cut-off frequency $\omega' = \gamma v/b$.

Now, it will be analyzed the energy dissipated by an electron due to the presence of a distribution of ions, whose numerical density is N_i. For simplicity, the nonrelativistic case will be described first, and then the relativistic one. The calculations will be done with the low-frequency part of the spectrum, where it can be considered as constant. Let us take into account all the ions that lie on a cylindrical shell surrounding the moving electron. The radii of the shell ranging among

$[b, b+db]$ and its distance along the x-axis is dx. Using the relation $dt = vdx$ and integrating over the impact parameters, it is obtained the energy loss by the nonrelativistic electron per unit frequency and per unit time (Longair, Sec. 6.4, [82])

$$\frac{dW}{d\omega dt} = \int 2\pi b N_i v \left(\frac{dW}{d\omega}\right) db = \frac{16 Z^2 e^6 N_i}{3c^3 m_e^2 v} \ln\left(\frac{b_{max}}{b_{min}}\right) \tag{A-8}$$

All the terms in the previous expression are known, except by the impact parameter limits. It is necessary to evaluate which are the suitable choices for them. The upper limit is derived from considering the duration of the collision equivalent to the electron orbital period, thus $b_{max} \approx v/\omega_0$ (Longair, Sec. 5.2.1, [82]). For its part, the lower limit can be calculated under two different approaches, from the point of view of classical or quantum mechanics (Longair, Sec. 5.2.2, [82]). The former is based on the principle of energy conservation. The closest impact parameter is achieved when the electron has a frontal collision with the ion, and then all the kinetic energy is transformed into electrostatic potential energy. Additionally, the quantum case is founded on the uncertainty principle. The maximum momentum change in the collision give us a constraint on the minimum approach distance. The expressions for both cases are

$$b^c_{min} = \frac{ze^2}{2m_e v^2} \qquad\qquad b^q_{min} = \frac{\hbar}{2m_e v} \tag{A-9}$$

In the case of a relativistic electron, the power emitted per unit frequency as seen from the frame Σ is the same as such describe in equation A-8. The main difference is the choice of the impact parameter limits. Now, $b_{min} = \hbar/m_e v$, while the upper limit can be considered as the radius of the ion according to the Fermi-Thomas model, $a = 1.4 a_0 Z^{-1/3}$ (Longair, Sec. 6.6, [82]).

In astrophysical contexts, as the flaring plasma in the solar atmosphere, a distribution of electrons is continuously colliding with the ambient ions. Such distribution has two typical forms, thermal or nonthermal. The former follows a Maxwell-Boltzmann distribution of velocities at a given temperature T, while the latter is usually described as a power-law over energy

$$N_e(v)dv = 4\pi v^2 N_e \left(\frac{m_e}{2\pi k_B T}\right)^{3/2} \exp\left(-\frac{m_e v^2}{2k_B T}\right) dv \qquad N(E)dE = CE^{-p}dE \tag{A-10}$$

Here, it has been introduced the Boltzmann constant k_B, the numerical density of electrons N_e, and the power-index p. Integrating the power emitted per unit frequency (equation A-8) over the appropriate distribution of electrons, we get the bremsstrahlung spectral emissivity. In the case of a thermal distribution the spectral emissivity looks like (Longair, Sec. 6.5.1, [82])

$$\frac{dW}{dV d\nu dt} \propto N_i N_e Z^2 T^{-1/2} g(\nu, T) \exp\left(-\frac{h\nu}{k_B T}\right) \tag{A-11}$$

The function $g(\nu, T)$ is called the *Gaunt factor*. The Gaunt factor preserves the information of the impact parameter limits, and it is a slowly-varying function of the frequency of emission and

the temperature of the thermal distribution (Rybicki & Lightman, Sec. 5.1, [97]). The spectral emissivity for nonthermal bremsstrahlung is found in a similar way (See section 2.2), but its functional form follows a power-law shape like the distribution of electrons. The total energy radiated by all the electrons can be found by integrating the spectral emissivity over frequency, and over the volume where the collisions take place. In order to make easier these calculations is convenient to take the average value of the Gaunt factor over frequency, which is typically assumed of the order of unity (Rybicki & Lightman, Sec. 5.2, [97]).

A.2.3. Gyrosynchrotron Radiation

The emission of a charged particle accelerated by a magnetic field receives different names depending on the energy of the particle. The radiation is called cyclotron, gyrosynchrotron and synchrotron, for nonrelativistic, mid-relativistic and relativistic particles, respectively (Dulk, 1985, [36]). However, the physical process is the same at all these regimes. Let us describe the spectrum of a highly relativistic particle and the basic features of the emitted light.

Suppose a particle of charge q moving at velocity v embedded in a region with constant magnetic field along the z-axis. The only force acting on the particle is the magnetic Lorentz force. This force do not exert work on the particle and hence do not change its energy throughout the motion. Therefore, the equation of motion of the charged particle is

$$m\gamma\frac{d\vec{v}}{dt} = \frac{q}{c}\vec{v}\times\vec{B} \tag{A-12}$$

The motion of the particle can be decomposed in the components parallel and perpendicular to the magnetic field direction. The parallel motion is linear, $z = z_0 + v_{||}t$, as it is not affected by the Lorentz force, while the perpendicular motion is circular around the magnetic field lines (Rybicki & Lightman, Sec. 6.1, [97]). The radius and angular *gyrofrequency* of the circular motion have the following form

$$r_g = \frac{\gamma mcv\sin\alpha}{qB} \qquad \omega_g = \frac{qB}{\gamma mc} \tag{A-13}$$

Here α is the *pitch angle*, which is the angle between the particle velocity and the magnetic field. In this case, the acceleration of the particle seen from its proper reference frame (Σ') is the centripetal acceleration of the circular motion $a_c' = \omega_g^2 r_g$, which is always perpendicular to the direction of motion. In the lab frame (Σ), where a stationary observer is located, the square of the centripetal acceleration is $a_c^2 = \gamma^4 a_c^{2\prime}$ (See appendix A.2.1). Then, according to the Larmor's formula A-3 , the total power emitted by the charged particle seen at the lab frame is

$$P = \frac{2q^4B^2\gamma^2v^2\sin^2\alpha}{3c^5m^2} \tag{A-14}$$

In general, the distribution of charged particles is isotropic over the pitch angles, due to the particles are scattered by the irregularities in the magnetic field (Longair, Sec. 7.5, [82]). Taking this into account, the term $\sin^2\alpha$ in the former result is replaced by the average sine square of the pitch angle from an isotropic distribution, which is $\langle \sin^2\alpha \rangle = 2/3$. If the radiating particle is an electron, the formula of the total power emitted can be rewritten by using the definitions of the classical electron radius ($r_e = e^2/m_e c^2$), the Thomson cross section ($\sigma_T = 8\pi r_e^2/3$), the magnetic energy density ($U_B = B^2/8\pi$) and $\beta = v/c$, as appears below

$$P = \frac{4}{3}\sigma_T c \beta^2 \gamma^2 U_B \tag{A-15}$$

In the case of nonrelativistic particles, all the power is emitted at the gyrofrequency ω_g. As the energy of the particle increases, the light is produced also at the harmonics of the gyrofrequency. The higher the harmonic, the less the power emitted at it and the broader is its distribution over frequencies (Longair, Sec. 8.2, [82]). For highly energetic particles all the harmonics join together generating a broad continuum. This last is the case of synchrotron radiation.

Now, let us examine the angular distribution of the radiation emitted by a charged particle moving around a constant magnetic field. Such distribution follows a dipolar pattern, seen at the proper reference frame of the particle, whose lobes open up perpendicularly to the instantaneous acceleration of the particle. For a distant observer at the lab frame, this pattern gets distorted due to the light aberration (Longair, Sec. 8.3, [82])

$$\sin\theta = \frac{\sin\theta'}{\gamma[1+\beta\cos\theta']} \qquad \cos\theta = \frac{\cos\theta' + \beta}{1+\beta\cos\theta'} \tag{A-16}$$

In the extreme case of an ultra-relativistic particle ($v \approx c$), this phenomenon confines the lobe of radiation inside a small-aperture angle, $\theta \sim 1/\gamma$. This is known as *beaming effect* and is a general feature of the radiation emitted by highly energetic particles, independently of the radiative mechanism involved. One consequence of the beaming effect for gyrosynchrotron or synchrotron radiation, is that the pulses of the electric field coming from the charged particle have less duration seen at the lab frame. Therefore, the frequency at which most of the light is emitted becomes higher than the nonrelativistic gyrofrequency (Longair, Sec. 8.3, [82]). This new characteristic frequency can be derived for an ultra-relativistic particle, i.e. in the case of synchrotron radiation, from the duration of its associated electric field pulses (Δt).

An observer only sees the synchrotron radiation when the beam of light points towards her/him. This happens while the particle moves between two specific points of the circular trajectory, P_1 and P_2, which subtend a segment of arc $s = r_g\theta$. Due to the beaming effect θ is very small, thus the linear distance between P_1 and P_2 is almost equal to s. The duration of the electric field pulse corresponds to the time delay between the radiation emitted at P_1 and P_2

$$\Delta t = \frac{L}{v}\left[1 - \frac{v}{c}\right] \tag{A-17}$$

Where v is the particle speed. The factor in the square brackets tends to $1/2\gamma^2$, due to it was assumed that $v \approx c$ (Longair, Sec. 8.3, [82]). Taking into account the beaming effect $\theta \sim 1/\gamma$, and that the particle speed is the product of the the angular gyrofrequency ω_g and the radius of the circular motion r_g, then the duration of the electric field pulse is straightforward calculated. The inverse of the pulse duration give us an approximation of the dominant frequency of the emission. This is called the *critical frequency* (ω_c) and it is γ^3 times higher than the gyrofrequency

$$\Delta t \approx \frac{1}{2\gamma^3 \omega_g} \qquad \omega_c \approx \frac{1}{\Delta t} \tag{A-18}$$

So far, it has been discussed the most relevant characteristics of this radiation mechanism, but it has not presented yet the form of the synchrotron spectrum. Its derivation is far from being trivial, as it is long and complex. For this reason, it will not be given a summary of such calculation process here. Instead, only the result will be written down and its main properties will be discussed. The energy emitted by a relativistic charged particle per unit frequency per unit time via synchrotron radiation is (Rybicki & Lightman, Sec. 6.4, [97])

$$\frac{dW}{d\omega dt} = \frac{\sqrt{3} q^3 B \sin\alpha}{2\pi mc} \, F(x) \tag{A-19}$$

From the previous result, we see that the shape of the spectrum is given solely by the form of $F(x)$, as the other quantities are physical constants or fixed parameters of the system. This function is defined in terms of modified Bessel function of order $5/3$, and it is evaluated over the parameter $x = \omega/\omega_c$. The exact expressions for $F(x)$ and the critical frequency ω_c are

$$F(x) = x \int_x^\infty K_{5/3}(z) dz \qquad \omega_c = \frac{3}{2}\gamma^3 \omega_g \sin\alpha \tag{A-20}$$

The synchrotron spectrum is very broad over frequencies, in contrast to the nonrelativistic emission that is confined at the gyrofrequency (See Figure **A-7**). Although ω_c is the characteristic frequency of this radiation mechanism, the maximum of the emission is not located at it, instead it is at $0.29\omega_c$. At low energies the spectrum decays as $\omega^{1/3}$, while at high energies it decreases as the product of an exponential and the square root of ω (Rybicki & Lightman, Sec. 6.4, [97]).

Lastly, the synchrotron spectrum coming from a nonthermal distribution of charged particles is derived. The distribution of particles is assumed to be a power-law over the Lorentz factors, i.e. $N(\gamma)d\gamma = C\gamma^{-p}d\gamma$, similar to such described in equation A-10. Then, the spectral emissivity will be the integral over the Lorentz factors of the product between the power spectrum ($dW/d\omega dt$) times the distribution of particles, which yields

$$\frac{dW}{dV d\omega dt} = \frac{\sqrt{3} q^3 C B \sin\alpha}{2\pi mc(p+1)} \Gamma\left(\frac{p}{4} + \frac{19}{12}\right) \Gamma\left(\frac{p}{4} - \frac{1}{12}\right) \left(\frac{mc\omega}{3qB\sin\alpha}\right)^{-s} \tag{A-21}$$

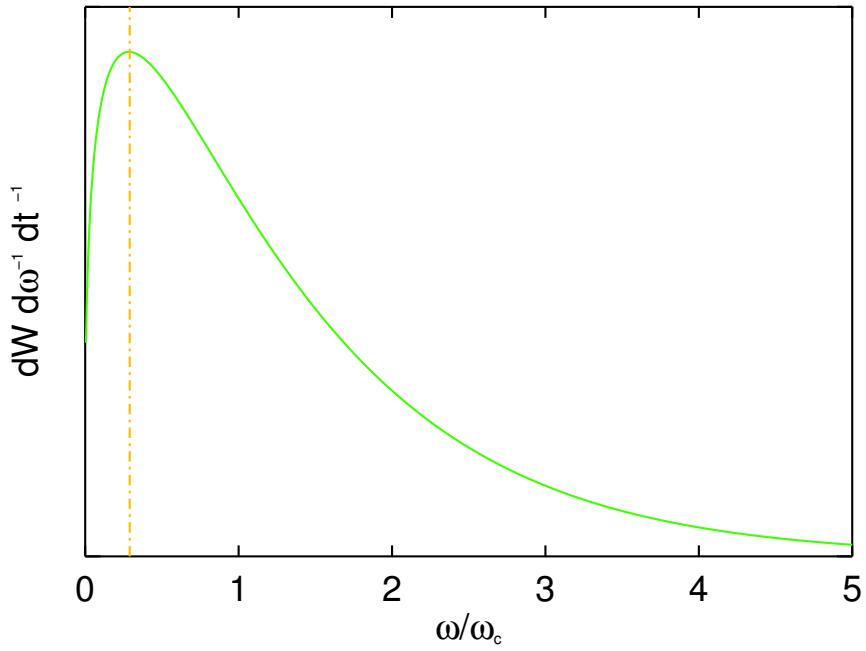

Figure A-7.: Functional form of the synchrotron spectrum for a single relativistic particle. The vertical dotted line marks the frequency with the highest emission $0.29\omega_c$.

Thus, the spectral emissivity is a power-law of ω, whose characteristic index is s. This spectral index depends on the power-index p of the distribution of particles as $s = -(p-1)/2$ (Rybicki & Lightman, Sec. 6.3, [97]). Then, from the observed light generated by the synchrotron radiation process it is possible to acquire information about the distribution of the emitting particles.

A.2.4. Basics on Radiative Transfer

Light can be generated via different radiation mechanisms as those exposed in the previous two appendices (A.2.2 & A.2.3). However, this light must travel through a medium before it reaches us. The medium blocks or allows the pass of light, depending on its composition and on the wavelength of the propagating radiation. In this appendix, it will be seen the basics of such interaction between light and matter, often called in the textbooks as *radiative transfer*.

The building block of the one-dimensional radiative transfer theory is the definition of the *pencil of radiation*. This is the light emitted by a radiating source in a narrow range of frequencies $d\nu$, during a short time interval dt, that passes across an area perpendicular to the direction of light propagation $dA_\perp$, which subtends a differential of solid angle $d\Omega$. The total energy emitted by the pencil of radiation is the product of all the small quantities described before and the *specific intensity* I_ν (Chandrasekhar, Sec. 5.1.a, [23])

$$dW = I_\nu d\nu dt dA_\perp d\Omega \tag{A-22}$$

Most of the observables detected with photometric techniques comes from the specific intensity. For example, the integral of I_ν over all directions gives as result the monochromatic flux F_ν. Furthermore, if the contributions from all frequencies are added up the net flux F is found. Finally, integrating over a closed surface containing the source the total power emitted, named luminosity L in the case of a star, is obtained. All these quantities have been extensively measured for any kind of astronomical objects and represent the core of photometry.

Now, it will be examined what happens when light interacts with matter along its propagation path. Suppose a beam of light that travels a distance dx across a medium with mass density ρ. The specific intensity that comes out is less than the initial, due to the medium absorbs part of the incoming light. The more intense is the beam, the bigger is the energy loss. Then, the differential decrease in the specific intensity dI_ν is proportional to I_ν, ρ, dx, and to an *absorption coefficient* κ_ν, whose units are cm^2 g^{-1} (Chandrasekhar, Sec. 5.1.g, [23]).

On the other hand, the medium can produce light by two different ways. First, an atom can spontaneously emit a photon of energy $h\nu_{nm}$, because it passes from an excited state n to another less energetic state m. Secondly, if the incoming light has frequency ν_{nm}, the beam can induce the generation of a photon with the same frequency. Both effects are included in the *emission coefficient* j_ν that have units of erg s^{-1} Hz^{-1} g^{-1} ster^{-1}. The total increase in the specific intensity is the product of ρ, j_ν and dx (Chandrasekhar, Sec. 5.1.f, [23]). Joining both effects, absorption and emission, we find the *equation of radiative transfer*

$$\frac{dI_\nu}{dx} = \rho j_\nu - \rho \kappa_\nu I_\nu \tag{A-23}$$

The equation of radiative transfer tells us how much change the specific intensity while light travels a distance dx through certain medium. Thus, I_ν increases or decreases depending whether emission or absorption processes are dominant at the frequency ν, respectively. Light can also be scattered by the atoms of the medium, which introduces another loss term in equation A-23.

Another key feature of the radiative transfer is the optical depth, $\tau_\nu = \kappa_\nu \rho dx$, which tell us how strong is the effect of light absorption. If $\tau_\nu > 1$ matter inhibit the propagation of light and radiation cannot escape from the source. In the other extreme limit, $\tau_\nu < 1$, the mean free path of the light is larger than the typical size of the source, and therefore light can escape. The medium is called *optically thick* in the former case, and *optically thin* in the latter (Rybicki & Lightman, Sec. 1.4, [97]). Putting the equation of radiative transfer in terms of the optical depth, and defining the ratio between the emission and absorption coefficients as the source function, $S_\nu = j_\nu / \kappa_\nu$, it is obtained

$$\frac{dI_\nu}{d\tau_\nu} = S_\nu - I_\nu \tag{A-24}$$

There is a particular and important solution of the previous radiative transfer equation when the medium where light propagates is in Local Thermodynamic Equilibrium (LTE), i.e. the temperature is the same throughout a local region and varies slowly from one slab or shell to another. In such case, absorption and emission effects compensate each other, and hence there is not net change in the specific intensity $dI_\nu/d\tau_\nu = 0$ (Chandrasekhar, Sec. 5.2, [23]). Under this condition, the specific intensity turns out to be equal to the source function. In a LTE medium the latter corresponds to the blackbody spectrum of radiation $B_\nu(T)$

$$B_\nu(T) = \frac{2h\nu^3}{c^2}\frac{1}{\exp(h\nu/k_BT) - 1} \tag{A-25}$$

In a LTE medium all radiation mechanisms converge to the blackbody spectrum at low frequencies, because at this regime the physical processes that produce light become also effective to absorb it (Longair, Sec. 6.5.2, [82]). In consequence, each radiative process has its own absorption coefficient κ_ν associated to it. This can be derived from the solution of the equation of radiative transfer in a LTE medium, i.e. $B_\nu(T)$, together with the relation between the emission coefficient j_ν and the spectral emissivity ϵ_ν of the corresponding radiative process (Rybicki & Lightman, Sec. 1.4, [97])

$$B_\nu(T) = \frac{j_\nu}{\kappa_\nu} \qquad \epsilon_\nu = \int \rho j_\nu d\Omega \tag{A-26}$$

Where ϵ_ν is the energy emitted per unit time per unit frequency and per unit volume by the radiative mechanism of interest. In particular, the spectral emissivities for bremsstrahlung and gyrosynchrotron radiation are found in appendices A.2.2 and A.2.3.

A.2.5. Polarization of Light

In the previous appendix (A.2.4) it was seen the radiative transfer equation for the specific intensity I_ν and when light can propagate or not through a medium. Nevertheless, a full 3D description of the radiative transfer must include information on the state of polarization of light as well as on its specific intensity. For this reason, let us discuss the concept of polarization of light. We start finding the latter for a single plane electromagnetic wave, because the pencil of radiation or beam of light is just the composition of multiple plane monochromatic electromagnetic waves.

By definition, in a single plane electromagnetic wave the electric field oscillates with a fixed temporal frequency ω and a fixed spatial frequency k. Such oscillation takes place in a plane perpendicular to the direction of light propagation $\vec{k}$. By its part, the magnetic field also oscillates with the same frequencies but in a plane normal to $\vec{E}$ and $\vec{k}$, as $\vec{B} = \vec{k} \times \vec{E}$. Now, suppose that light propagates towards positive z. Then, the electric field oscillates in the plane xy, and its most general functional form is (Shu, Ch. 12, [101])

$$\vec{E}(\vec{r}, t) = \left[\hat{x}\epsilon_x e^{i\phi_x} + \hat{y}\epsilon_y e^{i\phi_y}\right] e^{i(kz-\omega t)} \tag{A-27}$$

Where ϵ_n and ϕ_n are the magnitude and phase of the nth electric field component. In general, the oscillation of the electric field describes an elliptical trajectory in the plane xy. Nevertheless, there are two special of cases which deserve our attention. When both phases are equal the oscillation becomes linear, and thus the plane wave is said to be *linearly polarized*. On the other hand, when the electric field magnitudes are the same $\epsilon = \epsilon_x = \epsilon_y$ and the phase difference fulfill the condition $\phi_x - \phi_y = \pm\pi/2$, then the trajectory in the plane xy is a circle of radius ϵ. If the difference between the phases is $\pi/2$, the electric field sweep the circle counterclockwise and the plane wave is *right circularly polarized*. In the other case, $\phi_x - \phi_y = -\pi/2$, the electric field rotates clockwise and the plane wave is *left circularly polarized* (Bastian, Sec. 4.2.4, [9]).

We have seen that a plane electromagnetic wave is fully described by the real parameters ϵ_x, ϵ_y, ϕ_x and ϕ_y, if the direction of propagation $\vec{k}$, and the frequencies ω and k are known. However, handle this set of parameters can be tricky due to the difficulty of measuring them directly from observations. Therefore, another set of parameters is defined, in terms of the magnitudes and phases of the electric field, which are easier to measure by using just combinations of retardation phase plates and linear polarizers (Berry et al., 1977, [13]). These are the well-known *Stokes parameters* (Bastian, Sec. 4.2.4, [9])

$$\begin{aligned} I &= \epsilon_x^2 + \epsilon_y^2 & V &= 2\epsilon_x\epsilon_y \sin(\phi_x - \phi_y) \\ Q &= \epsilon_x^2 - \epsilon_y^2 & U &= 2\epsilon_x\epsilon_y \cos(\phi_x - \phi_y) \end{aligned} \tag{A-28}$$

Here, I is the total intensity which is the integral of I_ν over all frequencies. A plane wave is always fully polarized and its Stokes parameters fulfill the relation $I^2 = Q^2 + U^2 + V^2$. However, the light coming from astronomical sources is detected by our instruments during a finite time interval dt and inside a narrow range of frequencies or bandwidth $d\nu$. So, it contains a lot of plane waves, with different values of ϵ_n, ϕ_n, ω and k, that have oscillated many times during dt. Therefore, the Stokes parameters measured from astronomical objects are in fact averaged values over time and frequency of such composition of plane waves. Due to this reason, the observed Stokes parameters are independent of each other, and now they hold the expression $\bar{I}^2 \geq \bar{Q}^2 + \bar{U}^2 + \bar{V}^2$ (Shu, 1991, [101]). The deviation from the equality is attributed to unpolarized waves. Thus, the observed light has two components: polarized and unpolarized. In order to know how much light is polarized the total polarized intensity is divided over the total observed intensity. This quantity is called the *degree of polarization* (Rybicki & Lightman, Sec. 2.4, [97])

$$\Pi = \frac{I_p}{\bar{I}} = \frac{\sqrt{\bar{Q}^2 + \bar{U}^2 + \bar{V}^2}}{\bar{I}} \tag{A-29}$$

In the case of linear polarization V is null, and the resulting expression from equation A-29 is known as the linear degree of polarization ρ_l. By its part the circular degree of polarization is defined independently from Π, and obeys to $\rho_c = V/I$. These particular degrees of polarization are important for the radiative processes processes reviewed before (See appendices A.2.2

& A.2.3). Bremsstrahlung emission coming from a nonthermal distribution of particles can be partially linearly polarized, but it is not circularly polarized at all. The opposite case occurs with gyrosynchrotron radiation, as the circular polarization is the relevant one in this case (Bastian, Sec. 4.2.4, [9]).

Detailed information on radiative transfer and polarization of light can be found in the book *Radiative Transfer* by S. Chandrasekhar (1960, [24]).

A.3. Results from the Work Sample

In this Appendix are shown the results obtained from the quantities described in Chapter 4. The information of the impulsive phase duration measured from the nonthermal X-ray lightcurve (IPD), the rise time of the most prominent nonthermal X-ray emission (RT), the number of peaks detected within the impulsive phase duration or multiplicity (MU), and the linear Pearson correlation coefficient associated to the Neupert effect (NE) are found in Tables **A-2**, **A-3**, **A-4**, **A-5**, and **A-6** for the lightcurves LC1, LC2, LC3, LC4, and LC5, respectively. The units of IPD and RT are seconds. The other quantities are dimensionless.

On the other hand, the average values of the spectral indexes in HXR and microwaves, i.e. φ and s, are shown in Tables **A-7** and **A-10**, respectively. Their corresponding evolutionary patterns (EP) can be found in Tables **A-8** and **A-11**. Finally, the impulsive phase duration in microwaves (IPDM) is presented in Table **A-9**. The units of IPDM are seconds. All the other quantities mentioned throughout this document, like the impulsivity parameter (IP), the trapping indicator (TI), and the power-index of the distribution of electrons (p), can be inferred from the ones that are listed in this Appendix.

ID	IPD	RT	MU	NE	ID	IPD	RT	MU	NE	ID	IPD	RT	MU	NE
1	80	64	2	0.51	36	296	16	3	0.81	71	824	232	3	0.16
2	448	40	3	0.78	37	624	128	2	0.59	72	1248	896	9	0.69
3	56	16	1	0.33	38	664	256	4	0.68	73	360	104	3	0.72
4	40	16	1	0.72	39	176	48	1	0.45	74	336	64	3	0.62
5	368	192	3	0.27	40	240	144	1	0.67	75	216	64	2	0.71
6	168	48	1	0.78	41	0	0	0	0.10	76	176	48	1	0.60
7	80	32	1	0.37	42	312	144	3	0.76	77	136	16	1	0.43
8	1536	216	10	0.22	43	168	56	2	0.62	78	152	56	3	0.74
9	248	120	2	0.57	44	200	72	2	0.22	79	240	80	2	0.33
10	392	152	4	0.04	45	232	136	1	0.50	80	128	56	1	0.60
11	568	352	5	0.62	46	104	56	1	0.68	81	304	16	4	0.53
12	312	96	3	0.08	47	160	120	3	-0.00	82	136	8	1	0.45
13	56	24	1	0.35	48	280	160	4	0.52	83	192	56	1	0.71
14	656	104	6	0.68	49	160	72	1	0.82	84	528	296	5	0.59
15	216	120	1	0.09	50	168	88	1	0.33	85	224	32	2	0.64
16	160	88	1	0.86	51	40	16	1	0.76	86	0	0	0	0.23
17	208	144	1	0.11	52	0	0	0	0.10	87	232	64	1	0.00
18	64	40	1	0.89	53	168	96	1	0.16	88	136	48	1	-0.01
19	0	0	0	0.72	54	592	264	5	0.60	89	120	56	1	0.17
20	336	72	2	0.50	55	528	128	1	-0.29	90	296	64	2	0.51
21	312	112	3	0.36	56	488	160	4	0.58	91	400	192	3	0.52
22	88	16	1	0.66	57	456	232	2	0.41	92	264	128	4	0.76
23	64	40	2	0.46	58	200	112	1	0.60	93	312	160	2	0.60
24	360	88	1	0.69	59	680	224	5	-0.29	94	136	40	1	0.71
25	488	376	5	0.83	60	112	64	1	0.82	95	120	32	1	0.65
26	0	0	0	0.58	61	144	88	1	0.04	96	376	176	2	0.00
27	184	88	1	0.50	62	408	200	4	0.37	97	72	48	1	0.28
28	240	64	1	0.59	63	368	240	3	0.68	98	528	424	7	0.74
29	48	16	1	0.50	64	112	32	1	0.74	99	240	120	2	0.64
30	248	152	3	0.49	65	816	168	3	0.60	100	368	232	4	0.63
31	144	88	1	0.81	66	344	56	1	0.41	101	232	200	1	0.29
32	56	24	1	0.75	67	544	232	6	-0.18	102	0	0	0	0.36
33	176	72	1	0.82	68	56	24	1	-0.01	103	616	144	5	0.84
34	1576	576	5	0.22	69	776	168	6	0.21	104	112	40	1	0.59
35	328	176	1	0.80	70	144	88	2	0.71	105	144	56	2	0.76

Table A-2.: Impulsive phase duration (IPD), rise time of the most prominent peak (RT), multiplicity (MU), and correlation coefficient of the Neupert effect measured from LC1.

ID	IPD	RT	MU	NE	ID	IPD	RT	MU	NE	ID	IPD	RT	MU	NE
106	464	248	2	0.75	141	104	24	1	0.74	176	72	8	1	0.21
107	360	208	1	0.53	142	72	24	1	0.67	177	552	192	5	-0.03
108	656	456	2	0.37	143	920	584	5	0.43	178	120	40	1	0.79
109	136	112	1	0.49	144	360	104	1	0.85	179	472	128	4	0.14
110	200	72	2	0.33	145	144	120	1	0.00	180	56	16	1	0.62
111	448	48	5	0.52	146	296	80	2	0.09	181	152	16	3	0.00
112	392	152	3	0.69	147	240	96	1	0.58	182	216	96	3	0.20
113	792	376	5	0.71	148	40	8	1	0.76	183	72	16	1	0.70
114	176	24	1	0.71	149	1552	168	10	0.01	184	88	8	1	0.81
115	400	56	2	-0.04	150	120	24	2	0.42	185	800	216	5	-0.04
116	640	48	1	0.14	151	488	392	4	0.18	186	200	104	2	0.16
117	320	232	3	0.68	152	72	40	1	0.61	187	128	56	1	0.48
118	600	176	2	0.74	153	288	72	3	0.38	188	352	104	3	0.01
119	232	96	3	0.75	154	128	16	2	0.60	189	160	96	1	0.49
120	776	320	2	0.62	155	480	160	4	0.48	190	104	64	1	0.53
121	72	24	1	0.84	156	192	104	2	0.84	191	192	40	2	0.44
122	104	56	1	0.49	157	1456	840	4	0.07	192	352	24	3	0.00
123	824	160	1	0.82	158	72	48	2	0.70	193	648	312	5	0.00
124	184	40	2	0.76	159	1056	552	8	0.26	194	264	112	3	0.42
125	216	120	2	0.79	160	496	192	3	0.12	195	112	48	1	0.73
126	648	152	3	0.75	161	184	24	1	0.69	196	192	40	1	0.42
127	88	64	1	0.28	162	1112	512	7	0.08	197	160	72	1	0.60
128	120	80	1	0.48	163	112	16	1	0.80	198	120	40	1	0.15
129	272	168	4	0.55	164	632	120	1	0.09	199	688	232	5	0.43
130	72	24	1	0.03	165	104	40	2	0.81	200	208	80	2	0.52
131	136	64	1	0.67	166	440	120	4	0.00	201	168	120	4	0.42
132	120	64	2	-0.09	167	240	48	2	0.21	202	224	48	2	0.58
133	264	120	1	0.07	168	416	72	3	0.48	203	168	64	1	0.77
134	264	88	2	0.65	169	1000	424	6	0.45	204	1480	296	4	-0.03
135	208	32	1	0.75	170	184	96	1	0.40	205	312	56	1	0.17
136	112	48	1	0.79	171	608	120	1	0.45	206	1592	528	10	0.00
137	296	32	2	0.78	172	1304	200	3	-0.03	207	728	280	5	0.00
138	0	0	0	-0.09	173	200	64	2	0.24	208	136	32	2	0.37
139	496	232	5	0.39	174	152	88	1	0.15					
140	80	32	1	0.09	175	96	56	1	0.86					

Table A-2.: Impulsive phase duration (IPD), rise time of the most prominent peak (RT), multiplicity (MU), and correlation coefficient of the Neupert effect measured from LC1.

ID	IPD	RT	MU	NE	ID	IPD	RT	MU	NE	ID	IPD	RT	MU	NE
1	80	64	2	0.49	36	232	16	2	0.67	71	848	264	3	0.23
2	344	32	2	0.79	37	608	552	3	0.58	72	848	360	5	0.68
3	48	16	1	0.46	38	208	96	1	0.57	73	264	32	3	0.72
4	40	16	1	0.70	39	152	8	1	0.62	74	320	64	2	0.60
5	0	0	0	0.18	40	216	144	2	0.83	75	112	64	1	0.69
6	160	40	1	0.77	41	0	0	0	0.10	76	72	40	1	0.51
7	72	24	1	0.34	42	312	144	2	0.75	77	64	8	1	0.32
8	0	0	0	-0.19	43	104	24	1	0.74	78	152	56	2	0.72
9	208	88	2	0.75	44	152	72	1	0.47	79	200	80	2	0.26
10	224	80	2	0.53	45	192	104	1	0.47	80	136	64	1	0.66
11	296	152	2	0.72	46	88	56	1	0.71	81	288	16	3	0.72
12	200	80	2	0.14	47	152	120	3	-0.01	82	128	8	1	0.42
13	56	24	1	0.46	48	280	160	1	0.57	83	144	48	1	0.64
14	888	152	6	0.46	49	144	56	1	0.84	84	520	304	4	0.59
15	176	104	1	0.32	50	112	8	1	0.39	85	72	32	1	0.50
16	160	88	1	0.86	51	40	16	1	0.78	86	192	112	2	0.35
17	184	144	1	0.26	52	0	0	0	0.07	87	592	288	2	0.00
18	64	48	1	0.88	53	152	80	2	0.26	88	104	40	1	-0.01
19	128	96	1	0.75	54	504	208	3	0.60	89	112	56	1	0.15
20	0	0	0	0.36	55	560	200	2	-0.16	90	120	48	1	0.50
21	152	112	2	0.53	56	464	152	4	0.57	91	384	192	4	0.57
22	32	8	1	0.68	57	456	264	2	0.43	92	264	128	3	0.78
23	56	40	1	0.44	58	192	104	1	0.73	93	320	144	1	0.59
24	224	64	1	0.65	59	688	232	5	-0.19	94	240	96	2	0.87
25	472	376	5	0.81	60	112	64	1	0.81	95	200	32	1	0.69
26	0	0	0	0.51	61	136	88	1	-0.01	96	0	0	0	-0.00
27	144	88	1	0.47	62	0	0	0	0.06	97	72	48	1	0.26
28	152	64	1	0.53	63	328	200	2	0.68	98	528	424	6	0.75
29	48	16	1	0.40	64	64	24	1	0.71	99	240	120	2	0.63
30	264	152	2	0.53	65	0	0	0	0.57	100	144	24	2	0.59
31	160	88	1	0.83	66	360	80	2	0.46	101	104	72	1	0.34
32	56	24	1	0.73	67	232	64	1	0.03	102	0	0	0	0.62
33	136	72	1	0.79	68	56	24	1	0.09	103	0	0	0	0.57
34	288	136	1	0.41	69	280	208	1	0.45	104	72	40	1	0.47
35	304	144	1	0.82	70	136	88	2	0.68	105	128	56	1	0.77

Table A-3.: Impulsive phase duration (IPD), rise time of the most prominent peak (RT), multiplicity (MU), and correlation coefficient of the Neupert effect measured from LC2.

ID	IPD	RT	MU	NE	ID	IPD	RT	MU	NE	ID	IPD	RT	MU	NE
106	448	248	3	0.75	141	160	48	1	0.84	176	80	16	1	0.41
107	336	200	1	0.47	142	88	24	1	0.71	177	0	0	0	0.08
108	600	448	2	0.34	143	696	552	4	0.43	178	128	48	1	0.79
109	136	112	1	0.56	144	264	96	1	0.87	179	0	0	0	0.22
110	192	64	2	0.38	145	144	120	1	0.00	180	56	16	1	0.63
111	104	48	1	0.36	146	216	72	1	0.23	181	176	72	2	0.00
112	368	152	2	0.67	147	144	40	2	0.30	182	0	0	0	0.16
113	776	376	5	0.74	148	48	16	1	0.77	183	56	16	1	0.66
114	328	168	2	0.72	149	0	0	0	-0.10	184	88	8	1	0.82
115	400	56	2	-0.06	150	120	24	2	0.43	185	0	0	0	-0.05
116	368	16	2	0.38	151	528	304	5	0.73	186	176	16	2	0.56
117	416	256	4	0.71	152	72	32	1	0.60	187	112	56	1	0.46
118	512	88	4	0.70	153	176	64	2	0.79	188	280	88	2	0.26
119	248	96	2	0.77	154	96	16	1	0.60	189	48	8	1	0.39
120	1016	560	2	0.63	155	336	144	3	0.42	190	64	24	1	0.52
121	88	24	1	0.84	156	184	72	1	0.83	191	200	48	2	0.44
122	96	64	1	0.52	157	224	72	1	0.12	192	752	336	7	0.00
123	856	168	2	0.84	158	64	48	1	0.67	193	656	312	6	0.00
124	144	24	2	0.64	159	560	224	5	0.27	194	256	112	3	0.61
125	160	104	2	0.75	160	424	144	4	0.61	195	112	56	1	0.66
126	184	48	2	0.79	161	176	24	1	0.76	196	136	32	1	0.39
127	88	64	1	0.56	162	632	360	8	0.06	197	64	32	1	0.54
128	96	56	1	0.72	163	64	16	1	0.83	198	224	72	1	0.13
129	248	168	3	0.60	164	0	0	0	0.03	199	464	88	5	0.42
130	0	0	0	0.01	165	104	40	1	0.80	200	232	80	3	0.64
131	128	64	1	0.68	166	432	112	4	0.00	201	160	112	2	0.47
132	96	64	2	0.15	167	104	16	1	0.19	202	216	32	2	0.53
133	264	112	1	0.06	168	144	72	1	0.64	203	160	64	1	0.77
134	216	88	2	0.61	169	504	248	5	0.45	204	1160	176	4	-0.00
135	184	32	1	0.71	170	184	96	1	0.43	205	88	56	1	0.12
136	80	32	1	0.78	171	264	88	1	0.25	206	1440	776	11	0.00
137	272	32	3	0.76	172	0	0	0	0.13	207	656	272	6	0.00
138	296	216	3	0.42	173	128	8	1	0.24	208	176	40	2	0.38
139	440	360	5	0.54	174	144	88	1	0.18					
140	144	56	2	0.82	175	96	56	1	0.87					

Table A-3.: Impulsive phase duration (IPD), rise time of the most prominent peak (RT), multiplicity (MU), and correlation coefficient of the Neupert effect measured from LC2.

ID	IPD	RT	MU	NE	ID	IPD	RT	MU	NE	ID	IPD	RT	MU	NE
1	80	64	2	0.56	36	264	16	3	0.77	71	952	336	3	0.29
2	352	32	2	0.79	37	608	552	2	0.60	72	1240	896	4	0.69
3	48	16	1	0.48	38	376	248	1	0.58	73	272	40	4	0.72
4	40	16	1	0.71	39	160	48	1	0.67	74	328	64	2	0.61
5	456	192	2	0.33	40	224	144	2	0.82	75	128	48	1	0.70
6	160	40	1	0.77	41	0	0	0	0.11	76	96	48	1	0.54
7	80	32	1	0.35	42	312	144	3	0.70	77	72	16	1	0.35
8	0	0	0	-0.17	43	120	24	1	0.74	78	152	56	2	0.74
9	224	96	2	0.73	44	160	72	2	0.38	79	200	80	2	0.30
10	552	152	2	0.61	45	240	144	1	0.54	80	136	64	1	0.67
11	456	232	2	0.73	46	104	56	1	0.69	81	320	200	3	0.80
12	248	96	2	0.15	47	144	112	2	-0.00	82	136	8	1	0.45
13	152	24	2	0.56	48	296	160	1	0.62	83	160	48	1	0.68
14	888	144	5	0.42	49	144	56	1	0.83	84	544	304	4	0.63
15	176	104	1	0.14	50	176	72	1	0.45	85	80	32	1	0.53
16	168	88	1	0.86	51	48	16	1	0.79	86	208	120	2	0.46
17	192	136	2	0.27	52	0	0	0	0.09	87	632	288	2	0.00
18	64	40	1	0.89	53	272	176	2	0.35	88	128	40	1	-0.01
19	72	40	1	0.73	54	512	208	5	0.59	89	112	48	1	0.24
20	120	32	1	0.43	55	576	160	2	-0.16	90	288	56	2	0.51
21	224	112	1	0.53	56	488	160	4	0.60	91	472	272	4	0.60
22	80	8	2	0.57	57	456	264	1	0.40	92	272	128	3	0.77
23	64	40	1	0.47	58	192	112	1	0.72	93	328	144	1	0.64
24	256	64	1	0.66	59	680	224	4	-0.20	94	256	88	1	0.83
25	472	376	4	0.82	60	168	64	1	0.82	95	248	40	2	0.73
26	0	0	0	0.69	61	136	88	1	-0.01	96	320	96	2	0.03
27	192	104	1	0.50	62	0	0	0	0.25	97	72	48	1	0.34
28	160	64	1	0.55	63	392	240	2	0.70	98	712	552	5	0.75
29	48	16	1	0.47	64	112	32	1	0.73	99	272	128	2	0.67
30	248	136	2	0.59	65	656	136	3	0.65	100	288	152	4	0.64
31	160	96	1	0.83	66	376	96	2	0.49	101	104	72	1	0.32
32	56	24	1	0.76	67	272	80	1	0.07	102	304	88	4	0.80
33	176	72	1	0.82	68	72	24	1	-0.10	103	464	160	5	0.74
34	720	432	4	0.43	69	424	272	2	0.54	104	88	40	1	0.60
35	328	176	1	0.80	70	144	88	2	0.72	105	192	64	1	0.78

Table A-4.: Impulsive phase duration (IPD), rise time of the most prominent peak (RT), multiplicity (MU), and correlation coefficient of the Neupert effect measured from LC3.

ID	IPD	RT	MU	NE	ID	IPD	RT	MU	NE	ID	IPD	RT	MU	NE
106	536	264	3	0.76	141	224	80	1	0.84	176	88	24	1	0.36
107	360	208	1	0.52	142	280	32	2	0.73	177	624	192	3	0.08
108	648	456	2	0.37	143	680	536	5	0.50	178	144	40	2	0.72
109	248	112	1	0.61	144	400	104	1	0.85	179	112	56	1	0.32
110	208	72	3	0.47	145	264	120	1	0.01	180	56	16	1	0.67
111	112	48	1	0.43	146	288	80	1	0.24	181	168	64	2	0.00
112	368	152	2	0.68	147	168	40	2	0.35	182	296	64	3	-0.09
113	816	376	4	0.75	148	48	16	1	0.76	183	56	16	1	0.67
114	336	168	2	0.72	149	0	0	0	-0.10	184	104	16	1	0.81
115	760	72	6	-0.15	150	120	24	2	0.40	185	672	232	5	-0.04
116	88	16	1	0.25	151	624	304	3	0.64	186	176	16	2	0.56
117	512	256	4	0.71	152	72	32	1	0.62	187	136	56	1	0.42
118	592	168	3	0.72	153	176	64	2	0.76	188	256	72	3	0.26
119	288	96	2	0.75	154	120	16	1	0.63	189	48	8	1	0.42
120	1848	640	4	0.63	155	432	160	3	0.44	190	80	48	1	0.53
121	96	24	1	0.82	156	208	96	1	0.84	191	224	88	2	0.31
122	72	48	1	0.53	157	224	72	2	0.28	192	664	336	3	0.00
123	976	168	2	0.88	158	64	48	1	0.69	193	752	312	6	0.00
124	176	40	2	0.72	159	968	272	8	0.33	194	264	112	3	0.51
125	176	120	2	0.79	160	440	160	4	0.59	195	112	48	1	0.72
126	208	56	3	0.80	161	184	24	1	0.75	196	144	40	1	0.49
127	200	72	2	0.55	162	616	232	4	0.12	197	96	40	1	0.59
128	120	80	1	0.72	163	72	16	1	0.84	198	120	40	1	0.15
129	272	168	3	0.70	164	360	96	1	0.11	199	696	232	5	0.49
130	72	24	1	0.04	165	128	48	1	0.80	200	240	80	2	0.66
131	128	48	1	0.68	166	432	120	4	0.00	201	208	120	3	0.53
132	120	64	2	0.13	167	232	40	2	0.23	202	224	40	2	0.55
133	280	112	1	0.07	168	152	72	1	0.63	203	208	64	1	0.74
134	240	88	2	0.63	169	1048	472	7	0.51	204	1072	144	3	0.06
135	192	32	1	0.72	170	216	96	1	0.47	205	104	56	1	0.14
136	112	40	1	0.79	171	608	72	1	0.35	206	1536	528	10	0.00
137	296	32	2	0.78	172	88	40	1	0.02	207	664	280	6	0.00
138	1056	224	6	0.44	173	208	80	2	0.35	208	152	32	2	0.37
139	128	56	1	0.51	174	144	88	1	0.30					
140	152	56	2	0.84	175	96	56	1	0.86					

Table A-4.: Impulsive phase duration (IPD), rise time of the most prominent peak (RT), multiplicity (MU), and correlation coefficient of the Neupert effect measured from LC3.

ID	IPD	RT	MU	NE	ID	IPD	RT	MU	NE	ID	IPD	RT	MU	NE
1	0	0	0	0.05	36	376	280	2	0.77	71	824	224	4	0.09
2	224	88	1	0.75	37	600	128	2	0.55	72	512	232	1	0.39
3	0	0	0	0.06	38	200	80	1	0.50	73	152	16	2	0.55
4	64	32	1	0.50	39	176	128	1	0.18	74	168	104	1	0.60
5	0	0	0	-0.04	40	80	48	1	0.69	75	112	64	1	0.65
6	104	32	1	0.68	41	0	0	0	0.00	76	0	0	0	0.30
7	64	16	1	0.29	42	112	64	1	0.76	77	64	16	1	0.24
8	0	0	0	-0.29	43	112	48	1	0.54	78	136	40	2	0.63
9	184	104	1	0.68	44	400	192	2	0.11	79	152	56	2	0.36
10	0	0	0	-0.19	45	0	0	0	0.00	80	144	64	1	0.40
11	672	400	4	0.48	46	64	24	1	0.33	81	0	0	0	0.05
12	272	96	1	-0.13	47	56	24	1	0.00	82	80	8	1	0.35
13	0	0	0	0.34	48	368	208	3	0.13	83	144	48	1	0.53
14	592	88	6	0.76	49	272	152	2	0.77	84	376	184	2	0.40
15	160	104	1	0.33	50	56	8	1	0.30	85	64	32	1	0.16
16	200	136	1	0.82	51	32	16	1	0.72	86	0	0	0	0.20
17	104	40	1	0.31	52	0	0	0	0.08	87	0	0	0	0.00
18	64	8	1	0.35	53	0	0	0	0.09	88	72	48	1	0.00
19	0	0	0	0.31	54	816	256	3	0.50	89	232	208	1	-0.19
20	0	0	0	0.21	55	528	128	1	-0.35	90	744	544	5	0.51
21	80	16	2	0.20	56	264	144	3	0.37	91	328	96	3	0.38
22	0	0	0	0.16	57	456	232	2	0.37	92	256	104	3	0.73
23	72	48	1	0.39	58	160	96	1	0.02	93	64	24	1	0.47
24	200	48	1	0.59	59	680	248	3	-0.33	94	136	40	1	0.68
25	0	0	0	0.29	60	0	0	0	0.41	95	104	24	1	0.58
26	0	0	0	0.52	61	144	88	1	-0.04	96	0	0	0	-0.11
27	136	72	1	0.09	62	0	0	0	-0.07	97	216	120	1	0.08
28	80	24	1	0.19	63	0	0	0	0.47	98	160	128	2	0.49
29	32	16	1	0.27	64	48	24	1	0.64	99	112	96	2	0.07
30	0	0	0	0.16	65	0	0	0	0.36	100	488	232	4	0.45
31	0	0	0	0.11	66	288	48	1	0.26	101	0	0	0	0.26
32	56	8	1	0.45	67	528	224	3	-0.36	102	0	0	0	0.13
33	0	0	0	0.60	68	0	0	0	-0.03	103	0	0	0	0.10
34	0	0	0	0.43	69	752	144	5	0.09	104	0	0	0	0.06
35	0	0	0	0.38	70	0	0	0	0.49	105	0	0	0	0.26

Table A-5.: Impulsive phase duration (IPD), rise time of the most prominent peak (RT), multiplicity (MU), and correlation coefficient of the Neupert effect measured from LC4.

ID	IPD	RT	MU	NE	ID	IPD	RT	MU	NE	ID	IPD	RT	MU	NE
106	0	0	0	0.22	141	96	16	1	0.68	176	48	8	1	0.03
107	376	240	2	0.49	142	136	56	1	0.57	177	448	72	4	0.35
108	552	416	2	0.27	143	0	0	0	0.31	178	56	40	1	0.77
109	120	104	1	0.33	144	232	80	1	0.86	179	0	0	0	0.01
110	0	0	0	0.16	145	1024	112	1	-0.03	180	40	16	1	0.54
111	80	24	1	0.31	146	1608	800	14	-0.13	181	0	0	0	0.00
112	360	144	1	0.60	147	88	40	1	0.11	182	0	0	0	0.05
113	792	376	5	0.65	148	56	16	1	0.77	183	56	16	1	0.45
114	168	24	2	0.67	149	0	0	0	-0.20	184	80	8	1	0.75
115	0	0	0	-0.02	150	96	56	1	0.28	185	0	0	0	-0.05
116	224	16	1	0.33	151	368	280	3	0.11	186	0	0	0	0.10
117	248	184	2	0.52	152	64	48	1	0.38	187	0	0	0	-0.00
118	480	112	3	0.51	153	160	112	2	0.84	188	0	0	0	0.05
119	88	16	1	0.53	154	0	0	0	0.09	189	184	136	1	0.31
120	672	224	2	0.60	155	952	496	5	0.10	190	216	144	2	0.50
121	48	24	1	0.77	156	80	56	2	0.73	191	80	16	1	0.04
122	0	0	0	0.43	157	1184	568	5	-0.18	192	352	16	4	0.00
123	408	128	1	0.69	158	64	48	1	0.57	193	440	136	4	0.00
124	80	24	1	0.18	159	1032	464	4	0.15	194	224	16	1	0.41
125	136	72	2	0.66	160	344	64	4	0.49	195	72	32	1	0.22
126	184	48	3	0.78	161	88	24	1	0.72	196	0	0	0	0.01
127	96	64	1	0.04	162	0	0	0	0.11	197	0	0	0	0.30
128	88	56	1	0.09	163	56	16	1	0.82	198	0	0	0	0.08
129	312	296	2	-0.08	164	0	0	0	-0.00	199	512	176	4	0.34
130	0	0	0	-0.01	165	88	48	1	0.82	200	0	0	0	0.10
131	136	64	1	0.66	166	256	72	2	-0.00	201	0	0	0	0.06
132	440	208	1	-0.38	167	0	0	0	-0.00	202	136	48	1	0.41
133	248	112	1	0.06	168	48	24	1	0.56	203	160	48	1	0.76
134	176	80	2	0.59	169	296	72	2	-0.13	204	0	0	0	-0.11
135	192	40	2	0.74	170	0	0	0	0.30	205	0	0	0	-0.00
136	0	0	0	0.50	171	0	0	0	-0.02	206	0	0	0	0.00
137	136	24	1	0.49	172	0	0	0	0.08	207	0	0	0	0.00
138	0	0	0	-0.09	173	0	0	0	0.15	208	56	24	1	0.39
139	504	248	4	0.28	174	0	0	0	-0.00					
140	0	0	0	0.02	175	96	56	1	0.86					

Table A-5.: Impulsive phase duration (IPD), rise time of the most prominent peak (RT), multiplicity (MU), and correlation coefficient of the Neupert effect measured from LC4.

ID	IPD	RT	MU	NE	ID	IPD	RT	MU	NE	ID	IPD	RT	MU	NE
1	80	64	2	0.43	36	264	16	2	0.77	71	824	232	3	0.17
2	344	32	2	0.79	37	608	128	3	0.57	72	904	600	1	0.67
3	72	16	1	0.25	38	208	88	1	0.54	73	256	24	3	0.71
4	40	16	1	0.70	39	176	48	1	0.53	74	320	64	2	0.60
5	0	0	0	0.13	40	208	136	1	0.80	75	112	64	1	0.69
6	144	40	1	0.74	41	0	0	0	0.09	76	80	48	1	0.47
7	64	16	1	0.32	42	304	144	2	0.77	77	56	8	1	0.30
8	0	0	0	-0.30	43	88	24	1	0.72	78	152	56	2	0.70
9	200	96	2	0.75	44	144	24	2	0.41	79	184	64	2	0.27
10	384	144	2	-0.03	45	200	104	1	0.38	80	136	64	1	0.63
11	568	352	3	0.63	46	80	56	1	0.66	81	304	16	3	0.53
12	272	96	1	-0.01	47	152	120	3	-0.00	82	112	8	1	0.40
13	56	24	1	0.41	48	280	160	1	0.52	83	144	48	1	0.61
14	880	144	7	0.58	49	208	120	1	0.82	84	536	296	4	0.55
15	168	104	1	0.34	50	112	8	1	0.35	85	72	32	1	0.47
16	144	80	1	0.85	51	48	16	1	0.75	86	192	112	1	0.32
17	184	144	1	0.33	52	0	0	0	0.08	87	592	288	2	0.00
18	64	48	1	0.86	53	168	96	2	0.21	88	104	40	1	-0.00
19	208	120	1	0.74	54	616	264	3	0.61	89	120	56	1	0.03
20	128	48	1	0.33	55	528	128	1	-0.32	90	504	376	3	0.50
21	152	112	4	0.45	56	480	344	4	0.52	91	400	192	4	0.52
22	32	8	1	0.70	57	456	240	1	0.39	92	256	104	3	0.77
23	56	40	1	0.42	58	192	112	1	0.48	93	320	152	1	0.60
24	216	56	1	0.64	59	680	248	5	-0.31	94	240	96	2	0.87
25	472	368	6	0.77	60	112	64	1	0.81	95	120	32	1	0.66
26	0	0	0	0.56	61	144	88	1	-0.04	96	0	0	0	-0.02
27	64	24	1	0.46	62	0	0	0	-0.01	97	72	48	1	0.21
28	136	64	1	0.46	63	336	208	2	0.68	98	528	424	7	0.74
29	40	16	1	0.36	64	50	24	1	0.69	99	160	120	2	0.51
30	248	152	2	0.49	65	928	280	6	0.54	100	352	232	4	0.57
31	160	88	1	0.82	66	336	56	1	0.37	101	104	72	1	0.33
32	56	24	1	0.69	67	536	224	3	-0.28	102	0	0	0	0.47
33	128	72	1	0.77	68	136	104	1	0.01	103	480	224	2	0.40
34	1064	400	4	0.45	69	760	168	5	0.15	104	96	40	1	0.37
35	304	120	1	0.82	70	136	88	2	0.64	105	144	56	1	0.75

Table A-6.: Impulsive phase duration (IPD), rise time of the most prominent peak (RT), multiplicity (MU), and correlation coefficient of the Neupert effect measured from LC5.

ID	IPD	RT	MU	NE	ID	IPD	RT	MU	NE	ID	IPD	RT	MU	NE
106	416	248	2	0.73	141	144	24	1	0.82	176	64	16	1	0.18
107	376	232	2	0.50	142	80	24	1	0.68	177	560	72	2	0.27
108	592	440	2	0.32	143	944	608	5	0.39	178	120	40	1	0.80
109	136	112	1	0.51	144	264	96	1	0.87	179	472	128	4	0.16
110	200	72	2	0.33	145	144	120	1	0.00	180	56	16	1	0.60
111	88	32	1	0.34	146	296	80	1	0.15	181	160	64	2	0.00
112	368	152	2	0.65	147	144	40	2	0.27	182	216	104	4	0.18
113	792	376	6	0.71	148	40	8	1	0.77	183	56	16	1	0.62
114	312	160	2	0.72	149	1416	224	10	-0.17	184	88	8	1	0.81
115	400	56	2	-0.04	150	64	24	1	0.44	185	848	488	4	-0.05
116	288	16	2	0.36	151	520	304	4	0.38	186	184	40	2	0.54
117	320	232	3	0.68	152	72	40	1	0.57	187	112	32	1	0.43
118	488	88	3	0.66	153	168	112	2	0.82	188	184	64	2	0.29
119	240	96	3	0.76	154	120	16	1	0.46	189	40	8	1	0.37
120	784	328	2	0.62	155	336	96	3	0.33	190	104	64	1	0.52
121	88	24	1	0.85	156	168	72	1	0.83	191	144	16	2	0.39
122	104	64	1	0.50	157	1416	832	4	-0.04	192	448	112	3	0.00
123	510	160	1	0.79	158	64	48	1	0.67	193	648	312	6	0.00
124	136	24	2	0.58	159	1080	576	7	0.24	194	264	112	4	0.59
125	160	104	2	0.74	160	368	88	4	0.57	195	112	56	1	0.59
126	184	48	3	0.79	161	112	24	1	0.76	196	152	32	1	0.28
127	88	64	1	0.21	162	1112	512	7	0.08	197	48	24	1	0.49
128	88	56	1	0.33	163	64	16	1	0.83	198	120	40	1	0.12
129	280	176	3	0.44	164	0	0	0	0.02	199	536	88	5	0.40
130	0	0	0	-0.00	165	104	40	1	0.81	200	216	80	2	0.58
131	128	64	1	0.69	166	424	112	4	0.00	201	168	120	3	0.39
132	480	176	1	-0.26	167	104	16	1	0.15	202	216	128	2	0.51
133	264	120	1	0.06	168	64	32	1	0.63	203	160	64	1	0.77
134	200	80	2	0.61	169	512	248	5	0.36	204	1568	832	4	-0.06
135	192	32	1	0.72	170	184	96	1	0.39	205	1096	672	3	0.07
136	80	32	1	0.77	171	264	80	1	0.20	206	1592	784	10	0.00
137	272	32	3	0.75	172	360	208	4	0.16	207	856	200	6	0.00
138	680	280	1	0.10	173	200	64	2	0.22	208	56	24	1	0.41
139	144	72	1	0.51	174	1184	192	2	0.12					
140	144	56	1	0.70	175	96	56	1	0.87					

Table A-6.: Impulsive phase duration (IPD), rise time of the most prominent peak (RT), multiplicity (MU), and correlation coefficient of the Neupert effect measured from LC5.

ID	φ	ID	φ	ID	φ	ID	φ	ID	φ	ID	φ
1	7.25	36	2.98	71	6.83	106	7.55	141	5.15	176	5.93
2	5.18	37	1.75	72	5.38	107	1.74	142	5.97	177	1.76
3	4.46	38	2.99	73	5.38	108	3.83	143	2.87	178	5.89
4	5.52	39	5.61	74	4.91	109	3.88	144	4.89	179	7.18
5	7.32	40	4.36	75	4.68	110	5.64	145	3.52	180	5.65
6	3.52	41	7.04	76	6.53	111	3.57	146	6.82	181	6.56
7	3.24	42	6.02	77	5.41	112	2.77	147	5.87	182	7.50
8	4.60	43	5.18	78	4.32	113	3.38	148	2.07	183	4.51
9	5.79	44	5.24	79	4.63	114	5.10	149	2.38	184	3.55
10	5.83	45	5.36	80	3.50	115	6.48	150	4.62	185	4.53
11	2.80	46	5.98	81	7.65	116	4.59	151	4.86	186	5.66
12	1.74	47	5.39	82	3.54	117	3.02	152	6.43	187	6.76
13	8.32	48	6.57	83	4.35	118	4.00	153	3.29	188	5.37
14	2.89	49	2.46	84	5.45	119	6.20	154	5.36	189	4.97
15	3.78	50	3.75	85	6.47	120	2.81	155	4.06	190	2.35
16	4.49	51	4.30	86	4.13	121	6.70	156	7.41	191	5.74
17	5.26	52	8.53	87	8.25	122	4.22	157	6.81	192	4.64
18	6.60	53	7.04	88	6.82	123	2.55	158	5.56	193	3.44
19	6.75	54	4.50	89	6.66	124	5.85	159	3.70	194	4.87
20	6.98	55	1.76	90	4.80	125	5.15	160	3.45	195	5.14
21	6.36	56	4.57	91	3.90	126	4.33	161	4.49	196	4.96
22	7.18	57	1.77	92	3.35	127	5.26	162	4.66	197	6.61
23	4.29	58	5.24	93	5.68	128	3.86	163	5.65	198	4.91
24	4.27	59	1.74	94	5.84	129	7.05	164	6.82	199	4.54
25	5.54	60	6.81	95	4.62	130	7.91	165	3.96	200	7.46
26	5.21	61	1.74	96	7.38	131	3.11	166	5.26	201	6.82
27	6.01	62	5.00	97	4.07	132	4.30	167	6.87	202	4.52
28	4.18	63	7.08	98	6.40	133	1.75	168	5.17	203	4.88
29	5.19	64	5.18	99	5.75	134	3.77	169	6.04	204	5.92
30	7.33	65	6.93	100	5.59	135	3.58	170	5.67	205	3.66
31	7.51	66	2.52	101	5.75	136	6.21	171	5.40	206	2.62
32	5.54	67	1.75	102	8.27	137	4.50	172	9.16	207	6.38
33	7.46	68	7.83	103	2.65	138	8.11	173	6.64	208	4.07
34	4.14	69	6.46	104	6.75	139	5.85	174	4.10		
35	6.43	70	5.54	105	6.90	140	6.06	175	3.75		

Table A-7.: Average values of the spectral index in HXR (φ).

ID	EP	ID	EP	ID	EP	ID	EP	ID	EP	ID	EP
1	HHS	36	HHS	71	MAS	106	SHS	141	IRR	176	SHS
2	MAS	37	FLA	72	IRR	107	FLA	142	MAS	177	FLA
3	MAS	38	SHS	73	IRR	108	IRR	143	HSH	178	MAS
4	IRR	39	MAS	74	SHS	109	MAS	144	MAS	179	IRR
5	IRR	40	SHS	75	MAS	110	SHH	145	SHH	180	MAS
6	SHS	41	IRR	76	MAS	111	MAS	146	FLA	181	MAS
7	IRR	42	MAS	77	MAS	112	SHS	147	MAS	182	IRR
8	IRR	43	MAS	78	MAS	113	SHS	148	MAS	183	MAS
9	MAS	44	MAS	79	SHH	114	IRR	149	IRR	184	MAS
10	SHS	45	SHS	80	FLA	115	MAS	150	MAS	185	MAS
11	IRR	46	MAS	81	HHS	116	MAS	151	SHH	186	MAS
12	FLA	47	MAS	82	SHS	117	SHS	152	MAS	187	HHS
13	MAS	48	FLA	83	MAS	118	FLA	153	SHH	188	MAS
14	FLA	49	MAS	84	SHH	119	SHS	154	HHS	189	MAS
15	MAS	50	MAS	85	MAS	120	FLA	155	IRR	190	HSH
16	MAS	51	MAS	86	MAS	121	MAS	156	MAS	191	MAS
17	MAS	52	MAS	87	IRR	122	SHS	157	MAS	192	SHH
18	IRR	53	SHS	88	MAS	123	SHS	158	MAS	193	FLA
19	MAS	54	FLA	89	IRR	124	MAS	159	SHH	194	IRR
20	SHS	55	FLA	90	IRR	125	SHS	160	SHS	195	MAS
21	MAS	56	SHH	91	IRR	126	MAS	161	MAS	196	MAS
22	MAS	57	FLA	92	MAS	127	MAS	162	IRR	197	MAS
23	SHS	58	MAS	93	MAS	128	IRR	163	MAS	198	IRR
24	SHS	59	FLA	94	MAS	129	HHS	164	MAS	199	SHS
25	FLA	60	HHS	95	MAS	130	IRR	165	MAS	200	HHS
26	IRR	61	FLA	96	IRR	131	MAS	166	SHS	201	HHS
27	MAS	62	IRR	97	MAS	132	IRR	167	MAS	202	MAS
28	HHS	63	SHS	98	MAS	133	FLA	168	MAS	203	MAS
29	HHS	64	SHS	99	IRR	134	MAS	169	MAS	204	IRR
30	HSH	65	IRR	100	IRR	135	MAS	170	MAS	205	MAS
31	MAS	66	FLA	101	MAS	136	SHH	171	MAS	206	IRR
32	IRR	67	FLA	102	IRR	137	FLA	172	IRR	207	IRR
33	MAS	68	HHS	103	FLA	138	MAS	173	IRR	208	IRR
34	SHS	69	SHS	104	HHS	139	MAS	174	HSH		
35	FLA	70	MAS	105	IRR	140	MAS	175	MAS		

Table A-8.: Evolutionary patterns in HXR for the whole work sample.

ID	IPDM	ID	IPDM	ID	IPDM	ID	IPDM	ID	IPDM	ID	IPDM
1	183	36	373	71	1199	106	140	141	150	176	126
2	452	37	644	72	778	107	337	142	98	177	568
3	139	38	318	73	437	108	703	143	620	178	83
4	148	39	287	74	371	109	131	144	329	179	78
5	1389	40	159	75	110	110	207	145	104	180	52
6	211	41	0	76	136	111	173	146	543	181	65
7	111	42	225	77	107	112	793	147	0	182	344
8	0	43	193	78	183	113	1037	148	97	183	102
9	276	44	131	79	369	114	325	149	208	184	134
10	384	45	189	80	417	115	45	150	148	185	128
11	209	46	100	81	298	116	1491	151	528	186	308
12	348	47	213	82	167	117	397	152	198	187	91
13	185	48	323	83	182	118	0	153	0	188	272
14	627	49	162	84	508	119	239	154	140	189	44
15	360	50	70	85	114	120	720	155	348	190	82
16	267	51	188	86	0	121	171	156	371	191	181
17	223	52	0	87	177	122	0	157	513	192	380
18	129	53	179	88	97	123	706	158	74	193	899
19	127	54	482	89	0	124	193	159	2679	194	0
20	0	55	1077	90	121	125	208	160	433	195	0
21	119	56	521	91	556	126	250	161	102	196	105
22	204	57	184	92	297	127	110	162	129	197	186
23	78	58	254	93	106	128	147	163	95	198	299
24	847	59	585	94	237	129	122	164	0	199	113
25	239	60	101	95	196	130	0	165	180	200	126
26	0	61	292	96	0	131	131	166	626	201	83
27	100	62	0	97	138	132	152	167	0	202	246
28	0	63	152	98	735	133	553	168	64	203	183
29	52	64	55	99	179	134	214	169	594	204	111
30	106	65	142	100	0	135	281	170	199	205	29
31	119	66	823	101	180	136	63	171	313	206	0
32	74	67	300	102	0	137	317	172	547	207	599
33	144	68	63	103	0	138	1772	173	0	208	95
34	239	69	289	104	110	139	341	174	0		
35	311	70	152	105	183	140	170	175	201		

Table A-9.: Impulsive phase durations in microwaves (IPDM) for the events of the work sample.

ID	s	ID	s	ID	s	ID	s	ID	s	ID	s
1	1.49	36	-0.3	71	0.70	106	0.66	141	0.23	176	0.77
2	1.48	37	0.80	72	0.49	107	0.59	142	0.62	177	0.00
3	0.71	38	0.94	73	1.65	108	1.14	143	0.60	178	0.79
4	1.06	39	0.87	74	1.33	109	1.50	144	1.09	179	0.31
5	0.71	40	1.11	75	0.64	110	1.41	145	0.41	180	0.92
6	0.70	41	1.58	76	0.73	111	0.59	146	0.79	181	1.88
7	0.94	42	0.12	77	0.64	112	0.96	147	0.00	182	0.97
8	0.00	43	0.85	78	0.80	113	1.37	148	1.01	183	0.37
9	1.39	44	0.00	79	1.22	114	0.78	149	2.16	184	0.00
10	1.10	45	1.08	80	0.55	115	0.63	150	0.64	185	0.37
11	0.65	46	0.78	81	0.00	116	1.19	151	0.16	186	0.86
12	0.18	47	0.25	82	1.11	117	0.20	152	1.44	187	0.00
13	0.60	48	1.38	83	1.39	118	0.00	153	0.34	188	0.32
14	0.28	49	-0.0	84	0.99	119	2.30	154	0.67	189	0.41
15	0.60	50	0.38	85	0.00	120	1.30	155	1.47	190	0.64
16	1.04	51	0.68	86	0.00	121	1.47	156	1.14	191	0.55
17	0.54	52	0.02	87	0.68	122	0.02	157	0.26	192	0.95
18	1.84	53	1.06	88	1.09	123	0.01	158	-0.0	193	1.37
19	2.13	54	0.75	89	0.35	124	0.00	159	0.58	194	0.00
20	0.54	55	0.00	90	0.96	125	0.39	160	0.65	195	0.00
21	0.88	56	0.61	91	1.04	126	0.81	161	0.59	196	2.16
22	2.56	57	-3.0	92	0.95	127	0.36	162	1.60	197	0.65
23	0.84	58	1.12	93	0.34	128	0.20	163	0.78	198	1.18
24	1.60	59	-0.0	94	0.64	129	0.00	164	0.00	199	1.05
25	0.67	60	1.06	95	0.32	130	1.01	165	1.10	200	0.28
26	0.58	61	1.77	96	0.00	131	0.40	166	0.90	201	0.16
27	0.43	62	1.19	97	1.18	132	0.09	167	0.07	202	0.00
28	0.00	63	1.59	98	0.66	133	1.03	168	1.21	203	0.37
29	-0.0	64	1.58	99	1.35	134	1.01	169	0.96	204	1.17
30	0.00	65	0.37	100	0.00	135	0.34	170	0.75	205	0.94
31	1.26	66	0.81	101	0.54	136	1.12	171	0.88	206	0.32
32	0.92	67	0.08	102	0.67	137	0.99	172	0.32	207	0.08
33	0.57	68	1.38	103	0.23	138	0.71	173	8.64	208	0.68
34	0.26	69	1.42	104	0.00	139	0.63	174	5.89		
35	1.44	70	2.07	105	1.52	140	0.57	175	0.73		

Table A-10.: Average values of the spectral index in microwaves (s).

ID	EP	ID	EP	ID	EP	ID	EP	ID	EP	ID	EP
1	IRR	36	FDF	71	HSH	106	SHH	141	HHS	176	IRR
2	PNC	37	IRR	72	PNC	107	PNC	142	IRR	177	PNC
3	PNC	38	HSH	73	PNC	108	FLA	143	IRR	178	HSH
4	IRR	39	PNC	74	HHS	109	PNC	144	SHH	179	IRR
5	PNC	40	SHH	75	SHH	110	IRR	145	HSH	180	RR
6	HSH	41	PNC	76	IRR	111	IRR	146	HSH	181	PNC
7	HSH	42	IRR	77	HSH	112	PNC	147	PNC	182	IRR
8	PNC	43	SHH	78	PNC	113	HSH	148	FDF	183	FLA
9	PNC	44	FDF	79	PNC	114	SHH	149	PNC	184	PNC
10	IRR	45	HSH	80	HSH	115	HHS	150	IRR	185	IRR
11	IRR	46	IRR	81	PNC	116	PNC	151	HSH	186	IRR
12	FDF	47	PNC	82	SHH	117	FDF	152	IRR	187	FDF
13	PNC	48	PNC	83	PNC	118	PNC	153	HSH	188	PNC
14	SHS	49	SHH	84	HSH	119	SHS	154	PNC	189	HSH
15	SHH	50	IRR	85	FDF	120	IRR	155	PNC	190	IRR
16	SHH	51	HSH	86	PNC	121	SHS	156	SHH	191	HSH
17	HSH	52	PNC	87	PNC	122	FDF	157	FDF	192	PNC
18	SHH	53	IRR	88	IRR	123	PNC	158	HSH	193	PNC
19	HSH	54	SHH	89	IRR	124	FDF	159	SHH	194	PNC
20	HHS	55	PNC	90	HSH	125	SHH	160	IRR	195	PNC
21	PNC	56	PNC	91	SHH	126	PNC	161	HSH	196	HSH
22	HSH	57	PNC	92	SHH	127	PNC	162	PNC	197	IRR
23	SHS	58	PNC	93	PNC	128	SHH	163	SHH	198	PNC
24	SHH	59	FDF	94	PNC	129	FDF	164	PNC	199	SHH
25	SHH	60	SHH	95	SHS	130	IRR	165	SHH	200	HHS
26	IRR	61	IRR	96	PNC	131	HSH	166	SHH	201	SHS
27	SHS	62	PNC	97	IRR	132	HSH	167	FDF	202	FDF
28	PNC	63	SHS	98	PNC	133	PNC	168	IRR	203	HSH
29	PNC	64	IRR	99	IRR	134	HHS	169	PNC	204	PNC
30	PNC	65	PNC	100	PNC	135	PNC	170	PNC	205	PNC
31	PNC	66	PNC	101	SHS	136	HSH	171	PNC	206	PNC
32	SHH	67	PNC	102	PNC	137	SH	172	IRR	207	FLA
33	SHH	68	IRR	103	SHH	138	SHS	173	PNC	208	IRR
34	HSH	69	IRR	104	FDF	139	PNC	174	SHS		
35	PNC	70	IRR	105	HHS	140	PNC	175	SHH		

Table A-11.: Evolutionary patterns in microwaves for the whole work sample.

References

[1] Antonucci, E. ; Gabriel, A. H. ; Acton, L. W. ; Leibacher, J. W. ; Culhane, J. L. ; Rapley, C. G. ; Doyle, J. G. ; Machado, M. E. ; Orwig, L. E.: Impulsive phase of flares in soft X-ray emission. *Solar Physics* 78 (1982), May, p. 107–123

[2] Ardila, A. M.: *Física Experimental*. Segunda Edición. Bogotá : Unibiblos, Universidad Nacional de Colombia, 2007

[3] Arnoldy, R. L. ; Kane, S. R. ; Winckler, J. R.: Energetic Solar Flare X-Rays Observed by Satellite and Their Correlation with Solar Radio and Energetic Particle Emission. *Astrophysical Journal* 151 (1968), February, p. 711

[4] Aschwanden, M. J.: Deconvolution of Directly Precipitating and Trap-Precipitating Electrons in Solar Flare Hard X-Rays. I. Method and Tests. *The Astrophysical Journal* 502 (1998), July, p. 455–467

[5] Aschwanden, M. J.: *Physics of the Solar Corona*. First Edition. Chichester, UK : Springer, Praxis Publishing, 2004

[6] Aschwanden, M. J.: Pulsed Particle Injection in a Reconnection-Driven Dynamic Trap Model in Solar Flares. *The Astrophysical Journal* 608 (2004), June, p. 554–561

[7] Bahcall, J. N. ; Serenelli, A. M. ; Basu, S.: New Solar Opacities, Abundances, Helioseismology, and Neutrino Fluxes. *The Astrophysical Journal* 621 (2005), March, p. L85–L88

[8] Bahcall, J. N. ; Ulrich, R. K.: Solar models, neutrino experiments, and helioseismology. *Reviews of Modern Physics* 60 (1988), April, p. 297–372

[9] Bastian, T. ; Schrijver, C. J. (Ed.) ; Siscoe, G. L. (Ed.): *Heliophysics. Space Storms and Radiation: Causes and Effects*. Vol. 2. First Edition. New York : Cambridge University Press, 2010

[10] Bastian, T. S. ; Benz, A. O. ; Gary, D. E.: Radio Emission from Solar Flares. *Annual Review of Astronomy and Astrophysics* 36 (1998), p. 131–188

[11] Benz, A. O.: *Astrophysics and Space Science Library*. Vol. 279: *Plasma Astrophysics. Kinetic Processes in Solar and Stellar Coronae*. Second Edition. Berlin, Heidelberg : Kluwer Academic Publishers, June 2002

[12] Benz, A. O.: Flare Observations. *Living Reviews in Solar Physics* 14 (2016), Dec, Nr. 1, p. 2

[13] Berry, H. G. ; Gabrielse, G. ; Livingston, A. E.: Measurement of the Stokes parameters of light. *Applied Optics* 16 (1977), December, p. 3200–3205

[14] Bhatnagar, A. ; Livingston, W.: *Astronomy and Astrophysics*. Vol. 6: *Fundamentals of Solar Astronomy*. —. Singapore : World Scientific Publishing, 2005

[15] Bloomfield, D. S. ; Higgins, P. A. ; McAteer, R. T. J. ; Gallagher, P. T.: Toward Reliable Benchmarking of Solar Flare Forecasting Methods. *The Astrophysical Journal Letters* 747 (2012), March, p. L41

[16] Brown, J. C.: The Deduction of Energy Spectra of Non-Thermal Electrons in Flares from the Observed Dynamic Spectra of Hard X-Ray Bursts. *Solar Physics* 18 (1971), July, p. 489–502

[17] Brown, J. C.: The interpretation of spectra, polarization, and directivity of solar hard X-rays. In: *Solar Gamma-, X-, and EUV Radiation*. Kane, S. R. (Ed.) Vol. 68, 1975, p. 245–282

[18] Buitrago-Casas, J. C. ; Martínez Oliveros, J. C. ; Lindsey, C. ; Calvo-Mozo, B. ; Krucker, S. ; Glesener, L. ; Zharkov, S.: A Statistical Correlation of Sunquakes Based on Their Seismic and White-Light Emission. *Solar Physics* 290 (2015), November, p. 3151–3162

[19] Canavos, G. C.: *Probabilidad y Esdaística: Aplicaciones y Métodos*. Primera Edición en Español. México D.F. : McGraw-Hill/Interamericana de México, S.A., 1988

[20] Carmichael, H.: A Process for Flares. *NASA Special Publication* 50 (1964), p. 451

[21] Carrington, R. C.: Description of a Singular Appearance seen in the Sun on September 1, 1859. *Monthly Notices of the Royal Astronomical Society* 20 (1859), November, p. 13–15

[22] Caspi, A. ; Krucker, S. ; Lin, R. P.: Statistical Properties of Super-hot Solar Flares. *The Astrophysical Journal* 781 (2014), January, p. 43

[23] Chandrasekhar, S.: *An Introduction to the Study of Stellar Structure*. First Edition. Chicago : The University of Chicago Press, 1939

[24] Chandrasekhar, S.: *Radiative Transfer*. Second Edition. New York : Dover Publications Inc, 1960

[25] Chaplin, W. J.: *The music of the Sun*. First Edition. Oxford : One world, 2006

[26] Cohen, O. ; Schrijver, C. J. (Ed.) ; Bagenal, F. (Ed.) ; Sojka, J. J. (Ed.): *Heliophysics. Active stars, their astrospheres, and impacts on planetary environments*. Vol. 4. First Edition. Corwall : Cambridge University Press, 2016

[27] Cohen-Tannoudji, C. ; Diu, B. ; F., Laloe: *Quantum Mechanics, Volume 2*. Second Edition. Paris : Wiley VCH, 1977

[28] Cowling, T. G.: *Magnetohidrodinámica*. First Edition in Spanish. Madrid : Editorial Alhambra, 1968

[29] Cranmer, S. R. ; van Ballegooijen, A. A. ; Edgar, R. J.: Self-consistent Coronal Heating and Solar Wind Acceleration from Anisotropic Magnetohydrodynamic Turbulence. *The Astrophysical Journal Supplement Series* 171 (2007), August, p. 520–551

[30] Datlowe, D. W. ; Lin, R. P.: Evidence for Thin-Target X-Ray Emission in a Small Solar Flare on 26 February 1972. *Solar Physics* 32 (1973), October, p. 459–468

[31] De Pontieu, B. ; McIntosh, S. W. ; Hansteen, V. H. ; Schrijver, C. J.: Observing the Roots of Solar Coronal Heating - in the Chromosphere. *The Astrophysical Journal Letters* 701 (2009), August, p. L1–L6

[32] De Pontieu, B. ; Title, A. M. ; Lemen, J. R. ; Kushner, G. D. ; Akin, D. J. ; Allard, B. ; Berger, T. ; Boerner, P. ; Cheung, M. ; Chou, C. ; Drake, J. F. ; Duncan, D. W. ; Freeland, S. ; Heyman, G. F. ; Hoffman, C. ; Hurlburt, N. E. ; Lindgren, R. W. ; Mathur, D. ; Rehse, R. ; Sabolish, D. ; Seguin, R. ; Schrijver, C. J. ; Tarbell, T. D. ; Wülser, J.-P. ; Wolfson, C. J. ; Yanari, C. ; Mudge, J. ; Nguyen-Phuc, N. ; Timmons, R. ; van Bezooijen, R. ; Weingrod, I. ; Brookner, R. ; Butcher, G. ; Dougherty, B. ; Eder, J. ; Knagenhjelm, V. ; Larsen, S. ; Mansir, D. ; Phan, L. ; Boyle, P. ; Cheimets, P. N. ; DeLuca, E. E. ; Golub, L. ; Gates, R. ; Hertz, E. ; McKillop, S. ; Park, S. ; Perry, T. ; Podgorski, W. A. ; Reeves, K. ; Saar, S. ; Testa, P. ; Tian, H. ; Weber, M. ; Dunn, C. ; Eccles, S. ; Jaeggli, S. A. ; Kankelborg, C. C. ; Mashburn, K. ; Pust, N. ; Springer, L. ; Carvalho, R. ; Kleint, L. ; Marmie, J. ; Mazmanian, E. ; Pereira, T. M. D. ; Sawyer, S. ; Strong, J. ; Worden, S. P. ; Carlsson, M. ; Hansteen, V. H. ; Leenaarts, J. ; Wiesmann, M. ; Aloise, J. ; Chu, K.-C. ; Bush, R. I. ; Scherrer, P. H. ; Brekke, P. ; Martinez-Sykora, J. ; Lites, B. W. ; McIntosh, S. W. ; Uitenbroek, H. ; Okamoto, T. J. ; Gummin, M. A. ; Auker, G. ; Jerram, P. ; Pool, P. ; Waltham, N.: The Interface Region Imaging Spectrograph (IRIS). *Solar Physics* 289 (2014), July, p. 2733–2779

[33] Dennis, B. R.: Solar flare hard X-ray observations. *Solar Physics* 118 (1988), March, p. 49–94

[34] Dennis, B. R. ; Schwartz, R. A.: Solar flares - The impulsive phase. *Solar Physics* 121 (1989), March, p. 75–94

[35] Dennis, B. R. ; Zarro, D. M.: The Neupert effect - What can it tell us about the impulsive and gradual phases of solar flares? *Solar Physics* 146 (1993), July, p. 177–190

[36] Dulk, G. A.: Radio emission from the sun and stars. *Annual Review of Astronomy and Astrophysics* 23 (1985), p. 169–224

[37] Dulk, G. A. ; Marsh, K. A.: Simplified expressions for the gyrosynchrotron radiation from mildly relativistic, nonthermal and thermal electrons. *Astrophysical Journal* 259 (1982), August, p. 350–358

[38] Eddy, J. A. ; Ise, R.: *A new sun : the solar results from SKYLAB*. 1979

[39] Fajardo-Mendieta, W. G. ; Martínez-Oliveros, J. C. ; Alvarado-Gómez, J. D. ; Calvo-Mozo, B.: Impulsivity Parameter for Solar Flares. *The Astrophysical Journal* 818 (2016), February, p. 56

[40] Feldman, U. ; Doschek, G. A. ; Klimchuk, J. A.: The Occurrence Rate of Soft X-Ray Flares as a Function of Solar Activity. *The Astrophysical Journal* 474 (1997), January, p. 511–517

[41] Fivian, M. ; Hemmeck, R. ; McHedlishvili, A. ; Zehnder, A.: RHESSI Aspect Reconstruction. *Solar Physics* 210 (2002), November, p. 87–99

[42] Fletcher, L. ; Hudson, H. S.: Impulsive Phase Flare Energy Transport by Large-Scale Alfvén Waves and the Electron Acceleration Problem. *The Astrophysical Journal* 675 (2008), March, p. 1645–1655

[43] Fontenla, J. M. ; Avrett, E. H. ; Loeser, R.: Energy balance in the solar transition region. I - Hydrostatic thermal models with ambipolar diffusion. *Astrophysical Journal* 355 (1990), June, p. 700–718

[44] Forbes, T. ; Schrijver, C. J. (Ed.) ; Siscoe, G. L. (Ed.): *Heliophysics. Space Storms and Radiation: Causes and Effects*. Vol. 2. First Edition. New York : Cambridge University Press, 2010

[45] Foukal, P. V.: *Solar Astrophysics*. Second Edition. Weinheim : Wiley-VCH, 2004

[46] Foullon, C. ; Verwichte, E. ; Nakariakov, V. M. ; Fletcher, L.: X-ray quasi-periodic pulsations in solar flares as magnetohydrodynamic oscillations. *Astronomy and Astrophysics* 440 (2005), September, p. L59–L62

[47] Fraknoi, A. ; Morrison, D. ; Wolff, S.: *Voyages Through the Universe*. Saunders College, 2000 (Voyages Through the Universe Series). – ISBN 9780030259838

[48] Gary, D. E. ; Hurford, G. J. ; Gary, D. E. (Ed.) ; Keller, C. U. (Ed.): *Solar and Space Weather Radiophysics*. Vol. 314. First Edition. Dordrecht : Kluwer Academic Publishers, 2005

[49] Glesener, L. E. *Faint Coronal Hard X-rays From Accelerated Electrons in Solar Flares*. PhD thesis. University of California, Berkeley. 2012

[50] Golub, L. ; Pasachoff, J. M.: *Nearest Star: The Surprising Science of Our Sun*. First Edition. Cambridge, Massachusetts : Harvard University Press, 2001

[51] Grigis, P. C. ; Benz, A. O.: The spectral evolution of impulsive solar X-ray flares. *Astronomy and Astrophysics* 426 (2004), November, p. 1093–1101

[52] Guerrero, G. ; Smolarkiewicz, P. K. ; de Gouveia Dal Pino, E. M. ; Kosovichev, A. G. ; Mansour, N. N.: On the Role of Tachoclines in Solar and Stellar Dynamos. *The Astrophysical Journal* 819 (2016), March, p. 104

[53] Hajdas, W. ; Eggel, C. ; Wigger, C. ; Sanctuary, H. ; Zehnder, A. ; Smith, D.: Spacecraft Activation and South Atlantic Anomaly Profiles Measured with RHESSI Satellite. *ESA Special Publication* Vol. 536, 2004, p. 607

[54] Hansen, C. J. ; Kawaler, S. D.: *Stellar Interiors. Physical Principles, Structure, and Evolution*. First Edition. New York : Springer-Verlag, 1994

[55] Hansteen, V. ; Schrijver, C. J. (Ed.) ; Siscoe, G. L. (Ed.): *Heliophysics: Plasma Physics of the Local Cosmos*. Vol. 1. First Edition. New York : Cambridge University Press, 2009

[56] Hathaway, D. H.: The Solar Cycle. *Living Reviews in Solar Physics* 12 (2015), September, p. 4

[57] Hirayama, T.: Theoretical Model of Flares and Prominences. I: Evaporating Flare Model. *Solar Physics* 34 (1974), February, p. 323–338

[58] Hodgson, R.: On a curious Appearance seen in the Sun. *Monthly Notices of the Royal Astronomical Society* 20 (1859), November, p. 15–16

[59] Hudson, H.: Global Properties of Solar Flares. *Space Science Reviews* 158 (2011), p. 5–41

[60] Hudson, H. S.: Thick-Target Processes and White-Light Flares. *Solar Physics* 24 (1972), June, p. 414–428

[61] Hudson, H. S.: Differential Emission-Measure Variations and the "Neupert Effect". *Bulletin of the American Astronomical Society* Vol. 23, 1991, p. 1064

[62] Hurford, G. J. ; Schmahl, E. J. ; Schwartz, R. A. ; Conway, A. J. ; Aschwanden, M. J. ; Csillaghy, A. ; Dennis, B. R. ; Johns-Krull, C. ; Krucker, S. ; Lin, R. P. ; McTiernan, J. ; Metcalf, T. R. ; Sato, J. ; Smith, D. M.: The RHESSI Imaging Concept. *Solar Physics* 210 (2002), November, p. 61–86

[63] Kane, S. R.: Impulsive /flash/ phase of solar flares - Hard X-ray, microwave, EUV and optical observations. In: *Coronal Disturbances*. Newkirk, G. A. (Ed.) Vol. 57, 1974, p. 105–141

[64] Karttunen, H. ; Pekka Kröger, P. ; Heikki Oja, H. ; Markku Poutanen, M. ; k. J., Donner: *Fundamentals Astronomy*. Fifth Edition. Berlin : Springer, 2007

[65] Kiplinger, A. L.: Comparative Studies of Hard X-Ray Spectral Evolution in Solar Flares with High-Energy Proton Events Observed at Earth. *Astrophysical Journal* 453 (1995), November, p. 973

[66] Kliem, B. ; Karlický, M. ; Benz, A. O.: Solar flare radio pulsations as a signature of dynamic magnetic reconnection. *Astronomy and Astrophysics* 360 (2000), August, p. 715–728

[67] Koch, H. W. ; Motz, J. W.: Bremsstrahlung Cross-Section Formulas and Related Data. *Reviews of Modern Physics* 31 (1959), October, p. 920–955

[68] Kontar, E. P. ; Brown, J. C. ; Emslie, A. G. ; Hajdas, W. ; Holman, G. D. ; Hurford, G. J. ; Kašparová, J. ; Mallik, P. C. V. ; Massone, A. M. ; McConnell, M. L. ; Piana, M. ; Prato, M. ; Schmahl, E. J. ; Suarez-Garcia, E.: Deducing Electron Properties from Hard X-ray Observations. *Space Science Reviews* 159 (2011), September, p. 301–355

[69] Kontar, E. P. ; Hannah, I. G. ; MacKinnon, A. L.: Chromospheric magnetic field and density structure measurements using hard X-rays in a flaring coronal loop. *Astronomy and Astrophysics* 489 (2008), October, p. L57–L60

[70] Kopp, R. A. ; Pneuman, G. W.: Magnetic reconnection in the corona and the loop prominence phenomenon. *Solar Physics* 50 (1976), October, p. 85–98

[71] Kosovichev, A. G. ; Zharkova, V. V.: X-ray flare sparks quake inside Sun. *Nature* 393 (1998), May, p. 317–318

[72] Kosugi, T. ; Dennis, B. R. ; Kai, K.: Energetic electrons in impulsive and extended solar flares as deduced from flux correlations between hard X-rays and microwaves. *Astrophysical Journal* 324 (1988), January, p. 1118–1131

[73] Krucker, S. ; Christe, S. ; Glesener, L. ; Ishikawa, S.-n. ; Ramsey, B. ; Takahashi, T. ; Watanabe, S. ; Saito, S. ; Gubarev, M. ; Kilaru, K. ; Tajima, H. ; Tanaka, T. ; Turin, P. ; McBride, S. ; Glaser, D. ; Fermin, J. ; White, S. ; Lin, R.: First Images from the Focusing Optics X-Ray Solar Imager. *The Astrophysical Journal Letters* 793 (2014), October, p. L32

[74] Krucker, S. ; Hannah, I. G. ; Lin, R. P.: RHESSI and Hinode X-Ray Observations of a Partially Occulted Solar Flare. *The Astrophysical Journal,* 671 (2007), December, p. L193–L196

[75] Kundu, M. R. ; White, S. M. ; Shibasaki, K. ; Sakurai, T. ; Grechnev, V. V.: Spatial Structure of Simple Spiky Bursts at Microwave/Millimeter Wavelengths. *The Astrophysical Journal* 547 (2001), February, p. 1090–1099

[76] Landau, L. D. ; Lifshitz, E. M.: *Course of theoretical physics*. Vol. 6: *Fluid Mechanics*. Second Edition. Oxford : Pergamon Press, 1987

[77] Lee, J. ; Gary, D. E. (Ed.) ; Keller, C. U. (Ed.): *Solar and Space Weather Radiophysics*. Vol. 314. First Edition. Dordrecht : Kluwer Academic Publishers, 2005

[78] Lee, J. ; Gary, D. E.: Solar Microwave Bursts and Injection Pitch-Angle Distribution of Flare Electrons. *The Astrophysical Journal* 543 (2000), November, p. 457–471

[79] Lee, J. ; Gary, D. E. ; Qiu, J. ; Gallagher, P. T.: Electron Transport during the 1999 August 20 Flare Inferred from Microwave and Hard X-Ray Observations. *The Astrophysical Journal* 572 (2002), June, p. 609–625

[80] Lin, R. P. ; Dennis, B. R. ; Hurford, G. J. ; Smith, D. M. ; Zehnder, A. ; Harvey, P. R. ; Curtis, D. W. ; Pankow, D. ; Turin, P. ; Bester, M. ; Csillaghy, A. ; Lewis, M. ; Madden, N. ; van Beek, H. F. ; Appleby, M. ; Raudorf, T. ; McTiernan, J. ; Ramaty, R. ; Schmahl, E. ; Schwartz, R. ; Krucker, S. ; Abiad, R. ; Quinn, T. ; Berg, P. ; Hashii, M. ; Sterling, R. ; Jackson, R. ; Pratt, R. ; Campbell, R. D. ; Malone, D. ; Landis, D. ; Barrington-Leigh, C. P. ; Slassi-Sennou, S. ; Cork, C. ; Clark, D. ; Amato, D. ; Orwig, L. ; Boyle, R. ; Banks, I. S. ; Shirey, K. ; Tolbert, A. K. ; Zarro, D. ; Snow, F. ; Thomsen, K. ; Henneck, R. ; McHedlishvili, A. ; Ming, P. ; Fivian, M. ; Jordan, J. ; Wanner, R. ; Crubb, J. ; Preble, J. ; Matranga, M. ; Benz, A. ; Hudson, H. ; Canfield, R. C. ; Holman, G. D. ; Crannell, C. ; Kosugi, T. ; Emslie, A. G. ; Vilmer, N. ; Brown, J. C. ; Johns-Krull, C. ; Aschwanden, M. ; Metcalf, T. ; Conway, A.: The Reuven Ramaty High-Energy Solar Spectroscopic Imager (RHESSI). *Solar Physics* 210 (2002), November, p. 3–32

[81] Liu, W. ; Chen, Q. ; Petrosian, V.: Plasmoid Ejections and Loop Contractions in an Eruptive M7.7 Solar Flare: Evidence of Particle Acceleration and Heating in Magnetic Reconnection Outflows. *The Astrophysical Journal* 767 (2013), April, p. 168

[82] Longair, M. S.: *High Energy Astrophysics*. Third Edition. London : Cambridge University Press, 2011

[83] Losada, I. R. ; Warnecke, J. ; Glogowski, K. ; Roth, M. ; Brandenburg, A. ; Kleeorin, N. ; Rogachevskii, I.: A new look at sunspot formation using theory and observations. *ArXiv e-prints* (2017), April

[84] Lu, E. T. ; Petrosian, V.: The relative timing of microwaves and X-rays from solar flares.

[85] Mandrini, C. H. *Solar Structure and Activity: Transient Phenomena*. Summer School on Solar Astrophysics: Modern Trends and Techniques. Bogotá, Colombia. 2012

[86] Martínez-Oliveros, J. C. *Multi-Wavelength Analysis in Flare Seismology and the Role of Magnetic Field Dynamics in the Seismicity of Solar Active Regions*. PhD thesis. Monash University. 2009

[87] Martínez-Oliveros, J. C. ; Donea, A.-C. ; Cally, P. S. ; Moradi, H.: Helioseismic analysis of the solar flare-induced sunquake of 2005 January 15 - II. A magnetoseismic study. *Monthly Notices of the Royal Astronomical Society* 389 (2008), October, p. 1905–1910

[88] Melrose, D. B. ; Brown, J. C.: Precipitation in trap models for solar hard X-ray bursts. *Monthly Notices of the Royal Astronomical Society* 176 (1976), July, p. 15–30

[89] Meyer-Vernet, N.: *Basics of the Solar Wind*. Cambridge University Press (Cambridge Atmospheric and Space Science Series)

[90] Nakajima, H. ; Sekiguchi, H. ; Sawa, M. ; Kai, K. ; Kawashima, S.: The radiometer and polarimeters at 80, 35, and 17 GHz for solar observations at Nobeyama. *Astronomical Society of Japan* 37 (1985), p. 163–170

[91] Neupert, W. M.: Comparison of Solar X-Ray Line Emission with Microwave Emission during Flares. *Astrophysical Journal* 153 (1968), July, p. L59

[92] Ofman, L. ; Sui, L.: Oscillations of Hard X-Ray Flare Emission Observed by RHESSI: Effects of Super-Alfvénic Beams? *The Astrophysical Journal* 644 (2006), June, p. L149–L152

[93] Öztürk, M. K.: Trajectories of charged particles trapped in Earth's magnetic field. *American Journal of Physics* 80 (2012), Nr. 5, p. 420–428

[94] Parker, E. N.: Nanoflares and the solar X-ray corona. *Astrophysical Journal* 330 (1988), July, p. 474–479

[95] Roy, J.-R. ; Datlowe, D. W.: X-ray bursts from solar flares behind the limb. *Solar Physics* 40 (1975), January, p. 165–182

[96] Ryan, D. F. ; Milligan, R. O. ; Gallagher, P. T. ; Dennis, B. R. ; Tolbert, A. K. ; Schwartz, R. A. ; Young, C. A.: The Thermal Properties of Solar Flares over Three Solar Cycles Using GOES X-Ray Observations. *The Astrophysical Journal Supplement* 202 (2012), October, p. 11

[97] Rybicki, G. B. ; Lightman, A. P.: *Radiative Processes in Astrophysics*. 2nd Edition. Weinheim : Wiley-VCH, 2004

[98] Schnack, D. D.: *Lectures Notes in Physics*. Vol. 780: *Lectures in Magnetohydrodynamics*. First Edition. Berlin, Heidelberg : Springer, 2009

[99] Schwartz, R. A. ; Csillaghy, A. ; Tolbert, A. K. ; Hurford, G. J. ; McTiernan, J. ; Zarro, D.: RHESSI Data Analysis Software: Rationale and Methods. *Solar Physics* 210 (2002), November, p. 165–191

[100] Shibata, K.: New observational facts about solar flares from YOHKOH studies - evidence of magnetic reconnection and a unified model of flares. *Advances in Space Research* 17 (1996), p. 9–18

[101] Shu, F. H.: *The Physics of Astrophysics. Volume I: Radiation*. First Edition. Mill Valley, California : University Science Books, 1991

[102] SILSO World Data Center: The International Sunspot Number. *International Sunspot Number Monthly Bulletin and online catalogue* (1749-2017)

[103] Silva, A. V. R. ; Wang, H. ; Gary, D. E.: Correlation of Microwave and Hard X-Ray Spectral Parameters. *The Astrophysical Journal* 545 (2000), December, p. 1116–1123

[104] Simões, P. J. A. ; Kontar, E. P.: Implications for electron acceleration and transport from non-thermal electron rates at looptop and footpoint sources in solar flares. *Astronomy and Astrophysics* 551 (2013), March, p. A135

[105] Smith, D. M. ; Lin, R. P. ; Turin, P. ; Curtis, D. W. ; Primbsch, J. H. ; Campbell, R. D. ; Abiad, R. ; Schroeder, P. ; Cork, C. P. ; Hull, E. L. ; Landis, D. A. ; Madden, N. W. ; Malone, D. ; Pehl, R. H. ; Raudorf, T. ; Sangsingkeow, P. ; Boyle, R. ; Banks, I. S. ; Shirey, K. ; Schwartz, R.: The RHESSI Spectrometer. *Solar Physics* 210 (2002), November, p. 33–60

[106] Somov, B. V.: *Astrophysics and Sciences Library*. Vol. 340: *Plasma Astrophysics, Part 1*. Second Edition. Moscow : Springer, 2006

[107] Stix, M.: *The Sun: An Introduction*. First Edition. Berlin-Heidelberg : Springer - Verlag, 1989

[108] Sturrock, P. A.: Model of the High-Energy Phase of Solar Flares. *Nature* 211 (1966), August, p. 695–697

[109] Syrovatskii, S. I.: Solar Flare Time Development: Three Phases. *Comments on Astrophysics and Space Physics* 4 (1972), March, p. 65

[110] Takakura, T. ; Kai, K.: Energy Distribution of Electrons Producing Microwave Impulsive Bursts and X-Ray Bursts from the Sun. *Publications of the Astronomical Society of Japan* 18 (1966), p. 57

[111] Tejeiro, J. M.: *Sobre la teoría especial de la relatividad*. First Edition. Bogotá : Editorial Universidad Nacional de Colombia, 2005

[112] Torii, C. ; Tsukiji, Y. ; Kobayashi, S. ; Yoshimi, N. ; Tanaka, H. ; Enome, S.: Full-automatic radiopolarimeters for solar patrol at microwave frequencies. *Proceedings of the Research Institute of Atmospherics, Nagoya University* 26 (1979), March, p. 129–132

[113] Tsuneta, S.: Impulsive and hot thermal solar flares. *Solar Physics* 113 (1987), p. 35–45

[114] Vernazza, J. E. ; Avrett, E. H. ; Loeser, R.: Structure of the Solar Chromosphere. Basic Computations and Summary of the Results. *Astrophysical Journal* 184 (1973), September, p. 605–632

[115] Vernazza, J. E. ; Avrett, E. H. ; Loeser, R.: Structure of the solar chromosphere. III - Models of the EUV brightness components of the quiet-sun. *Astrophysical Journal Supplement Series* 45 (1981), April, p. 635–725

[116] Veronig, A. ; Temmer, M. ; Hanslmeier, A. ; Otruba, W. ; Messerotti, M.: Temporal aspects and frequency distributions of solar soft X-ray flares. *Astronomy and Astrophysics* 382 (2002), February, p. 1070–1080

[117] Veronig, A. M. ; Brown, J. C. ; Dennis, B. R. ; Schwartz, R. A. ; Sui, L. ; Tolbert, A. K.: Physics of the Neupert Effect: Estimates of the Effects of Source Energy, Mass Transport, and Geometry Using RHESSI and GOES Data. *The Astrophysical Journal* 621 (2005), March, p. 482–497

[118] Wright, P. J. ; Hannah, I. G. ; Grefenstette, B. W. ; Glesener, L. ; Krucker, S. ; Hudson, H. S. ; Smith, D. M. ; Marsh, A. J. ; White, S. M. ; Kuhar, M.: Microflare Heating of a Solar Active Region Observed with NuSTAR, Hinode/XRT, and SDO/AIA. *The Astrophysical Journal* 844 (2017), August, p. 132